

The Development of a Near-Infrared Integral Field Unit for Spatially Resolved Studies of Starburst Galaxies



Yutaro Kitagawa

Department of Astronomy, Graduate School of Science
The University of Tokyo

This dissertation is submitted for the degree of
Doctor of Philosophy

December 2016

Abstract

In the optical and near-infrared astronomy, obtaining spatially resolved spectra (*i.e.* integral field spectroscopy; IFS) is increasingly important year by year since they provide a clue to understanding a connection between a local star formation process and a global star formation activity in a galaxy. It is also important to observe nearby starburst galaxies whose specific star formation rates are nearly two orders of magnitude higher than those of nearby normal star-forming galaxies. They are rather close to high- z galaxies at $z = 1\text{--}2$, at which the cosmic star formation activity peaks (“cosmic noon”). Since high spatial resolution and spectroscopic observations can be easily achieved in the nearby universe, performing IFS observation of nearby starburst galaxies with high specific star formation is important to investigate the origin of star formation activity at cosmic noon.

In this thesis, we present a development of a near-infrared integral field unit (IFU) and results of a high-spatial resolution imaging of the nearby starburst galaxies. In Part I, we first introduce a concept of a module-like compact IFU, called SWIMS-IFU. SWIMS-IFU provides a new observation mode of SWIMS, which is one of the first generation instruments of the University of Tokyo Atacama Observatory (TAO) 6.5-m infrared telescope. Its optical parameters are optimized for a seeing-limited observation and SWIMS-IFU has the wide field-of-view of 145'' and 220'' at the Subaru and the TAO 6.5-m telescope, respectively, as well as the wide spectral coverage of $0.9\text{--}2.5\text{ }\mu\text{m}$. These capabilities will realize wider science targets and an efficient IFS survey, which is still rare in the near-infrared wavelength, although such surveys have been already implemented in the optical wavelength (*e.g.* CALIFA, SAMI, and MaNGA). To realize this concept, a very tight limitation is imposed on optical layout, which requires a compact size of $< 60 \times 170 \times 220\text{ mm}^3$. We employ aspheric surfaces and carefully take account of manufacturability and alignment procedure of optics throughout optimization. As a result, we succeed in constructing a compact optical layout satisfying the size specifications and optical performance for seeing-limited observations.

We next perform a proof-of-principle experiment of fabrication of a slicing mirror array, which is the heart of the IFU optics. We demonstrate monolithic test fabrication using end-mill process of a nickel phosphorus (NiP) coated mirror array whose aperture size is $10\text{ mm} \times 12.5\text{ mm}$ and twenty-five reflective surfaces with a slice width of $500\text{ }\mu\text{m}$. We

optimize the processing conditions by finding out the cause of various shape error based on preliminary experiments. A surface roughness of 10 nm and a shape error of 80 nm P-V has been achieved by simultaneous two-axis control of a diamond end-mill tool. This study is the first demonstration of monolithic fabrication of a NiP coated slicing mirror array.

Further we verify diamond cutting performance of various mirror materials such as conventional and special aluminum alloys, oxygen free copper, and electroless NiP plating. We show surface a roughness of ~ 5 nm can be achieved by diamond cutting, especially for special aluminum alloy and oxygen free copper. We also experimentally confirm that high silicon-containing aluminum optimized to match the CTE of NiP plating obviously suppresses the shape deformation at cryogenic condition. Our results indicate that this high-Si containing alloy coated with NiP is optimal for use on infrared mirror material in terms of the both surface roughness and shape.

In Part II, we have carried out spatially-resolved study of nearby starburst galaxies using an AO-assisted Pa α imaging at the Subaru telescope. Two starburst galaxies are observed, one is at a mid-merger stage and the other probably at an early stage, and bright star formation clumps emitting in Pa α are detected clearly in both targets. We find a strong correlation between the star formation rate surface density (Σ_{SFR}) and the stellar mass surface density (Σ_{M_*}). This relationship is the near-infrared version of the $\Sigma_{\text{SFR}}-\Sigma_{M_*}$ relationship which has been reported by optical IFS observations, and we detect it in starburst galaxies using the near-infrared Pa α line for the first time. Our relation shows a specific star formation rate higher those found in local star-forming galaxies by an order of magnitude. We also find that star formation is active not only in the Pa α clumps but also at non-clump regions of the galaxy. The detected Pa α clumps have star formation rate surface density of $\Sigma_{\text{SFR}} \sim 3-4 M_{\odot} \text{ yr}^{-1} \text{ kpc}^{-2}$, which is higher compared with those of HII regions in nearby normal galaxies. They are similar to giant star forming clumps in clumpy galaxies at $z = 1-2$. Based on gas surface density and gas fraction derived from the Kennicutt-Schmidt law, these Pa α clumps may be local analogs of those of $z \sim 1-2$ clumpy galaxies.

The samples obtained with the Pa α imaging will be good candidates to follow-up with SWIMS-IFU and their dynamical information will be useful for understanding their star formation activities, which will provide important information on star-formation at high- z galaxies.

Table of contents

List of figures	ix
List of tables	xi
1 Introduction and overview of the thesis	1
1.1 Integral Field Spectroscopy	1
1.2 Spatially resolved study of Galaxies	3
1.3 Purpose and Approach	4
1.4 Constitution of the thesis	6
I The Development of SWIMS-IFU	7
2 Introduction of Part I	9
2.1 Integral Field Unit	9
2.2 Purpose of the Part I	11
3 Compact IFU with a Multi-Object Spectrograph	13
3.1 Concept of SWIMS-IFU	13
3.2 Host spectrograph: SWIMS	13
3.3 Specifications of SWIMS-IFU	17
3.3.1 Optical component	17
3.3.2 Mechanical component	19
4 Optical design	21
4.1 Optical Components	21
4.2 Paraxial calculation	23
4.2.1 Enlarger optics	23
4.2.2 IFU optics	30

4.3	Optimization	31
4.4	Results	35
4.4.1	Optical parameters	35
4.4.2	Size of the IFU	41
4.4.3	Optical Performance	41
4.5	Tolerance estimation	44
4.5.1	Tolerance values of each component	44
4.5.2	Alignment Strategy	47
4.5.3	Throughput Estimation	47
4.6	Summary of Optical Design	51
5	Monolithic Fabrication of a Slicing Mirror Array	53
5.1	Application of Ultra-Precision Cutting to IFU optics	53
5.2	Specifications and Methods	55
5.3	End mill processing with Single axis Control	56
5.4	Correction of the Parabolic Shape Error	59
5.5	Optimization of Cutting Condition	61
5.6	Conclusion of the Fabrication	62
6	Search for Advanced Infrared Mirror Materials	65
6.1	Study on Diamond Cutting Performance of Metallic Alloys	65
6.1.1	Mirror Materials for Infrared Optics	65
6.1.2	Diamond Turning Experiments	67
6.1.3	Results	69
6.2	Interferometric Measurements at Cryogenic Condition	73
6.2.1	Bimetallic Bending Effect	73
6.2.2	Experimental Setup	74
6.2.3	Results of Shape Measurement	76
6.3	Summary	81
II	Spatially resolved study of Starburst galaxies	83
7	Introduction of Part II	85
7.1	Star formation main sequence	85
7.1.1	Integrated Study	85
7.1.2	Spatially-resolved Study	86
7.2	Role of Starbursts in Galaxy Evolution	86

7.3	Scope of Part II	87
8	Sample and Data	89
8.1	PARADISES Survey	89
8.1.1	Survey Description	89
8.1.2	Target Selection	90
8.2	AO Observations using Subaru/IRCS	91
8.3	Data Reduction	95
9	Resolved Star Formation Activities	97
9.1	Deriving Physical Quantities	97
9.1.1	Star Formation Rate	97
9.1.2	Stellar Mass	98
9.2	Results	101
9.2.1	Integrated $SFR - M_*$ relation	101
9.2.2	Mapping Σ_{SFR} vs. Σ_{M*}	103
9.2.3	Detection of Pa α clumps	107
10	Discussion	111
10.1	Origin of Bursty Star Formation Activities	111
10.2	Star-forming clumps in Starbursts galaxies	113
11	Conclusion of the thesis	117
	References	123
	Appendix A Measurement Instruments	139
	Appendix B Elimination of cutting marks by post-process polishing	141

List of figures

1.1	Conceptual illustration of methods of 3–D spectroscopy.	2
1.2	Metric of published paper about IFS	4
1.3	Comparison of current and future near-infrared IFUs	5
2.1	Three methods used for integral field spectroscopy	10
3.1	Assembled structure of SWIMS	14
3.2	The schematic view of the mask exchanger unit	14
3.3	The configuration of the output slitlets of SWIMS-IFU	18
3.4	Conceptual diagram of the exchanging unit	19
3.5	A photograph of the IFU storage	20
4.1	Schematic view of optical layout	22
4.2	Definition and arrangement of each symbol.	23
4.3	Searching the paraxial parameters.	28
4.4	Calculation flowchart of optical parameters	29
4.5	Flowchart of optimization of the IFU	33
4.6	Overall view of SWIMS-IFU	34
4.7	Optical layout of SWIMS and SWIMS-IFU	35
4.8	Spot diagrams at the S1	42
4.9	Spot diagrams of all the channels at S3	42
4.10	Spot diagram at the detector of the blue arm of SWIMS	43
4.11	Spot diagram at the detector of the red arm of SWIMS	44
4.12	A full field of view spot diagram at S2	44
4.13	A full-field spot diagram at the cold stop position within SWIMS	45
4.14	CAD image of SWIMS-IFU	48
4.15	Reflection rate of NiP	49
4.16	Calculated scattering rate	50
4.17	Estimated total throughput of SWIMS-IFU	51

5.1	Conceptual image of IFU optics	54
5.2	Configuration of the slicing mirror	57
5.3	Processing procedure of fabrication	57
5.4	Surface profile of each materials	58
5.5	A photograph of finished surface	60
5.6	Shape dependence on C axis angle	60
5.7	Surface roughness after end milling	62
5.8	Angle measurements of each reflective plane.	63
6.1	Comparison of physical property of mirror materials	66
6.2	Photograph of various metallic mirrors	68
6.3	Configuration of surface measurements	70
6.4	Surface profile of each materials	70
6.5	Distribution of measured roughness	72
6.6	Shape measurements of surface finished mirrors	73
6.7	Setup for cryo-shape measurement	75
6.8	Results of cryo-shape measurement	76
6.9	Temperature variation and hysteresis values of NiP coated aluminum mirrors	78
6.10	Surface profile of NiP plating with a thickness of 5 μ m	79
8.1	Transmittance curve of the filters of IRCS	92
8.2	SDSS composite images	93
8.3	NB, continuum, and Pa α images	96
9.1	Surface density map of stellar mass and SFR	99
9.2	Star-formation rate versus stellar-mass plot	102
9.3	Spatially resolved $\Sigma_{\text{SFR}}-\Sigma_{M_*}$	104
9.4	Spatially resolved $\Sigma_{\text{SFR}}-\Sigma_{M_*}$ with 0.''2 binning.	105
9.5	Radial distribution of sSFR	106
9.6	Pa α clumps in $\Sigma_{\text{SFR}}-\Sigma_{M_*}$ plane.	109
10.1	Scaling relation of star-forming clumps	115
A.1	Photographs of measurement instruments.	140
B.1	Results of modified polishing	142

List of tables

3.1	Specifications of SWIMS	16
3.2	Specifications and Requirements of SWIMS-IFU	17
4.1	Paraxial parameters of PO1 and PO2.	30
4.2	Paraxial parameters	31
4.3	Surface information and coordinates of pre-optical system	37
4.4	Surface information and coordinates of each channel of the slicing mirror array	38
4.5	Surface information and coordinates of each channel of the pupil mirror array	39
4.6	Surface information and coordinates of each channel of the slit mirror array	40
4.7	Sensitivity analysis for Ch-13	46
4.8	Tolerance table of each component	47
5.1	Examples of recent fabrications of image slicers	55
5.2	Specifications of the slicing mirror array	56
5.3	Summary of cutting conditions and measurement results	63
6.1	Processing conditions of diamond turning	69
6.2	Summary of surface roughness and shape error	74
6.3	Specifications of test pieces for cryo-measurements	75
6.4	Difference value of P-V values between room temperature and cryogenic condition	80
8.1	Total number of observable targets with IRCS	90
8.2	AO188 observations	94
9.1	Summary of SFR and stellar mass	100
9.2	Summary of SFR and stellar mass of Pa α clumps	108
10.1	Gas properties derived from KS-law	112

A.1 Specifications of measurement instruments 140

Chapter 1

Introduction and overview of the thesis

1.1 Integral Field Spectroscopy

Integral field spectroscopy (IFS) is one of observation methods that can acquire spatial information and spectral information at the same time (*i.e.* spatially resolved spectra over a two-dimensional field of view). An optical component that realizes IFS observation is called an integral field unit (IFU). IFUs allow us to investigate the spatial distribution of metallicity (Magrini et al., 2016) and stellar population (Sánchez-Blázquez et al., 2014) within the galaxy, and also to extract the kinematic information such as radial velocity and velocity dispersion field at both low- and high-redshift galaxies (*e.g.* Glazebrook (2013), and references therein).

As a final data product the IFS observation provides a data cube in which information of (X, Y, λ) is stored. Meanwhile, there are other observation methods to obtain a data cube, which are generally referred to as three-dimensional spectroscopy (Allington-Smith et al., 2006). In optical to infrared wavelength, the difference between an IFS and other methods lies in the method of generating a data cube as shown in Fig. 1.1. For example, an imaging fourier transform spectrometer (IFTS) and a fabry-Perot spectrometer (FPS) use the time domain to scan in the spectral space and the fourier space, respectively (Eisenhauer and Raab, 2015). In these methods, since all the pixels of a detector can be used in the spatial direction, the wider field of view and high spectral dispersion can be realized. Using a long-slit scanning (Fig. 1.1b), a data cube is generated by translating a slit position or rotating a slit direction on a object. This is the very simple method that can be performed with conventional spectrographs. However, the scanning methods have the problem that an observation time tend to be long and it is sensitive to temporal variability such as atmospheric conditions and instrument stability. On the other hand, the IFS can acquire data cubes by a snapshot using optical systems such as a fiber bundle, a microlens array, or mirror arrays.

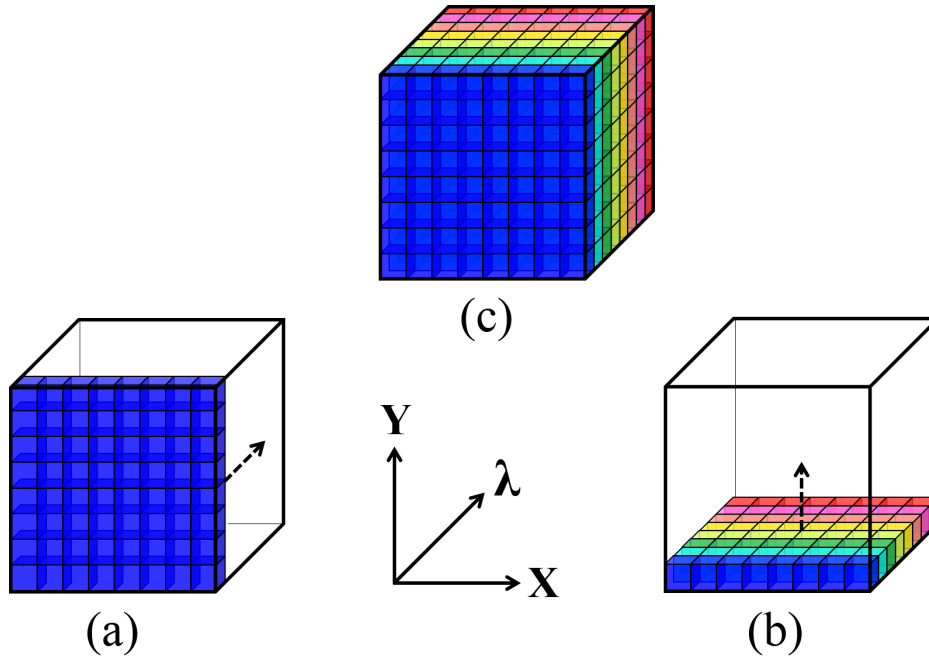


Fig. 1.1 Conceptual illustration of 3–D spectroscopy. Each method provides data cube as the final data product, but the scanning axis is different. The black dashed lines represent the scanning direction. (a) IFTS or FPI, scanning in the spectral direction. (b) long–slit scan, scanning in the spatial direction. (c) IFS observation with non–scanning (*i.e.* snapshot observation).

Among the above methods, IFS has higher observation efficiency and can be said to be suitable for the era of large telescopes, although the field of view of the IFS is relatively small ($\lesssim 1000 \square''$ for optical, and $\lesssim 100 \square''$ for near-infrared IFUs). Details of the configuration of specific optical system of IFUs will be described in Chapter 2.

In recent years, energy resolved detectors have also been developed in optical and infrared astronomy (Mazin et al., 2013). For the super-conductive detector devices, an incident photon is absorbed at each pixel and quasi-particles are generated. By counting the number of the particles we can measure the energy of the incident photon without using a dispersive element, and a data cube is generated. Such energy resolved detectors are commonly used in X–ray astronomy. In X–ray astronomy, a silicon CCD detector is also used which generates electron-hole pairs (exciton).

1.2 Spatially resolved study of Galaxies

Recent multi-wavelength observations reveal that the star formation activity of the universe peaks at the age of redshift $z = 1-3$ and it is ~ 30 times higher than that of the present universe (*e.g.* Hopkins and Beacom (2006)). The high star formation rate density is contributed by starburst galaxies with star formation rate of $10 M_{\odot}/\text{yr}$ or more (Goto et al., 2011, 2010). Therefore, the physical mechanism that triggers starburst activity is an important key in understanding galaxy evolution. IFS observations in the near-infrared wavelength is proved to be a powerful tools for that purpose, because it enable us to spatially resolve dusty star-forming region and the kinematics structure inside galaxies at the rest-frame optical wavelength. VLT/SINFONI observations of 11 $z \sim 2$ galaxies show that about half of them have experienced major merger by tracing the radial velocity and velocity dispersion field with the $H\alpha$ emission line (Shapiro et al., 2008). This result suggests that starburst may be induced by collisions between galaxies. A more detailed discussion is made from a large sample of about 60 galaxies (Förster Schreiber et al., 2009), where 1/3 is "rotation-dominated", 1/3 is "dispersion-dominated", and the remaining 1/3 is "interacting/merging system".

Other distant galaxy studies are carried out on the kinematic structure of clumpy star formation regions (Genzel et al., 2011), rotation curves (Förster Schreiber et al., 2006), and the Tully-Fisher relation (Cresci et al., 2009). IFS observations of distant magnified by gravitational lensing effect offer high-spatial resolution view (Jones et al., 2013; Wuyts et al., 2014). Future study on these distant galaxies is expected to reveal detailed spatial structure by IFS observations with extremely large telescopes.

Observations of nearby galaxies ($z \lesssim 0.1$) have an advantage of detailed spatial distribution of physical quantities (González Delgado et al., 2014). Using 8–10m class telescopes, it is possible to detect clumpy dust structures at a size of 200–300 pc within luminous infrared galaxies (LIRGs) even without adaptive optics (AO) (Piqueras López et al., 2013, 2012). The kinematic structure of the nearby galaxies is the key information to understand how the galaxies have evolved, and also is important to interpret observational results of distant galaxies. Another advantage of study on nearby galaxies is its capability to construct large samples. For instance, CALIFA survey obtain IFS data of ~ 600 objects (Müller-Sánchez et al., 2013), while SAURON/Atlas3D ~ 200 objects (Cappellari et al., 2011). Furthermore, the ongoing SAMI survey (Bryant et al., 2015; Cortese et al., 2016) and the MaNGA survey (Bundy et al., 2015; Yan et al., 2016) are planning to construct 5000–10000 IFS samples. These results will enables us to carry out statistical discussion with their large IFS datasets.

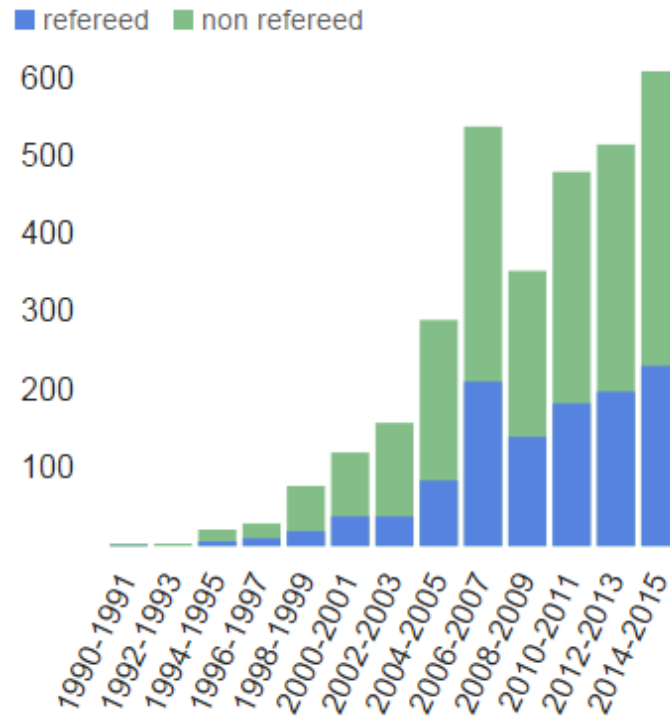


Fig. 1.2 Metric of published paper related to integral field spectroscopy. Blue and green bar shows number of refereed and non-refereed papers, respectively. The histogram is taken from *astrophysics data system* (ADS; <https://ui.adsabs.harvard.edu/>). The papers are counted from 1990 to 2015, which contain the keywords "integral field spectroscopy" or "integral field unit" or "integral field spectrograph."

1.3 Purpose and Approach

Obtaining spatially resolved spectra is increasingly important year by year in optical and near-infrared astronomy. Historically IFS observations began in optical wavelength (Adam et al., 1989; Pecontal et al., 1990). Near-infrared IFS observations are also essential for study of galaxy formation and evolution, because most of the key spectral features (*e.g.* $H\alpha$, $H\beta$, [OII], [OIII]) are redshifted to the near-infrared wavelength at $z > 1$. In addition, near-infrared observations are less affected by dust attenuation. Furthermore, since AO works effectively at this wavelength, high spatial resolution close to the diffraction limit ($\sim 0.1\text{--}0.2''$ for 8–4 m telescopes at K -band) can be achieved even from the ground-based telescopes. Fig. 1.2 clearly shows that IFS studies have been rapidly enhanced since 2000s, which corresponds to the emergence of the large 8–10m class telescopes such as Keck, Gemini, and VLT. The light-gathering power and angular resolution of these large telescopes offer powerful near-infrared IFS observations, and spatially resolved studies are greatly developed.

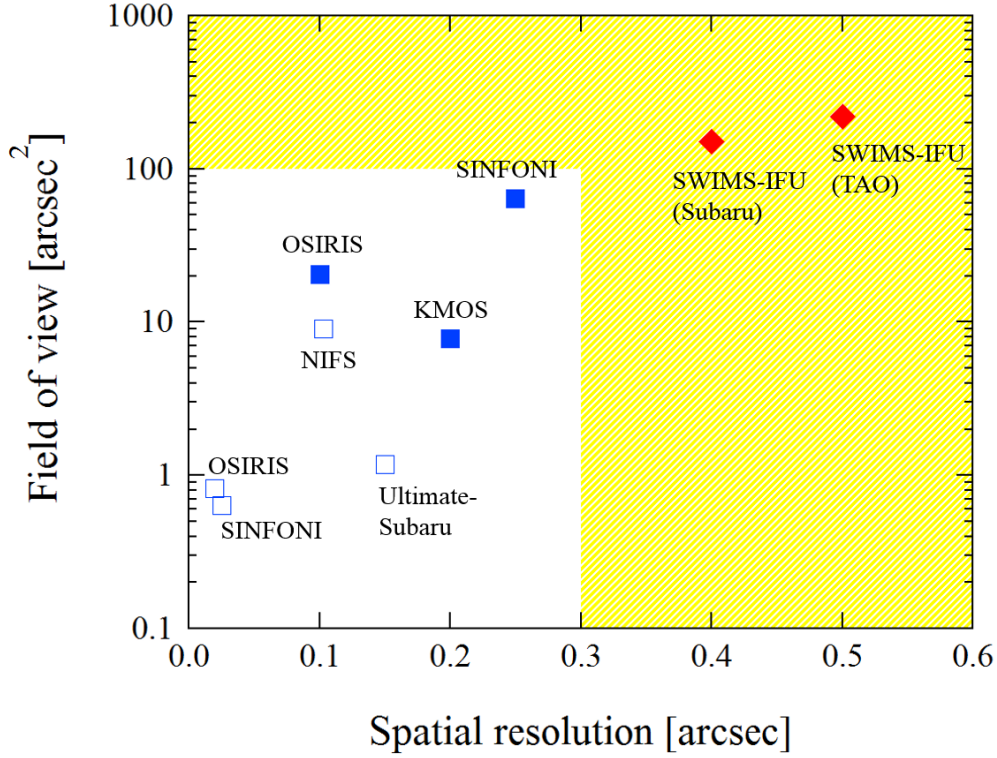


Fig. 1.3 Comparison of current and future near-infrared instruments with IFUs. The open and solid symbols denote the IFUs with and without AO facilities, respectively. The yellow shaded area represents an unexplored parameter space.

As shown in Fig. 1.3, the current near-infrared IFUs are specialized for fine spatial sampling for the purpose of AO observations. In case of same detector format, spatial sampling and the field of view are in a trade-off relationship. This fact means that only a data cube with a very narrow field of view can be obtained in the case of AO observation.

On the other hand, an IFU with mild spatial resolution and wider field of view is a powerful tool in the nearby universe, because sub-kpc resolution can be achieved at $z < 0.1$ even with a seeing-limited condition. However, Fig. 1.3 shows that there are no existing near-infrared IFUs meeting the above objectives. In other words, IFS observations with the wide field of view IFS observations optimized for seeing-limited condition is still an undeveloped parameter space.

In this thesis, we design and develop a new near-infrared IFU named SWIMS-IFU (Kitagawa et al., 2014), which has wider field of view ($\gtrsim 150 \text{ arcsec}^2$) and spatial sampling of $0.''4$ optimized for seeing-limited observations. It also enable us to acquire spectrum of $0.9\text{--}2.5 \mu\text{m}$ simultaneously. Since a near-infrared IFU with such a wide field of view and wide wavelength coverage has not existed so far, it realizes unique wide-field IFS observations.

For example, a comprehensive near-infrared IFS survey is new and enable us to spatially resolve dusty starburst galaxies in the nearby universe.

1.4 Constitution of the thesis

This thesis consists of the following two parts. Part I (chapter2–chapter7) describes development of SWIMS-IFU and fabrication of their optics. First, we propose concept of SWIMS-IFU. It is a module-like IFU, realizing IFS observations using an existing multi-object spectrograph. Next, we examine required specifications for realizing SWIMS-IFU and describe the optical design method of the image slicer type IFU. Furthermore, we apply state-of-the-art processing technique, *i.e.* ultra-precision cutting technique to fabrication of IFU mirror array. And we show the result of searching for optimum mirror material for infrared optics which needs cooling. At the end of part I, we summarize the experimental results.

Part II shows the result of AO-assisted imaging observation of nearby starburst galaxies, which spatially resolves the Pa α emission line map with a resolution of ~ 400 pc. Finally we summarize the results of the thesis and discuss future prospects using SWIMS-IFU.

Part I

The Development of SWIMS–IFU

Chapter 2

Introduction of Part I

2.1 Integral Field Unit

The method of realizing the IFU can be roughly divided into three optical systems(Allington-Smith and Content, 1998) as shown in Fig. 2.1, which are (a) micro lens array type, (b) fiber bundle type, and (c) image slicer type IFU. Each detail is as follows.

(a) Microlens array type A microlens array is an optical element in which small lenses ($< 1 \text{ mm}^2$) are arranged on a plane. In this method, the array is placed on a object image of the telescope. The image is divided into small section by the microlens array, and forms a group of small pupil images. The small pupil images enter the spectrograph, and their spectra are extracted on a detector plane. The maximum length of the spectrum that can be placed on the detector is determined by the size of the pupil image and the F value of the microlens array. In order to extend the longer spectral length, a microlens array should have a faster F value, although such microlens array is often difficult to manufacture. Therefore, this method is suitable for a science which does not require a long spectral length such as "wide wavelength coverage + low spectral resolution" or "narrow wavelength coverage + high spectral resolution" observations. An advantage of this method is that microlens array are used in various fields (*e.g.* optics for wavefront sensor, projection equipment, etc...) and are mature technology compared to the other IFU methods. Thus it is easy to design and manufacture the optical system. The covering factor of the detector is lower than that of the other methods, because the spectra have to be arranged on the detector plane so as not to overlap with each other. As an example of this type IFUs, there are Subaru/Kyoto3DII (Sugai et al., 2010), WHT/OASIS (Benn et al., 2003) and WHT/SAURON (de Zeeuw et al., 2000) in the optical, and Keck/OSIRIS (Larkin et al.,

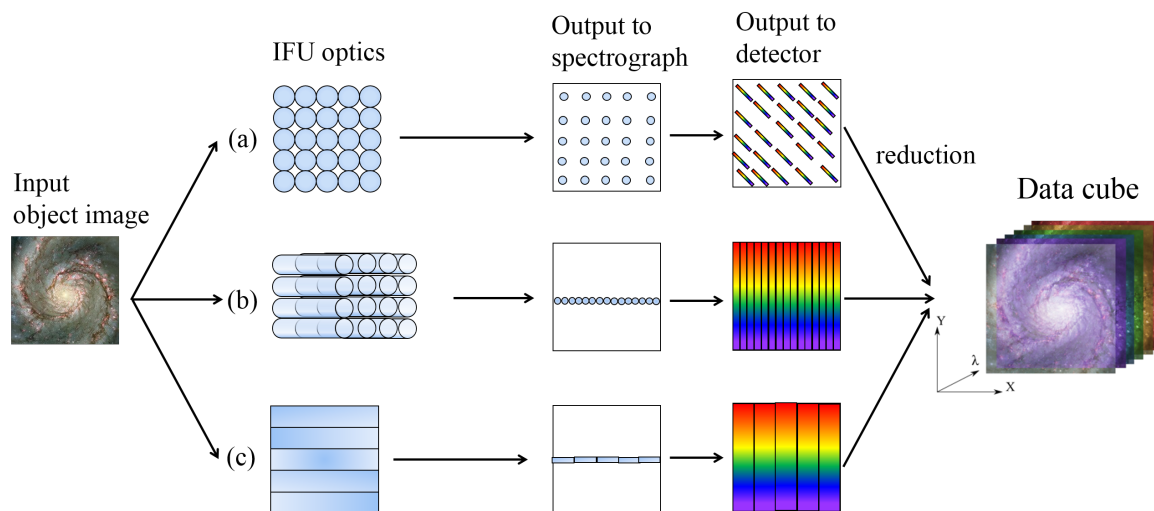


Fig. 2.1 Three methods used for integral field spectroscopy. (a) Microlens array type. (b) Fiber bundle type. (c) Image slicer type.

2003) in the near-infrared. OASIS uses a hexagonal shaped microlens, and SAURON and OSIRIS use a rectangular shaped.

(b) Fiber bundle type In this method, fibers are spread two-dimensionally on the telescope focal plane. Since fibers have flexibility, their other ends can be rearranged one-dimensionally at a slit of a spectrograph, and a spectrum of each region can be acquired. The advantage of this method is that since fibers have flexibility, there is a degree of freedom in arrangement of the instruments. On the other hand, since each fiber has a finite clad thickness, the spatial sampling should be discrete and filling factor is determined by core/cladding ratio of a fiber. It is empirically required to have a thickness of about 10λ in order to avoid crosstalk between neighboring clads. As a typical core diameter is $\sim 50\text{--}100 \mu\text{m}$, the filling factor will be $\sim 60\text{--}70 \%$. There is another problem called focal ratio degradation (FRD) where a F value of exit light from a fiber becomes smaller than that of the incident light. Combining a microlens array and fiber bundle together, FRD could be solved in some cases. In most cases, the fiber bundle is used in the optical wavelength, because fibers which can be used beyond $> 2 \mu\text{m}$ (*i.e.* at *K*-band) are not yet available. CAT/PMAS (Roth et al., 2000), Gemini/GMOS-IFU (Allington-Smith et al., 2002), HJST/VIRUS-P (Hill et al., 2008) are examples of this type of IFUs. PMAS and GMOS-IFU use microlens together.

(c) Image slicer type This type of IFUs use mirror arrays of complicated shapes. By placing an optical element called a slicing mirror or an image slicer on the telescope focal plane, a two-dimensional field of view is divided into a number of small slitlets. Then,

they are reflected at different angles and finally rearranged into a one-dimensional long pseudo-slit by other mirror arrays. The advantage of this method is that it is suitable for infrared instruments which requires cryogenic environment for the entire optical system. Since all the mirror arrays can be made of metallic materials in this type IFU, we can avoid thermal mismatch between optics and their support structures. Also, the image slicer type of IFUs have larger filling factor on the detector, because the slicing mirror continuously divides the field of view without losing the spatial information. As a disadvantage, each mirror array has complicated shape and faceted plane, so fabrications of these mirror arrays are highly challenging. Examples of IFUs that adopt this method are VLT/SINFONI (Eisenhauer et al., 2003), Gemini/NIFS (McGregor et al., 2003), KPNO/FISICA (Eikenberry et al., 2004), and VLT/KMOS (Sharples et al., 2004) in the near infrared, and VLT/MUSE (Bacon et al., 2010), Hale/CWI (Matuzewski et al., 2010), and WiFeS on the ANU 2.3-m telescope (Dopita et al., 2007).

The method to use are selected depending on observation wavelength and desired science. The microlens array and fiber bundle type of IFUs are often used in the optical. On the other hand, the image slicer method is often used in the infrared wavelengths. One of the reasons is because all the optical systems can be composed of metallic mirrors, and there is no need to consider the influence of thermal contradiction on optical alignment. Other reason is that the filling factor of the detector is the highest, so it can make efficient use of the detector whose price per pixel is high in the infrared. In an actual optical system, there is often a pre-optical system that enlarges/shrinks the telescope focal plane image.

2.2 Purpose of the Part I

Development of near-infrared IFUs has important meaning for the study on galaxy formation and evolution in the next decade. For instance, near infrared IFUs are being developed as a standard instruments for the next generation extremely large telescope (TMT/IRIS; ?) and the space telescope (JWST/NIRSpec; Posselt et al. (2004)). However, the number of available near-infrared IFUs is still small and their spatial sampling and field of view are limited in narrow region in the parameter space as shown in Fig. 1.3. This is because that there are difficulties of designing and fabricating of complicated optical elements used in an image slider type IFU which are standard selection for near-infrared wavelength..

In this study, we propose a new near-infrared IFU; SWIMS-IFU, and take the following approach to the above problems. We design SWIMS-IFU as a compact optical unit which realizes near-infrared IFS easily by installing the unit into the host multi-object spectrograph

(MOS). This enables us a highly efficient observation, because we can change each observation mode; the imaging, the long-slit spectroscopy, and the IFS spectroscopy in short period of $\sim 1\text{--}3$ minutes.

In order to fabricate complicated IFU mirror arrays, we adopt an ultra-precision cutting technique. Once the processing method has been established, it is possible to fabricate mirror arrays with good reproducibility. Establishment of fabrication method of the mirror arrays is a very important element technology to realize a multi-object IFU in the future.

In Part I, we first introduce the concept of SWIMS-IFU and determine the required specification in Chapter 3. The optical design method of image slicer type IFU and evaluation of optical performance are shown in Chapter 4. Then, we perform a proof-of-principle experiment to fabricate an slicing mirror using the ultra-precision cutting technique (Chapter 5). Also we explore which metallic alloys are optimal for cryogenic optics and show the experimental results (Chapter 6). Finally, we summarize the results of Part I and present a future outlook on IFU development in Chapter 7.

Chapter 3

Compact IFU with a Multi-Object Spectrograph

3.1 Concept of SWIMS-IFU

SWIMS-IFU is a new observation mode of SWIMS (Simultaneous-color Wide-field Infrared Multi-object Spectrograph) (Kitagawa et al., 2014; Ozaki et al., 2012). Since SWIMS is initially designed as an ordinary MOS instrument and fabrication of its opto-mechanical components have been already finished, our objective is to introduce IFS observation mode into SWIMS without any modification on the existing system. In order to achieve this goal, a compact and lightweight IFU is required, which works as a connector between the telescope and SWIMS by converting a two-dimensional field of view into a one-dimensional long pseudo-slit. We adopt “the advanced image slicer” layout (Content, 1997) used in GNIRS-IFU, for example (Allington-Smith, 2006; Dubbeldam, 2006).

3.2 Host spectrograph: SWIMS

SWIMS is one of the first generation instrument of the University of Tokyo Atacama Observatory (TAO) 6.5-m infrared telescope promoted by Institute of Astronomy, University of Tokyo (Yoshii et al., 2010). The TAO 6.5-m telescope is being constructed at the world’s highest astronomical site, the summit of Cerro Chajnantor (an altitude of 5,640 m) in northern Chile.

SWIMS is a two-color (0.9–1.4 μm /1.4–2.5 μm) simultaneous imager and MOS (Konishi et al., 2012; Motohara et al., 2016, 2014). Specifications of SWIMS are summarized in Table 3.1. The final F value of 12.2 of the TAO 6.5-m telescope matches with that of

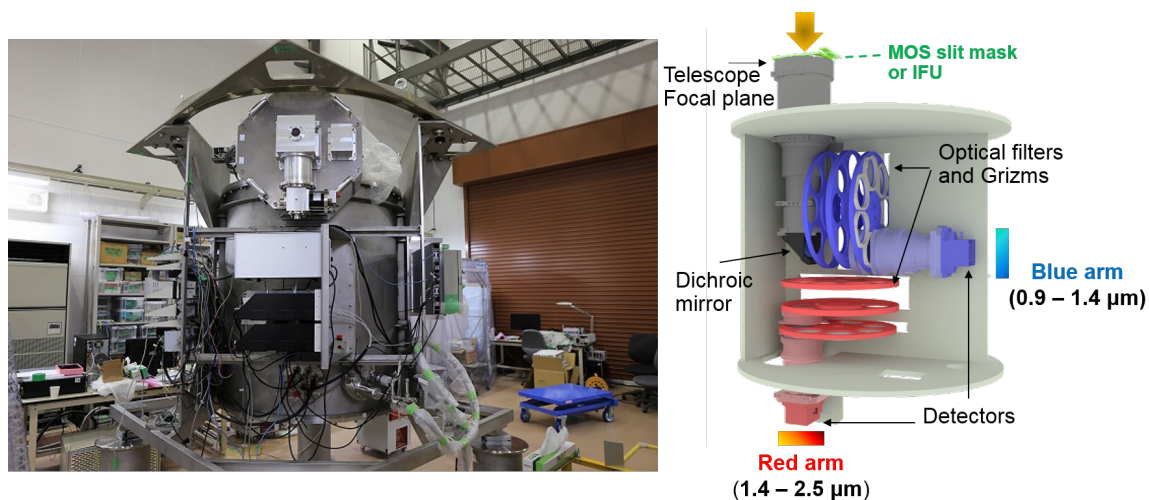


Fig. 3.1 *left*: Assembled structure of SWIMS components, which cryostat and the slit mask exchanger for MOS and IFS observation (see also Fig. 3.2). *right*: Layout of SWIMS optics with its optomechanics optimized for the Subaru telescope. The mask exchanger is not drawn in this figure. The incident light from the telescope is divided into the blue arm (0.9–1.4 μm) and the red arm (1.4–2.5 μm) with the dichroic mirror. Each camera lens is optimized for each wavelength band.

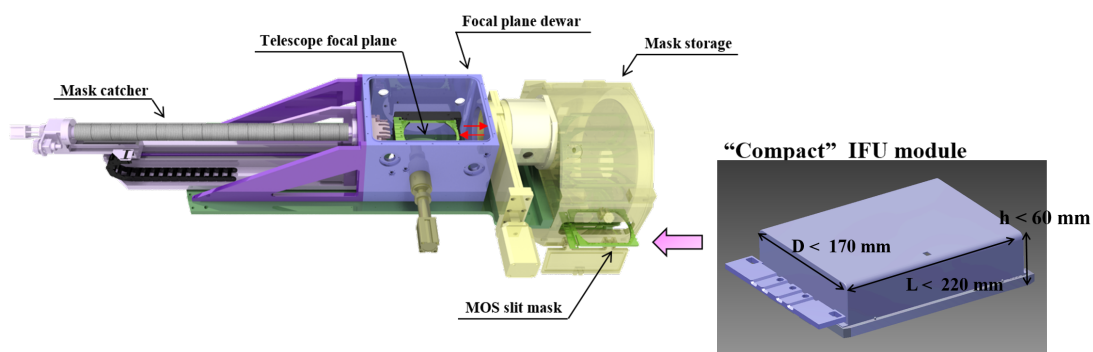


Fig. 3.2 The schematic view of the mask exchanger unit which can be also seen in the left panel of Fig. 3.1. The telescope focal plane is located in the focal plane dewar. The mask catcher drags a slit mask holder or an IFU from the mask storage and sets it on the telescope focal plane. The storage and the dewar are kept under cryogenic temperature (< 80 K) during observations (Takahashi et al., 2014).

the Subaru telescope at the Cassegrain focus with infrared secondary mirror. SWIMS can therefore be installed on the Cassegrain focus of the Subaru telescope, and we will conduct initial scientific observations (2017–2018) until the completion of the TAO 6.5-m telescope.

All the constituent parts such as the MOS unit, whole optics, and the cryostat have been completed, and it is in the final phase of operation tests (Motohara et al., 2016). The left panel of Fig 3.1 shows the SWIMS main cryostat. All the optical systems are housed in it, and are cooled down to about 100 K for the science operation. As shown in the right panel of Fig 3.1, the incident light from the telescope is split by the dichroic mirror into two wavelength ranges of 0.9–1.4 μm (Blue arm) and 1.4–2.5 μm (Red arm) , and finally re-imaged on the detectors through the camera lens. Filters are installed in each arm (see also Table 3.1) and two or four HAWAII-2 RG (H2RG) detectors are placed on each focal plane at the Subaru telescope or at the TAO 6.5-m telescope, respectively.

Table 3.1 Specifications of SWIMS

	TAO 6.5m	Subaru 8.2m
Observation Modes	"Two-color" Imaging and Multi-Object Spectroscopy (MOS)	
Wavelength Coverage	0.9–1.4 μm (<i>blue</i> arm) and 1.4–2.5 μm (<i>red</i> arm)	
Detector	HAWAII-2RG ^a (four arrays per arm) (two arrays currently procured for each arm)	
Field of View		
Imaging	8'.6 \times 4'.3 (ϕ 9'.6 ^b)	6'.6 \times 3'.3
Spectroscopy ^c	3'.7 \times 4'.3 (3'.7 \times 8'.6 ^b)	2'.8 \times 3'.3
Pixel Scale	0".126 pixel ⁻¹	0".096 pixel ⁻¹
Filters		
Broad-band	<i>Y</i> ($\lambda_c = 1.01 \mu\text{m}$), <i>J</i> (1.25 μm), <i>H</i> (1.64 μm), <i>K_s</i> (2.14 μm)	
Narrow-band	N129 ($\Delta\lambda = 40 \text{ nm}$), N133 (34 nm), N1875 (20 nm), N195 (40 nm)	
Grisms	<i>Blue</i> : 26.7 deg, 210 grooves/mm; <i>Red</i> : 22 deg, 110.5 grooves/mm	
Spectral Resolution (0".5 slit width)	<i>Blue</i> : $\lambda/\Delta\lambda \sim 700\text{--}1000$; <i>Red</i> : $\lambda/\Delta\lambda \sim 500\text{--}900$	
MOS Multiplicity	~ 20 masks excluding long slit masks, ~ 30 objects per mask	
Expected Total Throughput	Imaging: 31%; Spectroscopy: 20%	
Expected Limiting Magnitudes (in AB, 1hr, S/N=5) ^d		
Imaging	<i>Y</i> =25.0, <i>J</i> =24.2, <i>H</i> =23.5, <i>K_s</i> =23.8	<i>Y</i> =25.3, <i>J</i> =24.5, <i>H</i> =23.7, <i>K_s</i> =24.0
Spectroscopy ($\lambda/\Delta\lambda=1000$)	<i>Y</i> =23.3, <i>J</i> =22.4, <i>H</i> =22.2, <i>K_s</i> =21.9	<i>Y</i> =23.6, <i>J</i> =22.7, <i>H</i> =22.5, <i>K_s</i> =22.2

^a2048 \times 2048 pixels, 18 μm /pixel, long wavelength cut off at 2.5 μm .^bField of view covered with four HAWAII-2RG arrays (4096 \times 4096 pixels).^cField of view where the entire NIR (i.e., 0.9–2.5 μm) spectra can be obtained.^dMagnitudes for the case at the TAO are scaled from those at the Subaru by the difference of the telescope diameters.

Table 3.2 Specifications and Requirements of SWIMS-IFU

	TAO 6.5m	Subaru 8.2m
Observation mode	"Two-color" Integral Field Spectroscopy	
Wavelength Coverage	0.9–1.4 μm (<i>Blue</i> arm) and 1.4–2.5 μm (<i>Red</i> arm)	
Spectral Resolution	<i>Blue</i> : $\lambda/\Delta\lambda \sim 1000\text{--}1500$; <i>Red</i> : $\lambda/\Delta\lambda \sim 800\text{--}1400$	
Field of View	17.''2 \times 12.''8	14'' \times 10.''4 (14'' \times 5.''2 ^a)
Slice numbers (N)	26	26 (13 ^a)
Slice width (w)	0.''5	0.''4
Magnification factor (β)	$\times 2.6$	
Entrance and Exit F-number	12.2	
Expected IFU throughput	$> 70\%$ at $\lambda = 1\ \mu\text{m}$	
Weight ^b	$< 900\ \text{g}$	
Size	$D < 170\ \text{mm}$, $L < 220\ \text{mm}$, $H < 60\ \text{mm}$	

^a Field of view covered with two HAWAII-2RG arrays (4096×4096 pixels)

^b The upper limit including IFU optics and support structures

3.3 Specifications of SWIMS-IFU

3.3.1 Optical component

The specifications of SWIMS-IFU are summarized in Table 3.2. Some parameters are slightly different between at a use of the Subaru and TAO 6.5-m telescope due to the change of a pixel scale (see Table 3.1). As SWIMS is optimized for seeing-limited observation specification of the optics of the IFU should be also optimized for typical seeing on the summit of Mauna Kea and Cerro Chajnantor. We determine a sampling width per each slice (w) and a number of slice (N) a keeping a wide field of view and maximizing a covering factor of detectors.

First, considering a typical seeing at the summit of Mauna Kea and Cerro Chajnantor of 0.''4–0.''8, we set w to the value of the best seeing of $\sim 0.''4$. The determination of N is arbitrary. From the positional relationship shown in Fig. 3.3, the maximum length that can be used in the direction in which the pseudo slits are aligned is 188.5 mm. Then the actual length per slice becomes $(188.5/N)$ mm on the telescope focal plane. Using the plate scale of the Cassegrain focus at the Subaru telescope of $485\ \mu\text{m}/\text{arcsec}$, this value can be rewritten as $(389/N)''$. We have chosen $N = 26$, then the field of view of $0.''4 \times 15''$ can be assigned for one slice on the telescope focal plane. This corresponds to a situation in which each spectra is laid without gaps on the detector surface and in practice it is necessary to provide a gap

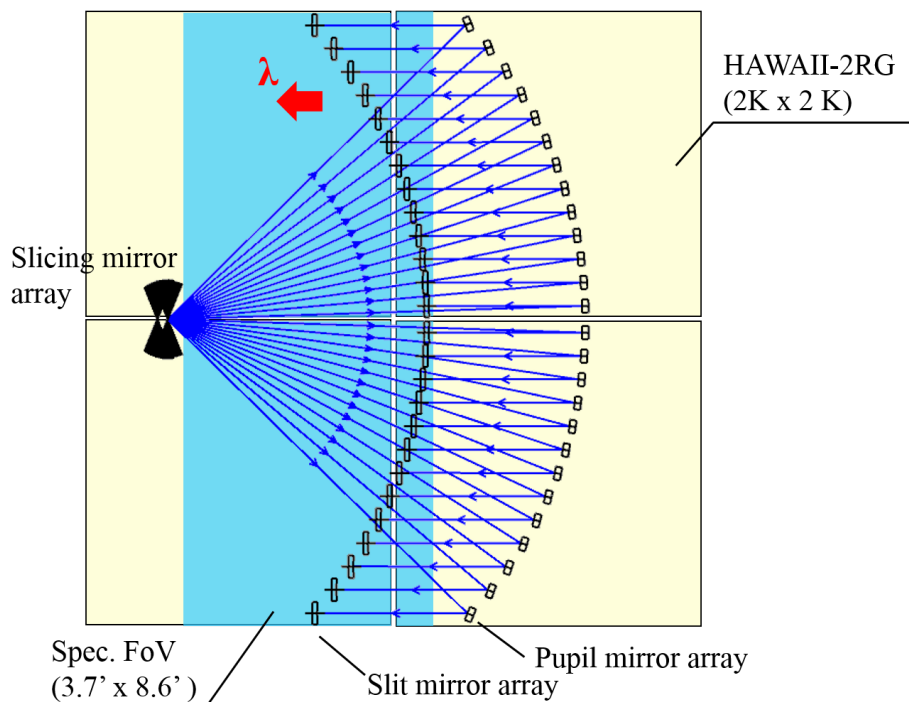


Fig. 3.3 Layout of the output slitlets of SWIMS-IFU according to both the telescope focal plane and the SWIMS detector plane. The four yellow squares represent HAWAII-2RG arrays covering the focal plane of the SWIMS. The area with cyan corresponds to the field-of-view where we can obtain entire near-infrared spectra between 0.9 and 2.5 μm . The red arrow indicates the direction of the spectral dispersion.

between each spectra so that adjacent spectra do not overlap. If we assume that the interval should be 10 pix (= 180 μm or 1.0'') on the detector surface, the final pseudo slit has a length of 14.''0 per slice, and the total field of view of the IFU becomes 10.''4 \times 14.''0 at the Subaru telescope.

Next, we determine a magnification factor β of the pre-optical system which enlarges the telescope focal image and output it to the IFU optics. We consider manufacturing feasibility of the slicing mirror array. Using a currently available ultra-precision cutting machine, a processable slice width is an order of 100 μm (*e.g.* Dubbeldam et al. (2012); Sakon et al. (2013)). Then, we adopt a moderate value of 500 μm as the actual slice width. Since the slice width of 0'4 corresponds to 194 μm before enlargement, β is 2.6 .

Finally, we calculate a covering fraction on the detector using the determined value. It is as high as 94 %, while we keep a wider field of view than that of any existing near-infrared IFUs. In the case of the TAO 6.5-m telescope, the parameters can be calculated in the same way using the pixel scale for the telescope shown in Table 3.1. These specifications for the IFU are set to the starting point of the optical design in Chapter 4.

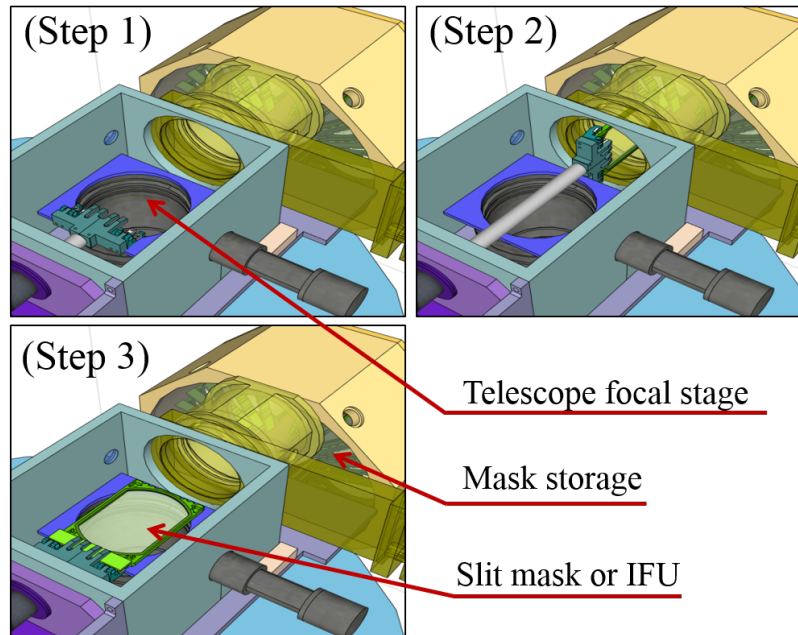


Fig. 3.4 Conceptual diagram of the MOS exchanging unit. (Step 1) The initial state corresponding to imaging observation. (Step 2) The catcher goes into the storage, grips the mask or the IFU, comes back to the focal plane, and (Step 3) puts the mask on the stage. The incident light from the telescope comes above.

3.3.2 Mechanical component

Fig. 3.4 shows how IFS observation mode can be realized by the mask exchanger unit. In order to handle the IFU and store it to the mask storage like a MOS slit mask, the size of the IFU needs to be almost the same as the slit mask. We assign a volume of two slit-mask holders to the IFU including support structure and optical components. This volume has width $D = 170$ mm, length $L = 220$ mm, and height $H = 60$ mm (the left panel of Fig. 3.5). When the IFU is placed on the focal plane, incident light from the telescope comes from a direction parallel to H . Note that the direction that gives the tightest restriction on the optical layout is H .

Weight of the IFU is also limited by a grasping power of the mask catcher which must handle the IFU between the mask storage and the focal plane without any trouble. We perform an experiment to measure the grasping power. Using a dummy mask of which weight can be adjusted by putting additional weight ($\Delta M = 7.0$ g) on the mask, the experiment is repeated five times with same load. The maximum load M_{\max} is defined as the weight where the catcher cannot lift the mask up from the focal plane. As the result, we estimate M_{\max} to be 1153 ± 70 g.

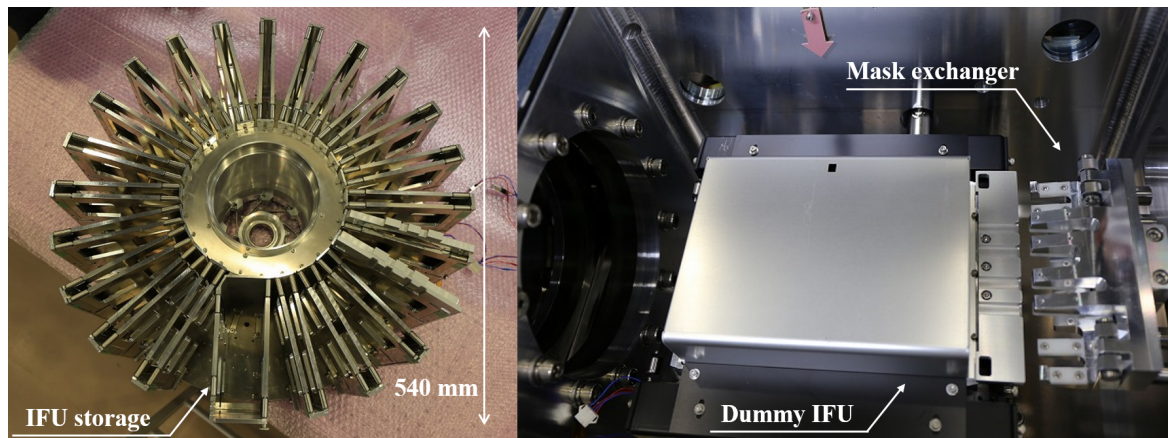


Fig. 3.5 (*left*) A carousel unit as a storage for MOS slit masks. A larger housing at the bottom side corresponds to the IFU storage. (*right*) Focal plane stage inside a MOS unit. The storage is located on the left side of the panel.

This result is confirmed by a dummy IFU whose weight is 908 g (right panel of Fig. 3.5). Using this dummy IFU, a repetitive test is performed again, where the catcher reciprocates 100 times in total between the IFU storage and the focal plane. It takes about 70 seconds to put the unit on the focal plane stage. We confirm that the dummy IFU can be handled without any problem. Therefore, the allowable maximum weight of the IFU is set to $M_{\text{IFU}} = 900$ g, which is the upper limit on the total weight including the IFU optics and the support structure.

Chapter 4

Optical design

4.1 Optical Components

In this chapter, we investigate whether possible optical solution exists for the specifications given in Table 3.2, and also describe how to design an optical layout of an image slicer type IFU.

The optical layout of SWIMS-IFU is shown in Figure 4.1, and the optical components and their abbreviation are defined as follows.

- *Pick-off mirror* (PO0) has a flat surface and introduces the incident rays from a telescope into the IFU. The entrance F-number is 12.2, which is the value at the Cassegrain focus of the Subaru telescope with IR secondary mirror, or at the Nasmyth focus of the TAO 6.5-m telescope.
- *Enlarger optics* consists of achromatizing lenses (PO1) and a concave spherical mirror (PO2). PO1 is a doublet lens using BaF₂ and S-NPH2 and suppresses chromatic aberration throughout the NIR wavelength (0.9–2.5 μm). PO1 and PO2 magnify the telescope focal plane image by a factor of 2.6 and reimage it on the slicing mirror array.
- *Slicing mirror array* (S1) divides the magnified image into 26 small slits and reflects them to corresponding pupil mirrors.
- *Pupil mirror array* (S2) is located at exit pupil positions of S1. It also converts the F ratio of the input rays to that of the telescope (*i.e.* F/12.2) and create “pseudo” slits.

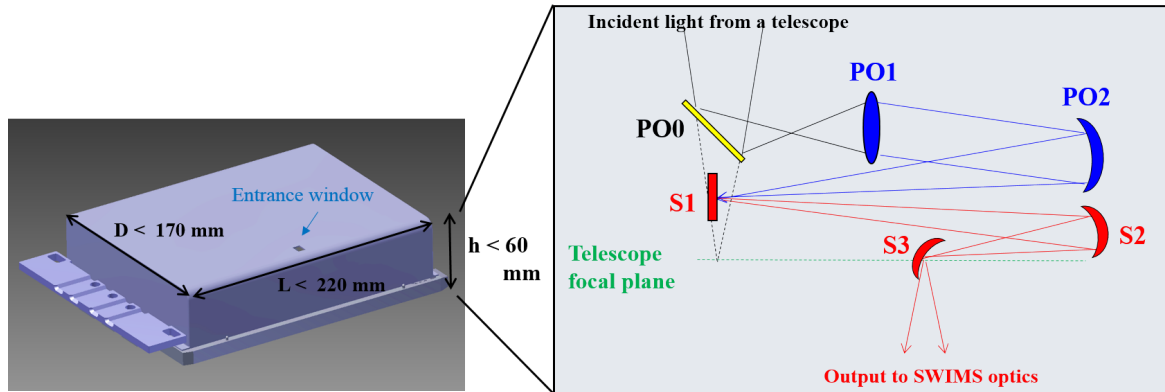


Fig. 4.1 Schematic view of the optical layout. Incident light (black lines) from a telescope is guided into the IFU by PO0. Then, the telescope focal image is enlarged by PO1 and PO2 by magnification factor of 2.6, and re-focused on S1 (represented by blue lines). S1, S2, and S3 convert the enlarged image into a group of small slits (slitlets), and reflects to the SWIMS spectrograph (red lines). S3 is located in the telescope focal plane. All optical components should be contained in the volume shown in the left image.

- *Slit mirror array* (S3) reflects the rays from S2 into the SWIMS main optics. It also matches the position and sizes of the exit pupils of the IFU to those of the cold stops inside the SWIMS optics.

Each component is numbered as follows : , *i.e.* $0 \equiv \text{PO0}$, $1 \equiv \text{PO1}$, $2 \equiv \text{PO2}$, $3 \equiv \text{S1}$, $4 \equiv \text{S2}$, and $5 \equiv \text{S3}$, respectively. Fig. 4.1 shows how these components should be aligned in the IFU.

The enlarger optics can be composed of at least two or more optical surfaces to obtain the desired magnification factor. Possible combinations are “mirror + mirror”, “lens + mirror”, or “lens + lens.” Because that the size tends to be large in the case of “mirror + mirror” system, and “lens + lens” has disadvantage in terms of chromatic aberration, we employ “lens + mirror” system.

In order to perform paraxial calculation we introduce a relationship between an object and an image at the given surface, and define its sign as shown in Fig 4.2. A definition of s_i , t_i , and f_i depicted in Fig. 4.2 are as follows.

- s_i : a distance from an i -th surface to an on-axis object point.
- s'_i : a distance from an i -th surface to an on-axis image point.
- t_i : the distance from an i -th surface to an entrance pupil.
- t'_i : the distance from an i -th surface to an exit pupil.

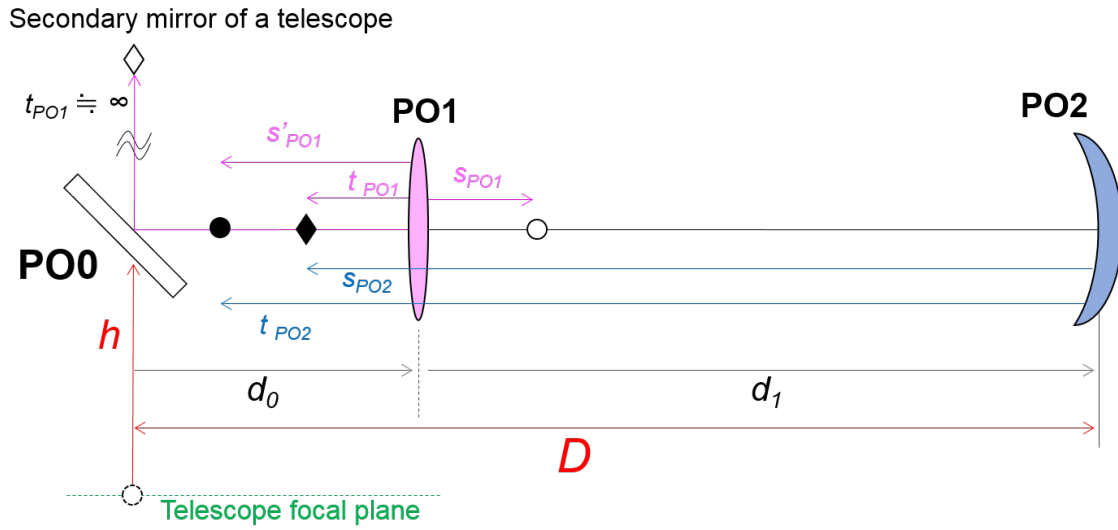


Fig. 4.2 Definition and arrangement of each symbol. The direction of each arrow coincides with the direction of the positive sign. Black open and filled circles indicate positions of an object and an image, respectively. Black open and filled diamonds indicate positions of an entrance and exit pupil, respectively. D is the width of the unit, and h is height of PO0 measured from the focal plane

- f_i : the focal length of an i -th surface at an image side.

An apex of i -th surface is taken as the origin of above quantities, and the traveling direction of the ray is defined as a positive direction. A sign of image height is positive when image position is above the optical axis. The unit of numerical values appearing in following discussion is measured in [mm] unless otherwise specified. For a certain optical i -th surface, two relationships about image and pupil positions hold as follows.

$$\frac{1}{s_i} - \frac{1}{s'_i} = -\frac{1}{f_i} \quad (4.1)$$

$$\frac{1}{t_i} - \frac{1}{t'_i} = -\frac{1}{f_i} \quad (4.2)$$

4.2 Paraxial calculation

4.2.1 Enlarger optics

We determine parameters of each optical surfaces by paraxial calculation. First, the following conditions are imposed on the paraxial calculations.

(Condition A) $d_2 = d_3 = D$

(Condition B) The surface shape of S1 must be flat.

d_i is distance from i -th surface to $(i+1)$ -th surface. Condition A is intended to monolithically fabricate each optical components, and greatly simplify the alignment procedure. Condition B make fabrication of the slicing mirror easier. This is important because fabrication of a slicing mirror with curved surfaces is very challenging.

From this conditions, we treat $s_{PO1} (\equiv x)$ as a free parameter of the optical system, and show that x is uniquely determined by giving fixed parameter of width (D), height (h) of the unit, and synthesis magnification of PO1 and PO2 (β). The following relationship holds from condition A.

$$\frac{1}{s_{PO2}} - \frac{1}{D} = -\frac{1}{f_{PO2}} \quad (4.3)$$

$$\frac{1}{t_{PO2}} - \frac{1}{2D} = -\frac{1}{f_{PO2}} \quad (4.4)$$

From these two equations the following equation is derived.

$$t_{PO2} = \frac{2D s_{PO2}}{2D - s_{PO2}} \quad (4.5)$$

Both s_{PO2} and t_{PO2} are negative from the definition of the sign. From Fig. 4.2 the range of s_{PO2} should be $-D \leq s_{PO2} \leq 0$, then

$$|t_{PO2}| \leq |s_{PO2}| \quad (4.6)$$

is always satisfied. It means that in order to make the exit pupil of PO2 at the back of the image of PO2, the entrance pupil of PO2 needs to be located closer than the object position (*i.e.* the exit pupil is located behind the image of objects with respect to PO1) \dots (i). By rewriting this as a condition for PO1, the conditions imposed on s_{PO1} and f_{PO1} become clear.

$$|t_{PO2}| \leq |s_{PO2}| \iff |s'_{PO1}| \leq |f_{PO1}| \quad (4.7)$$

Using this relationship, the following inequality is obtained.

$$\frac{1}{s_{PO1}} - \frac{1}{s'_{PO1}} = -\frac{1}{f_{PO1}} \quad (4.8)$$

$$\implies s_{PO1} = \frac{f_{PO1}s'_{PO1}}{f_{PO1} - s'_{PO1}} > 0 \quad (4.9)$$

Therefore, we can see that $s_{PO1} > 0$ is always satisfied. Then, (i) can be translated as follows: PO1 needs to be placed on the upstream (incident) side of the focal plane of the telescope in order to be located behind the exit pupil of PO2 image. . . (ii). At this time, the focal plane of the telescope becomes a virtual object point with respect to PO1. Rewriting (ii) with optical parameters, the following relation is obtained when h is height of PO0 measured from the focal plane (see also Fig. 4.2).

$$0 \leq s_{PO1} \leq h \quad (4.10)$$

Let us select s_{PO1} as a free parameter of the entire optical system of the IFU. In other words, we chose an expression which describes a change in the geometric arrangement of the IFU according to the position of PO1. From Fig. 4.2, we obtain the following formula.

$$s'_{PO1} = D - h + s_{PO1} + s_{PO2} \quad (4.11)$$

Also, as β_1 and β_2 are magnification factors of PO1 and PO2, respectively, the resultant magnification factor, β , can be written as follows.

$$\beta = \beta_1 \times \beta_2 \quad (4.12)$$

$$= \frac{s'_{PO1}}{s_{PO1}} \times \frac{s'_{PO2}}{s_{PO2}} \quad (4.13)$$

$$= \frac{D - h + s_{PO1} + s_{PO2}}{s_{PO1}} \times \frac{D}{s_{PO2}} \quad (4.14)$$

From the above results, s_{PO2} can be rewritten as a function of s_{PO1} .

$$s_{PO2} = \frac{D(D - h + s_{PO1})}{\beta s_{PO1} - D} \quad (4.15)$$

Therefore, calculating s_{PO1} from given constant D, h , and β , we can uniquely determine a parameter set of $[s'_{PO1}, f_{PO1}]$ and $[s_{PO2}, s'_{PO2}, t_{PO2}, t'_{PO2}, f_{PO2}]$. However, with this alone,

the exit pupil of PO2 is not necessarily formed at the distance of D behind the slicing mirror. Next we will think about this problem.

The distance between PO1 and PO2 is expressed as d_1 , and can be written as follows.

$$d_1 = |s_{PO2}| - |s'_{PO1}| \quad (4.16)$$

$$= |t_{PO2}| - |t'_{PO1}| \quad (4.17)$$

In general the second equality sign is not always satisfied. This can be thought as follows. We introduce a new parameter Δ , and define it as follows.

$$\Delta \equiv (|s_{PO2}| - |s'_{PO1}|) - (|t_{PO2}| - |t'_{PO1}|) \quad (4.18)$$

From this form Δ does not always satisfy $\Delta = 0$. As $t_{PO1} = \infty$, $\frac{1}{\infty} - \frac{1}{t'_{PO1}} = -\frac{1}{f_{PO1}}$, and $t'_{PO1} = f_{PO1}$, we can derive the following expression.

$$\Delta = s_{PO2} - s'_{PO1} - t_{PO2} + f_{PO1} \quad (4.19)$$

(ii) mentioned above is equivalent to $\Delta = 0$, and can be treated as follows. Let the actual placement length be \tilde{s}_{PO2} , \tilde{t}_{PO2} , from as in Fig. 4.2, we obtain the following equation.

$$\tilde{s}_{PO2} = t_{PO2} - (s'_{PO1} - t'_{PO1}) = t_{PO2} - s'_{PO1} + f_{PO1} \quad (4.20)$$

Therefore,

$$s_{PO2} - \tilde{s}_{PO2} = s_{PO2} - t_{PO2} - s'_{PO1} + f_{PO1} \quad (4.21)$$

$$= \Delta \quad (4.22)$$

In the same way, for the imaging relation of the pupil, the following equation is derived.

$$\tilde{t}_{PO2} = s_{PO2} - (s'_{PO1} - t'_{PO1}) = s_{PO2} - s'_{PO1} + f_{PO1} \quad (4.23)$$

thus,

$$t_{PO2} - \tilde{t}_{PO2} = t_{PO2} - s_{PO2} + s'_{PO1} - f_{PO1} \quad (4.24)$$

$$= -\Delta \quad (4.25)$$

Δ express a deviation between the theoretical value and the actual arrangement length about the object and pupil image of PO2.

Then, we define a function on x as follows.

$$F(x) \equiv -\Delta \quad (4.26)$$

$$= t_{PO2}(x) - s_{PO2}(x) + s'_{PO1}(x) - f_{PO1}(x) \quad (4.27)$$

$$= t_{PO2}(x) - f_{PO1}(x) + x + D - h \quad (4.28)$$

The second equality is transformed using $s'_{PO1}(x) = x + s_{PO2}(x) + D - h$. Then, $t_{PO2}(x)$, $f_{PO1}(x)$ in the expression can be written as a function of x as follows.

$$t_{PO2}(x) = \frac{2D s_{PO2}(x)}{2D - s_{PO2}(x)} \quad (4.29)$$

$$f_{PO1}(x) = \frac{x s'_{PO1}}{x - s'_{PO1}} = \frac{x[D - h + x + s_{PO2}(x)]}{x - [D - h + x + s_{PO2}(x)]} = -\frac{x[D - h + x + s_{PO2}(x)]}{D - h + s_{PO2}(x)} \quad (4.30)$$

$$s_{PO2}(x) = \frac{D(D - h + x)}{\beta x - D} \quad (4.31)$$

A specific expression of $F(x)$ can be written by the following equation.

$$F(x) = \frac{2D \frac{D(D-h+x)}{\beta x - D}}{2D - \frac{D(D-h+x)}{\beta x - D}} + \frac{x[D - h + x + \frac{D(D-h+x)}{\beta x - D}]}{D - h + \frac{D(D-h+x)}{\beta x - D}} + x + D - h \quad (4.32)$$

Solving $F(x) = 0$ for x using constant parameters of D , h , and β , we obtain following solutions.

$$x_1 = \frac{\beta(D - h) + D}{\beta(2\beta - 1)} \quad (4.33)$$

$$x_2 = h - D \quad (4.34)$$

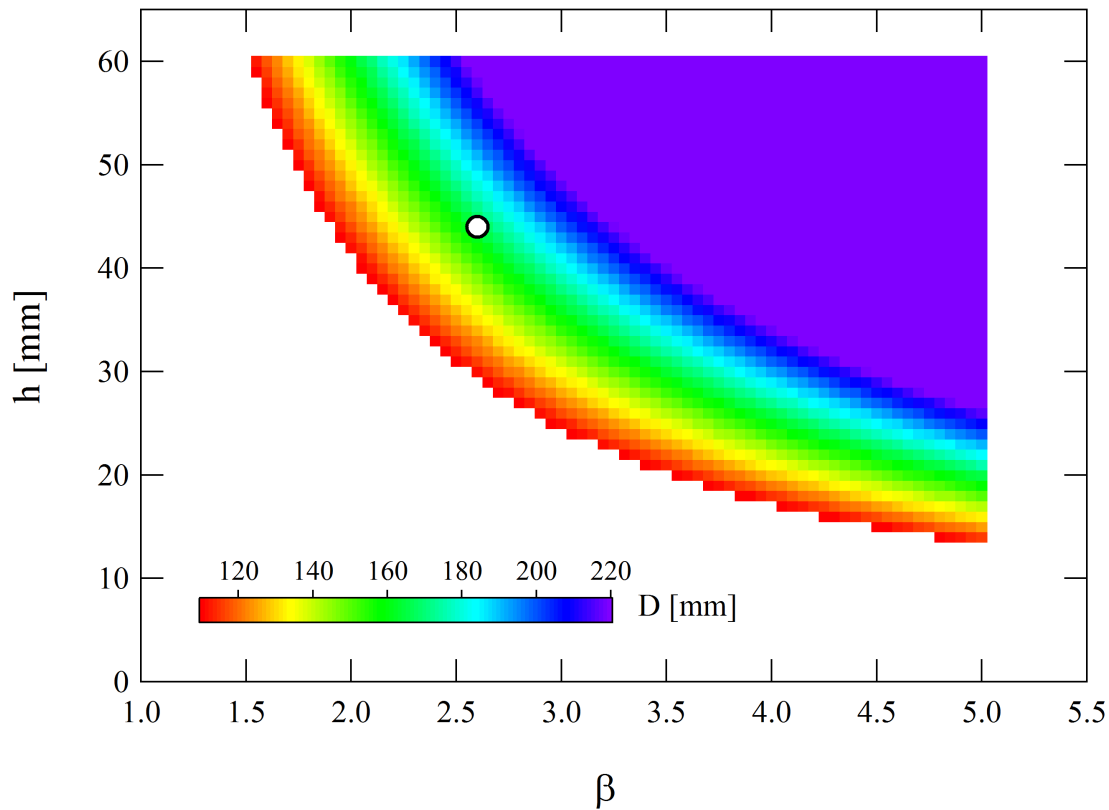


Fig. 4.3 The paraxial parameters which gives the solutions of $F(x) = 0$ with $0 < x < h$. The search ranges of each parameter are $D = 110\text{--}220$ mm, $h = 0\text{--}60$ mm, and $\beta = 0.0\text{--}5.0$, respectively. The white circle indicate the set of (D, h, β) we used for calculating the paraxial optical layout.

Since inequality of $D > h$ holds in the case of SWIMS-IFU, x_2 always takes a negative value. Therefore, the solution that satisfies $0 < x < h$ is only x_1 , in other words, we can uniquely determine the free parameter of $s_{PO1} = x_1$ by giving the fixed parameter of D, h, β .

Fig. 4.3 shows the result of searching the parameter with the range of $D = 110\text{--}220$ mm, $h = 0\text{--}60$ mm, and $\beta = 0.0\text{--}5.0$. Since whether a paraxial solution exists is not trivial, it is the important fact that there are solutions of $F(x)$ satisfying $0 < x < h$ within a realistic range of (D, h, β) . Using a solution obtained here we can construct a paraxial layout which satisfies the condition A and B. We adopt the values of $s_{PO1} = 35.678$ mm as the starting point of paraxial calculations obtained from $D = 140$, $h = 44$, and $\beta = 2.6$ (the white circle in Fig. 4.3).

Fig. 4.4 shows the calculation flowchart, and we can uniquely determine all the parameters of the enlarger optical system by giving the value of s_{PO1} .

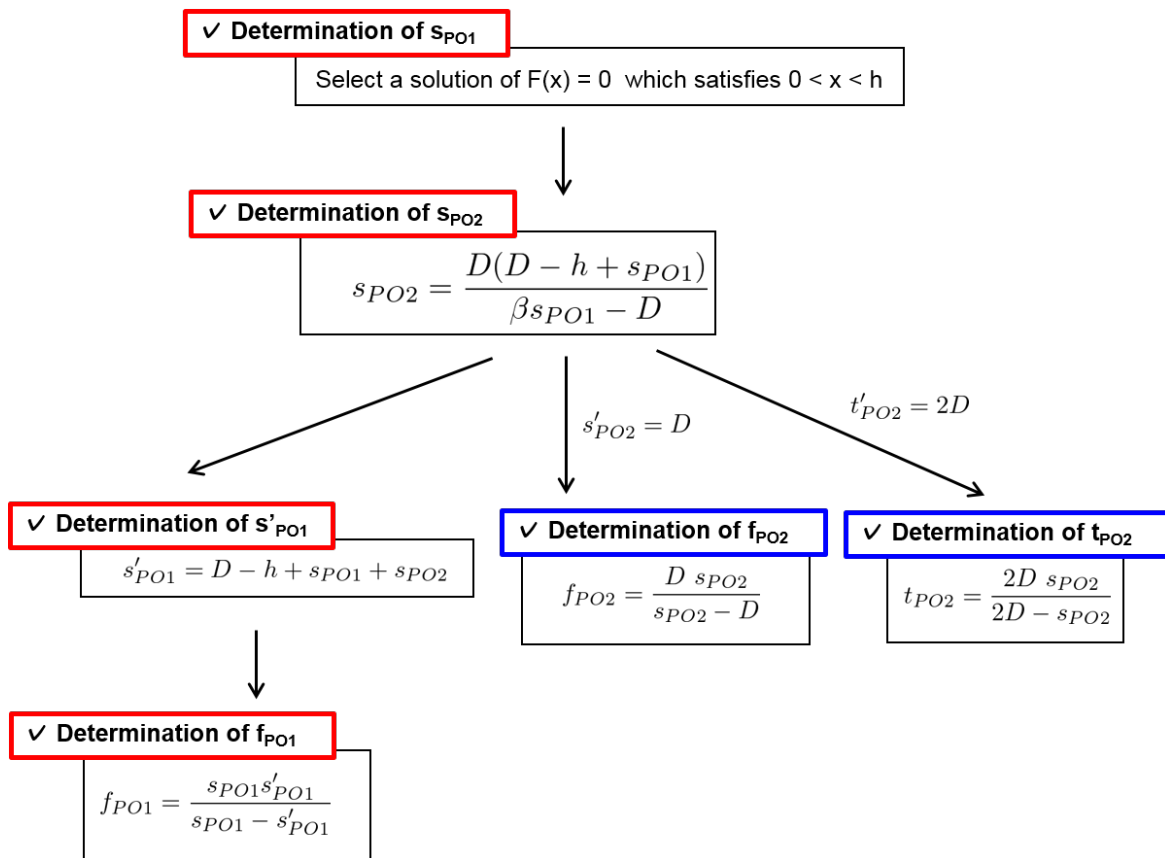


Fig. 4.4 Calculation flowchart of optical parameters of magnifying optical system. All values are uniquely determined by giving D , h , and β .

Table 4.1 Paraxial parameters of PO1 and PO2.

s_{PO1} [mm]	s'_{PO1} [mm]	f_{PO1} [mm]		
35.678	-258.577	-31.352		
s_{PO2} [mm]	s'_{PO2} [mm]	t_{PO2} [mm]	t'_{PO2} [mm]	f_{PO2} [mm]
-390.254	140.000	-163.030	280.000	103.037

Calculated parameters are summarized in Table ?? and Table ?. The enlarger system consists of a doublet lens with a concave power and a concave mirror. Each magnification factor is $\beta_{PO1} \sim -7.2$ and $\beta_{PO2} \sim -0.36$ calculated by the parameters in Table ?? and Table ?., and resultant magnification factor is $\beta = \beta_{PO1} \times \beta_{PO2} \sim 2.6$. They mean that PO1 expands the focal plane image excessively, and then it is reduced by PO2.

It is useful to convert the values in Table 4.1 into the distance between each surface (d_i) and the curvature of the surface (R_i) because these quantities are required for ZEMAX optimizations. We can calculate them by using following equations.

$$d_0 = h - s_{PO1} \quad (4.35)$$

$$d_1 = -(s_{PO2} - s'_{PO1}) = -(t_{PO2} - f_{PO1}) \quad (4.36)$$

$$R_i = 2f_i \quad (i = 1, 2) \quad (4.37)$$

The results are shown in Table 4.2.

4.2.2 IFU optics

Next, We determine parameters of the IFU optics. The distance d_4 between S2 and S3 and the curvature of each mirror can also be calculated from the values in Table ?. First of all, d_4 is determined from $d_4/d_3 = 1/\beta$ and $d_3 = D$ from the requirements to return the magnified image to its original size.

$$d_4 = D/\beta \quad (4.38)$$

A focal length of S2 can be calculated from the following equation.

Table 4.2 Paraxial parameters for ZEMAX optimization.

	d_i [mm] ^(a)	R_i [mm] ^(b)
PO0	8.322	<i>inf</i>
PO1	131.678	-62.704
PO2	140.0	-206.074
S1	140.0	<i>inf</i>
S2	53.846	-77.778
S3	–	-107.692

^(a) The thickness between the i -th and the $(i + 1)$ -th surface.

^(b) The radius of curvature of the i -th surface. The *inf* means the flat shape, and the minus sign means the concave shape.

$$\frac{1}{d_3} - \frac{1}{-d_4} = \frac{1}{D} + \frac{1}{D/\beta} = -\frac{1}{f_{S2}} \quad (4.39)$$

$$\therefore f_{S2} = -\frac{D}{1 + \beta} (< 0) \quad (4.40)$$

The initial value of the focal length of S3 can be calculated from the condition that the entrance pupil at the pupil mirror is moved to infinity.

$$\frac{1}{d_4} - \frac{1}{\infty} = \frac{1}{D/\beta} = -\frac{1}{f_{S3}} \quad (4.41)$$

$$\therefore f_{S3} = -\frac{D}{\beta} (< 0) \quad (4.42)$$

Since the curvature radius of the mirror is twice times of the focal length, both f_{S2} and f_{S3} are determined only by the width D of the IFU and the magnification factor β .

4.3 Optimization

We perform optimization of the whole system of the IFU using the ray tracing software Zemax. The obtained paraxial parameters are adopted as a starting point of optimization. The flowchart of the optimization is shown in Fig. 4.5. Optimizations are carried out in three steps. First, we optimize the enlarger optics (PO1 and PO2). Next, we deal with the parameters of S1–S3 which are the heart of the IFU. Finally, we evaluate the whole system including both the IFU and SWIMS optics.

Step 1 In the framework of the paraxial calculation, PO1 is modeled as an ideal thin lens, so in the ray tracing it is necessary to replace it with a lens of finite thickness. Since the wavelength coverage of SWIMS is wide (0.9–2.5 μm), chromatic aberration needs to be corrected for PO1. We adopt a doublet lens with a glass materials of BaF₂ with high transmittance in the infrared region and S–NPH2 (OHARA) suitable for chromatic aberration correction with high availability. The shape and the optimized parameters are summarized in Table 4.3. Each lens is as thin as 2–3 mm, and their fabrication process and a risk of breakage due to thermal cycling will be a subject to be studied in the future. By embedding this doublet lens (PO1) and the concave mirror (PO2) in the paraxial solution position, we confirm that the telescope focal plane image is enlarged by factor of 2.6, and focused on the position with distance of $D \sim 140$ mm from PO2. The curvature and the lens thickness of PO1 and PO2 are set to variables, and the composite magnification factor is fixed to $\beta = 2.6$. The merit function is optimized at the position of the slicing mirror. The optical parameters of the enlarger optics are fixed to the values obtained in Step1, and do not changed in the subsequent optimization.

Step 2 SWIMS-IFU divide the field of view into 26 slitlets, so 78 mirrors in total should be optimized and this is not easy tasks. We use a macro language and user-defined optimization functions in order to handle these multivariate optimization. A fan angle is the angle in the longitudinal direction of the slicing mirror, and a tilt angle is the angle in the horizontal direction. We set position of S2 and fan angle of S1 to variables, and position of S2 is fixed to pupil position of exit pupil of S1. After determining the arrangement of each channel for S2, we set a height of S3 to the telescope focal plane. Then, at the position of S3, the tilt angle of S2 and the position in the optical axis direction of S3 are optimized so as to minimize the spot radius. The tilt angle of S3 is adjusted so that the exit pupil for S3 matches with the position of cold stop in the SWIMS optics.

Step 3 Since the optical parameters of SWIMS such as the position of the cold stop cannot be changed, an exit F-number of the IFU optical system should be same as that of the telescope. These procedures are repeated until satisfying the deviation of pupil position at the cold stop is less than 10 %. The obtained optical layout after the optimization are shown in Fig. 4.6.

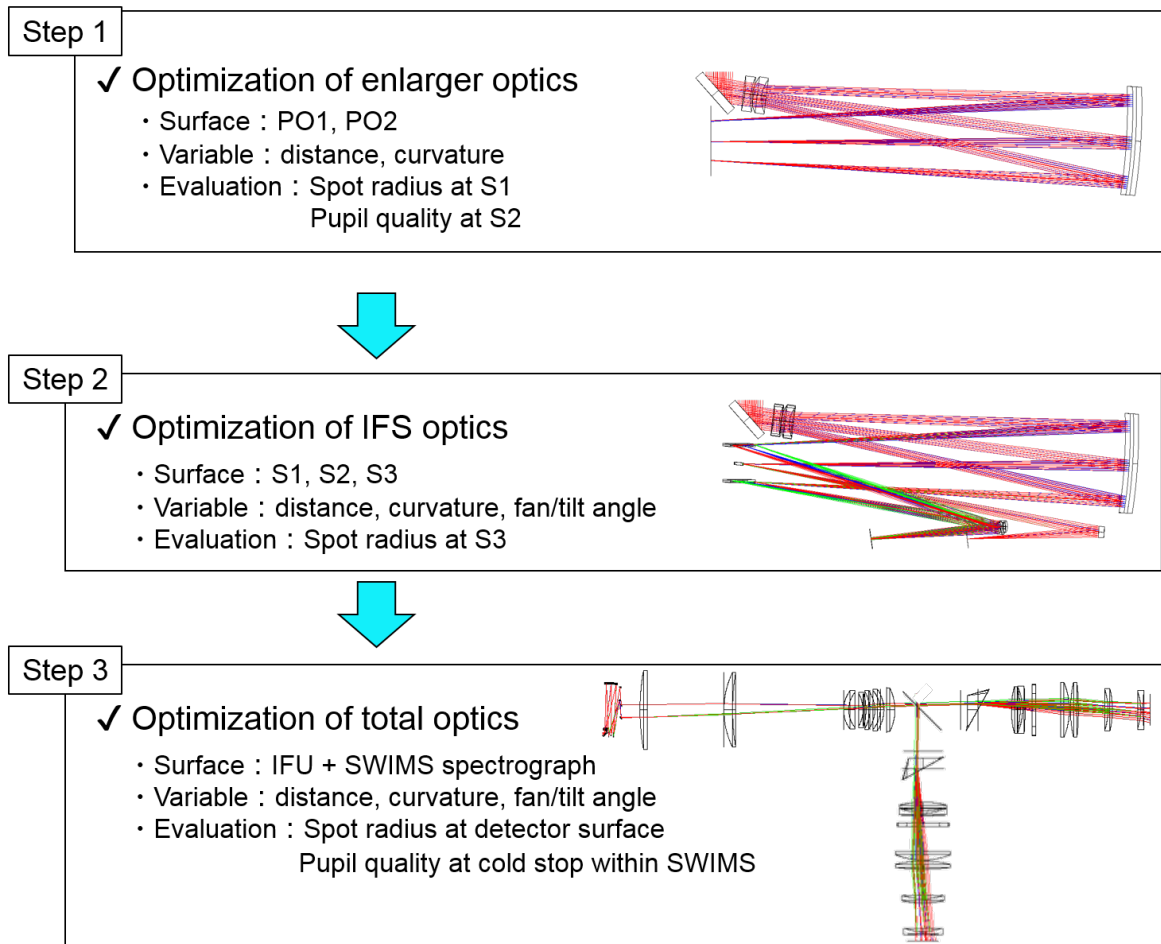


Fig. 4.5 Flowchart of optimization of the IFU.

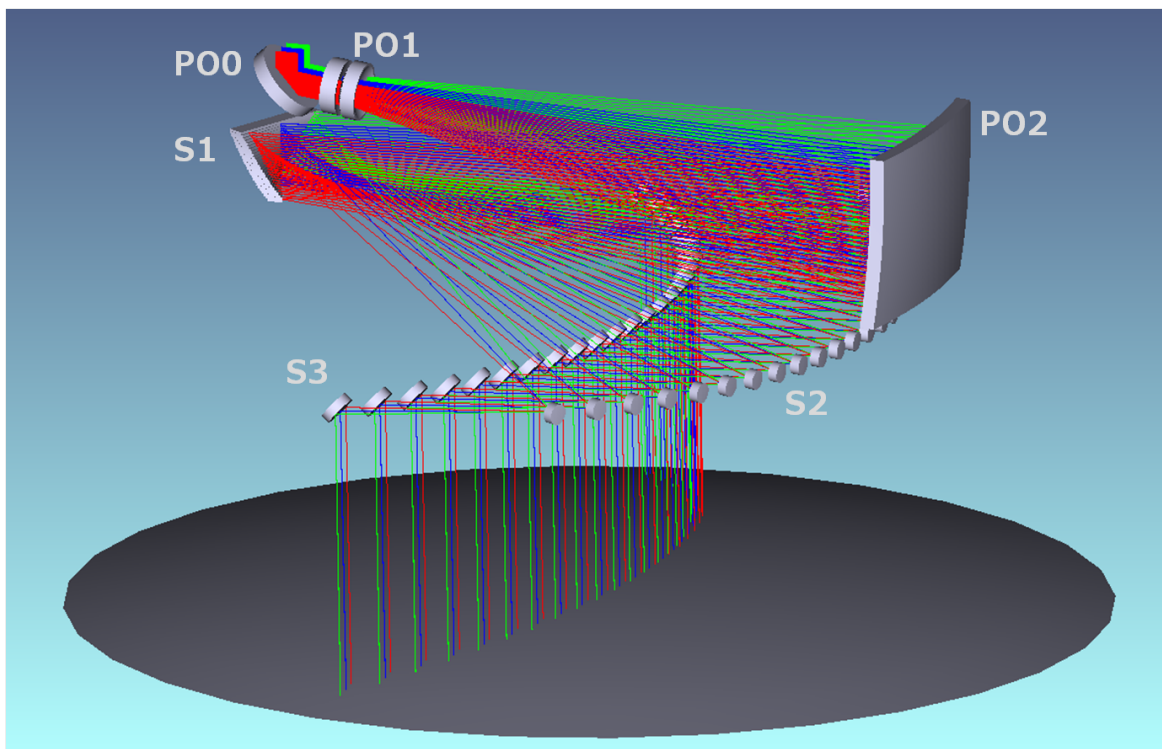


Fig. 4.6 Overall view of SWIMS-IFU. The incident light (upper left) from the telescope is guided into the IFU by PO0, the two-dimensional field of view is divided into twenty-six slitlets, converted into a one-dimensional slit and emitted to the SWIMS. The position of S3 is equal to the position of the telescope focal plane.

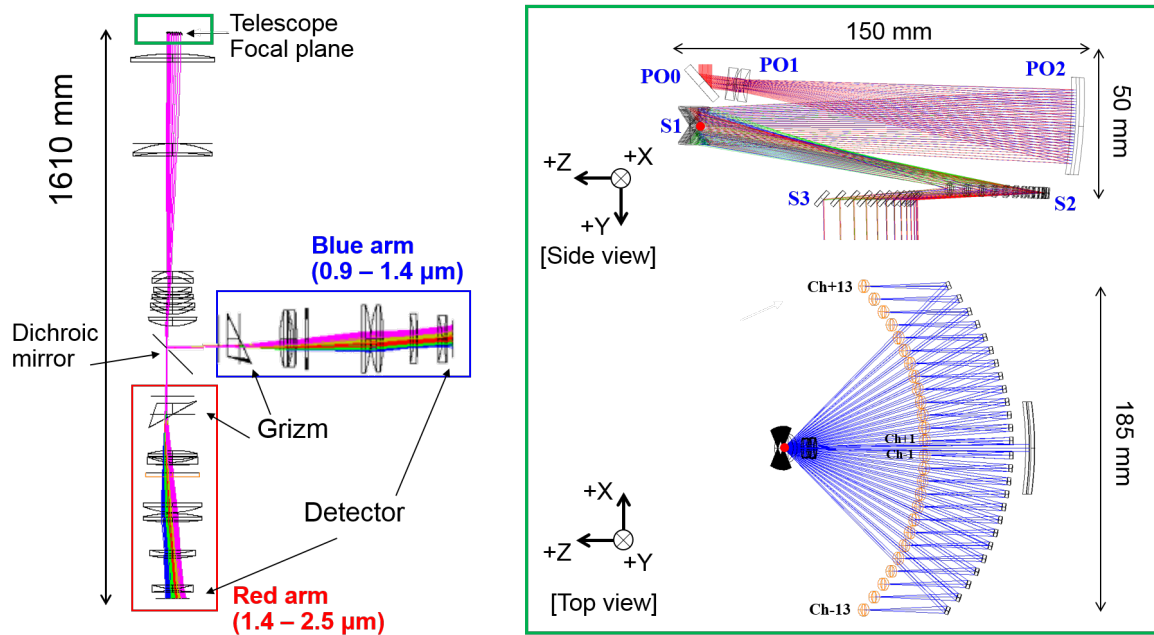


Fig. 4.7 Optical layout of SWIMS (left) and SWIMS-IFU (right). Green square represents the IFU. X-axis lies in the focal plane of the telescope and the Y-axis is chosen parallel to the optical axis of the telescope. Z-axis corresponds to the direction of propagation of light rays in the IFU. A “Ch xx” represents a symbol attached to each reflection surface of the mirror arrays, and the enlarged image is divided into 26 pieces from Ch−13 to Ch+13. The orange arc of the lower right is the rearranged slitlets corresponding to S3. It becomes an injection slit to SWIMS.

4.4 Results

4.4.1 Optical parameters

The final optical parameters and the coordinates after optimization are summarized in Table 4.3 ~Table 4.6. We define the coordinate system as follows. The X-axis lies in the focal plane of the telescope and the Y-axis is parallel to the telescope optical axis as shown in Fig. 4.7. In consideration of design and manufacture, we chose the reference point of the IFU (*i.e.* the origin of the coordinate system) as the center of the slice mirror located between Ch+1 and Ch−1 (the red circles in Fig. 4.7) The intersection of the focal plane and the optical axis of the telescope is located at $(0.000, +27.162, -67.492)$ with respect to the IFU reference point.

PO0 has a planar shape and introduces light from the telescope into the IFU. The magnifying optical system is composed of a doublet lens (PO1) and a spherical mirror (PO2). We introduce a doublet on one side of the enlarger optics to make the optical system compact.

This consists of biconcave (PO1-1) and meniscus (PO1-2) lens, and PO2 has a concave shape. PO1 and PO2 reimage the focal plane image at the position of S1 with synthesis magnification of ~ 2.6 . Since SWIMS acquires spectrum of wide wavelength band from $0.9 \mu\text{m}$ to $2.5 \mu\text{m}$ with one exposure, careful lens design to suppress chromatic aberration is required. As a result of considering various lens materials in combination, we adopt BaF_2 and S-NPH2 as achromatic lens material in the near-infrared wavelength. In order to take into account the refractive index at low temperature, we use the data obtained from experiments (Yamamuro et al., 2006).

S1, S2, and S3 are the heart of the IFU and consist of three mirror arrays. They divide the two-dimensional field of view into twenty-six slitlets and inject a rearranged slit image toward the SWIMS optical system. Each reflective surface from Ch-13 to Ch+13 shown in Fig. 4.7 has a planar shape in S1, and have concave spherical in S2 and S3. We use off-axis ellipsoid for Ch-13~Ch-7 and Ch+7 ~Ch+13 in S2. On the outer reflection surfaces of S2, the incident ray from S1 has a large incident angle, and is reflected to S3. This causes a large aberration on these reflective surfaces. In order to improve optical performance, we introduce an aspheric surface to S2. In consideration of ease of manufacturing and alignment, we decide to replace a part of the pupil mirror with an aspheric surface. These have the effect of greatly improving the imaging performance of the exit slit of the IFU as described in Section 4.4.3.

Table 4.3 Surface information and coordinates of pre-optical system

	Type	Radius of Curvature [mm]	Aperture [mm]	X [mm]	Y [mm]	Z [mm]	Tilt-X [degree]	Tilt-Y [degree]	Tilt-Z [degree]
PO0	Flat	–	15 × 15	0.000	-16.838	-2.492	-41.500	0.000	0.000
PO1-1 (front)	Biconcave	36.572	φ 12.0	0.000	-15.770	-11.187	7.000	0.000	0.000
PO1-1 (rear)	(BaF2)	-18.753	φ 12.0	0.000	-15.524	-13.192	7.000	0.000	0.000
PO1-2 (front)	Meniscus	-11.784	φ 12.0	0.000	-15.463	-13.689	7.000	0.000	0.000
PO1-2 (rear)	(S-NPH2)	-11.133	φ 12.0	0.000	-15.073	-16.865	7.000	0.000	0.000
PO2	Concave spherical	191.762	26 × 18	0.000	0.000	-139.627	3.500	0.000	0.000

Table 4.4 Surface information and coordinates of each channel of the slicing mirror array

Configuration	Type	Radius of Curv. [mm]	Aperture [mm]	X [mm]	Y [mm]	Z [mm]	Tilt-X [degree]	Tilt-Y [degree]	Tilt-Z [degree]
Ch-13				0.000	6.500	0.000	5.935	-22.028	2.233
Ch-12				0.000	5.980	0.000	5.851	-19.916	1.999
Ch-11				0.000	5.460	0.000	5.781	-17.923	1.785
Ch-10				0.000	4.940	0.000	5.723	-16.021	1.584
Ch-9				0.000	4.420	0.000	5.674	-14.193	1.395
Ch-8				0.000	3.900	0.000	5.632	-12.422	1.215
Ch-7				0.000	3.380	0.000	5.598	-10.698	1.042
Ch-6				0.000	2.860	0.000	5.569	-9.012	0.875
Ch-5				0.000	2.340	0.000	5.546	-7.355	0.712
Ch-4				0.000	1.820	0.000	5.528	-5.721	0.553
Ch-3				0.000	1.300	0.000	5.514	-4.106	0.396
Ch-2				0.000	0.780	0.000	5.505	-2.502	0.241
Ch-1				0.000	0.260	0.000	5.501	-0.906	0.087
Ch+1	Flat	-	0.52×18.2 (per Ch)	0.000	-0.260	0.000	5.501	0.906	-0.087
Ch+2				0.000	-0.780	0.000	5.505	2.501	-0.241
Ch+3				0.000	-1.300	0.000	5.514	4.102	-0.396
Ch+4				0.000	-1.820	0.000	5.528	5.715	-0.552
Ch+5				0.000	-2.340	0.000	5.546	7.344	-0.711
Ch+6				0.000	-2.860	0.000	5.569	8.995	-0.873
Ch+7				0.000	-3.380	0.000	5.597	10.674	-1.040
Ch+8				0.000	-3.900	0.000	5.632	12.389	-1.212
Ch+9				0.000	-4.420	0.000	5.673	14.149	-1.391
Ch+10				0.000	-4.940	0.000	5.721	15.965	-1.579
Ch+11				0.000	-5.460	0.000	5.779	17.851	-1.777
Ch+12				0.000	-5.980	0.000	5.848	19.826	-1.990
Ch+13				0.000	-6.500	0.000	5.930	21.917	-2.220

Table 4.5 Surface information and coordinates of each channel of the pupil mirror array

Configuration	Type	Radius of Curv. [mm]	Aperture [mm]	X [mm]	Y [mm]	Z [mm]	Tilt-X [degree]	Tilt-Y [degree]	Tilt-Z [degree]
Ch-13				91.125	22.828	-92.984	0.951	-22.202	0.000
Ch-12				83.875	23.162	-99.321	1.393	-20.062	0.000
Ch-11				76.625	23.448	-104.787	1.765	-18.046	0.000
Ch-10	Off-axis	~ 69	5.0×5.0	69.375	23.695	-109.514	2.086	-16.125	0.000
Ch-9	concave ellipsoid ^(a)			62.125	23.909	-113.597	2.369	-14.280	0.000
Ch-8				54.875	24.094	-117.103	2.621	-12.495	0.000
Ch-7				47.625	24.254	-120.084	2.849	-10.758	0.000
Ch-6				40.375	24.391	-122.579	3.056	-9.060	0.000
Ch-5				33.125	24.507	-124.618	3.246	-7.392	0.000
Ch-4				25.875	24.603	-126.225	3.422	-5.749	0.000
Ch-3				18.625	24.680	-127.415	3.586	-4.125	0.000
Ch-2				11.375	24.740	-128.201	3.738	-2.513	0.000
Ch-1				4.125	24.782	-128.591	3.881	-0.910	0.000
Ch+1	Concave spherical	70.0	5.0×5.0	-4.125	24.806	-128.561	4.014	0.910	0.000
Ch+2			(per Ch)	-11.375	24.811	-128.110	4.138	2.511	0.000
Ch+3				-18.625	24.798	-127.264	4.253	4.118	0.000
Ch+4				-25.875	24.768	-126.014	4.361	5.737	0.000
Ch+5				-33.125	24.719	-124.349	4.461	7.372	0.000
Ch+6				-40.375	24.651	-122.251	4.552	9.028	0.000
Ch+7				-47.625	24.561	-119.699	4.634	10.714	0.000
Ch+8				-54.875	24.447	-116.663	4.705	12.436	0.000
Ch+9				-62.125	24.308	-113.103	4.763	14.203	0.000
Ch+10	Off-axis	~ 69	5.0×5.0	-69.375	24.140	-108.971	4.805	16.028	0.000
Ch+11	concave ellipsoid ^(a)			-76.625	23.939	-104.197	4.827	17.926	0.000
Ch+12				-83.875	23.698	-98.689	4.823	19.916	0.000
Ch+13				-91.125	23.409	-92.318	4.781	22.027	0.000

^(a) We model an elliptical surface using a *conjugate*-type surface in Zemax, *i.e.*, both foci of the ellipsoid are located at the positions of S1 and S3. A calculated conic constant is ~ -0.20 .

Table 4.6 Surface information and coordinates of each channel of the slit mirror array

Type	Radius of Curv. [mm]	Aperture [mm]	X [mm]	Y [mm]	Z [mm]	Tilt-X [degree]	Tilt-Y [degree]	Tilt-Z [degree]
Ch-13			91.125	27.313	-46.357	41.660	0.000	0.000
Ch-12			83.875	27.313	-52.362	41.891	0.000	0.000
Ch-11			76.625	27.313	-57.595	42.081	0.000	0.000
Ch-10			69.375	27.313	-62.164	42.240	0.000	0.000
Ch-9			62.125	27.313	-66.140	42.374	0.000	0.000
Ch-8			54.875	27.313	-69.578	42.488	0.000	0.000
Ch-7			47.625	27.313	-72.520	42.584	0.000	0.000
Ch-6			40.375	27.313	-74.996	42.666	0.000	0.000
Ch-5			33.125	27.313	-77.030	42.734	0.000	0.000
Ch-4			25.875	27.313	-78.643	42.790	0.000	0.000
Ch-3			18.625	27.313	-79.846	42.834	0.000	0.000
Ch-2			11.375	27.313	-80.644	42.868	0.000	0.000
Ch-1			4.125	27.313	-81.053	42.891	0.000	0.000
Ch+1	65.0	7.0 × 7.0 (per Ch)	-4.125	27.313	-81.042	42.903	0.000	0.000
Ch+2			-11.375	27.313	-80.613	42.904	0.000	0.000
Ch+3			-18.625	27.313	-79.794	42.894	0.000	0.000
Ch+4			-25.875	27.313	-78.572	42.873	0.000	0.000
Ch+5			-33.125	27.313	-76.942	42.841	0.000	0.000
Ch+6			-40.375	27.313	-74.892	42.796	0.000	0.000
Ch+7			-47.625	27.313	-72.403	42.738	0.000	0.000
Ch+8			-54.875	27.313	-69.451	42.664	0.000	0.000
Ch+9			-62.125	27.313	-66.007	42.573	0.000	0.000
Ch+10			-69.375	27.313	-62.030	42.460	0.000	0.000
Ch+11			-76.625	27.313	-57.464	42.322	0.000	0.000
Ch+12			-83.875	27.313	-52.244	42.152	0.000	0.000
Ch+13			-91.125	27.313	-46.260	41.940	0.000	0.000

4.4.2 Size of the IFU

In SWIMS-IFU optical design, careful consideration is required to satisfy the size requirement. The most severe restriction on the optical system is the height of the IFU (parallel to Y-axis), and it is determined by the position of PO0. Therefore, through optimization, the position of PO0 is controlled to keep the value of paraxial calculation. In order to simplify the alignment of the optical elements, the constraint condition that each optical element is located at the end of the unit was imposed by paraxial calculation (see also Section 4.5.2).

Specifically, we optimize PO0 and PO2 so that they are located at both ends of the unit and that the distance between PO0 and PO1 is not too far, while keeping the synthesis magnification of PO0 and PO1 so as to be ~ 2.6 . In the same way, the position of S1 is adjusted to be almost beneath PO0, and the position of the pupil mirror is also optimized to be beneath PO2. Optimization is repeated so as to minimize the aberration while considering the arrangement of optical elements.

We verify the details of the size of the optical layout. Fig. 4.7 shows elevation and plane view of the optics of the SWIMS-IFU after optimization. The result demonstrates that all the optical surfaces are packed into volume of $D = 150$ mm, $L = 185$ mm, and $H = 50$ mm, respectively. This layout also satisfies the condition that each optical component (without S3) should be packed together at each side of the unit. It allows us to fabricate monolithically not only each mirror arrays but several components on the same side (*e.g.* PO2 and S2) and to reduce procedures of alignment by using high precision machining technique. As a result of optimization, we succeed in constructing an optical layout solution satisfying the size requirement sufficiently.

4.4.3 Optical Performance

Fig. 4.8 shows the spot diagrams at the slicing mirror. The diameter of the spot size is $\sim 0.''05$ at the center channel and $0.''08$ at the outer channel.

Fig. 4.9 is also shows that all the spot diameter at the slit mirror position. We adopt off-axis ellipsoid surfaces for pupil mirrors at Ch-13 \sim Ch-7 and Ch+7 \sim Ch+13 to improve the performance. In fact, we have improvement in the spot diameters at these channels compared with when they have spherical surfaces. At Ch-13 and Ch+13 which show the worst spot size with spherical surfaces, the spot diameters become $0.''3$ or less and are improved by $1/3$ with the non-spherical surfaces. This means it is necessary to use an off-axis ellipsoid surface in a channel at the outer side of the pupil mirror. In other words, about half of the 26 channels of the pupil mirrors should have off-axis ellipsoid surfaces.

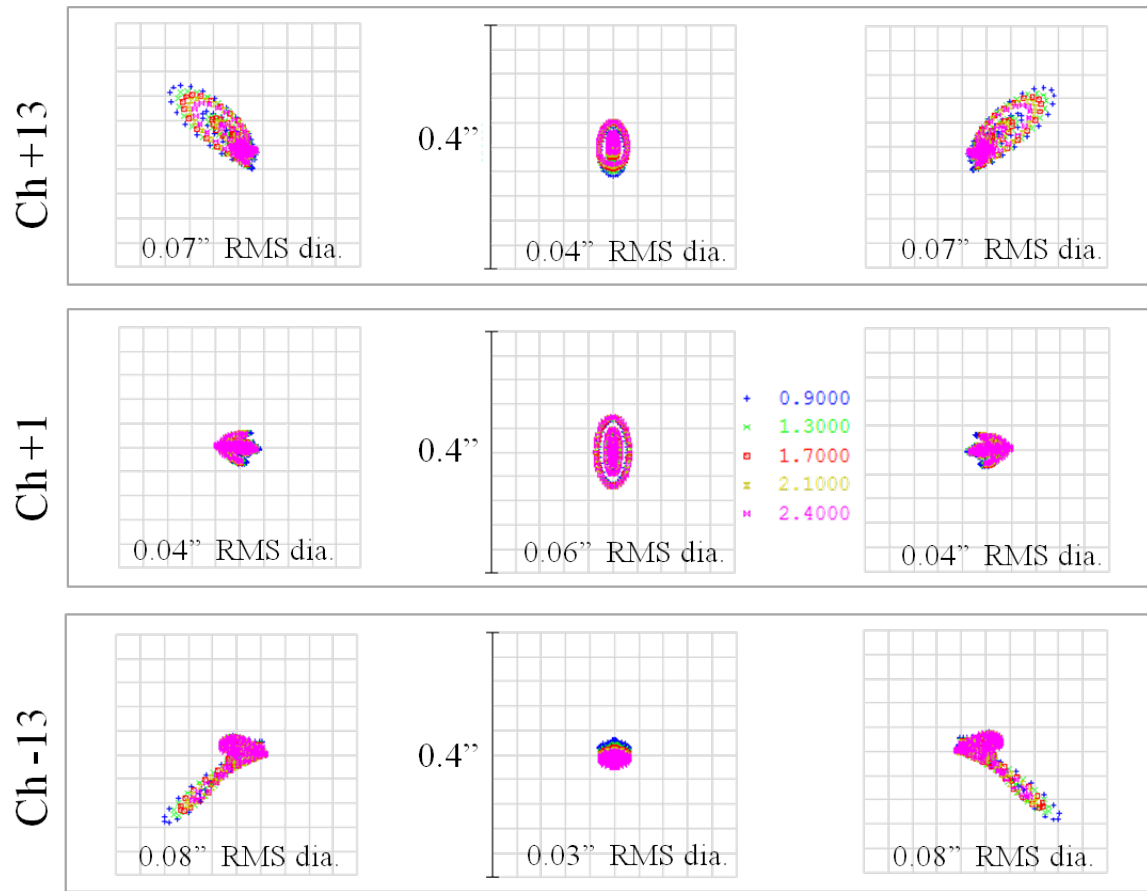


Fig. 4.8 Spot diagrams at the S1 (slicing mirror) position

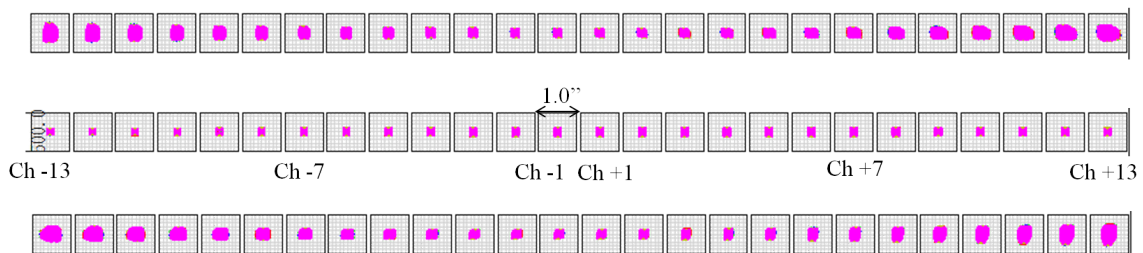


Fig. 4.9 Spot diagrams of all the channels at S3 adopting off-axis ellipsoid to Ch-13 ~ Ch-7 and Ch+7 ~ Ch+13 of S2 (pupil mirror). One side of the rectangle represents 1.0''. The upper row and the lower row show edge of the slitlets, and the middle row the center.

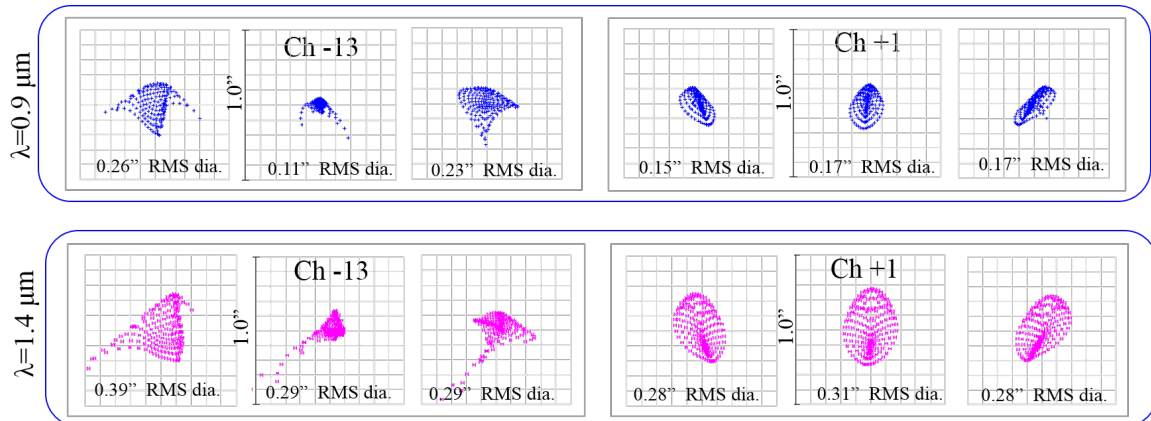


Fig. 4.10 Spot diagram at the detector of the blue arm of SWIMS. One side of the outer rectangle represents $1.''0$ ($= 10$ pixels) The upper row and the lower row show spots at $0.9 \mu\text{m}$ and $1.4 \mu\text{m}$, respectively.

Next, by connecting the IFU to SWIMS spectrograph as shown in Fig. 4.7, the imaging performance on the detectors is evaluated. We call the shorter wavelength side ($0.9\text{--}1.4 \mu\text{m}$) as “blue arm” and the longer wavelength side ($1.4\text{--}2.5 \mu\text{m}$) as “red arm”.

Spot diagrams at the detector surface are shown in Fig.4.10 and Fig. 4.11. The imaging performances of both arms tends to decrease with increasing wavelength. This is caused by the design of the SWIMS optics itself, and is independent of the nature of the IFU optics. Also, the spots worsen as going to the outer channel due to their large reflective angle at the pupil mirrors. The maximum spot diameter obtained is $0.''39$ which is approximately equal to the IFU spatial sampling. Considering that SWIMS-IFU will be used under seeing-limited condition of $0.''4 - 0.''8$ at the Subaru or the TAO 6.5-m telescope, this spot diameter is within allowable range . In other words, this image quality dose not significantly degrade spatial and spectral resolutions in the case of seeing-limited observations, although it may possible to make efforts to improve the spot diameter by reviewing the degree of freedom of the optical system. Based on the above results, the optical layout of this study satisfied the size requirement, and the final imaging performance is better than the spatial sampling of $\sim 0.4''$.

Finally we discuss the pupil alignment between the IFU and the cold stop within SWIMS. Since SWIMS-IFU is connected to the existing spectrograph, misalignment of pupil image will leads to a loss in light intensity and increase thermal background noise.

Fig. 4.12 shows the full field of view spot diagram at the pupil mirrors of position for $\text{Ch}+1$ and $\text{Ch}\pm 13$. From these results, good pupil image is obtained even at the outer channel of SWIMS-IFU. Using this as an entrance pupil for SWIMS-spectrograph, collimator lens of SWIMS make the exit pupil image at the cold stop position. Since the diameter and position of the cold stop in SWIMS are all fixed, it is necessary to fit the exit pupil of the SWIMS-IFU

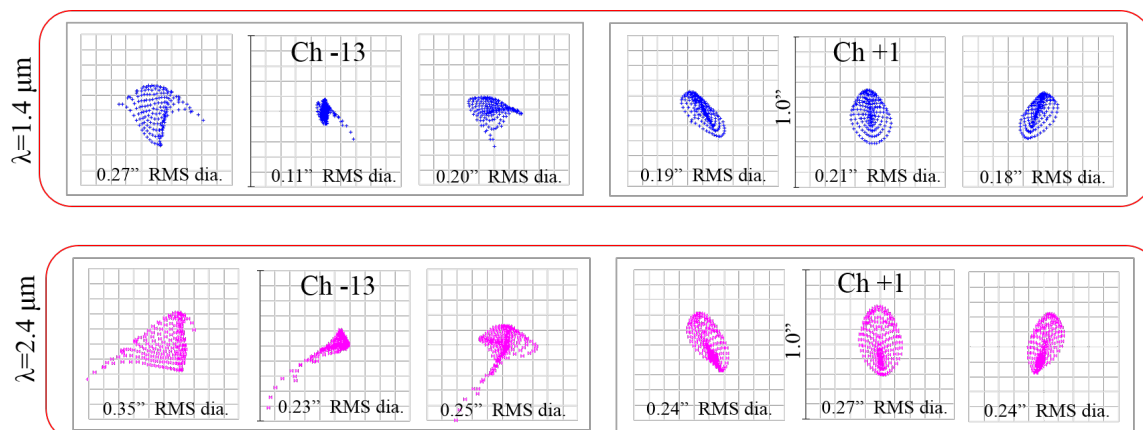


Fig. 4.11 Spot diagram at the detector of the red arm of SWIMS. One side of the outer rectangle represents $1.''0$ ($= 10$ pixels) The upper row and the lower row show spots at $1.4\mu\text{m}$ and $2.4\mu\text{m}$, respectively.

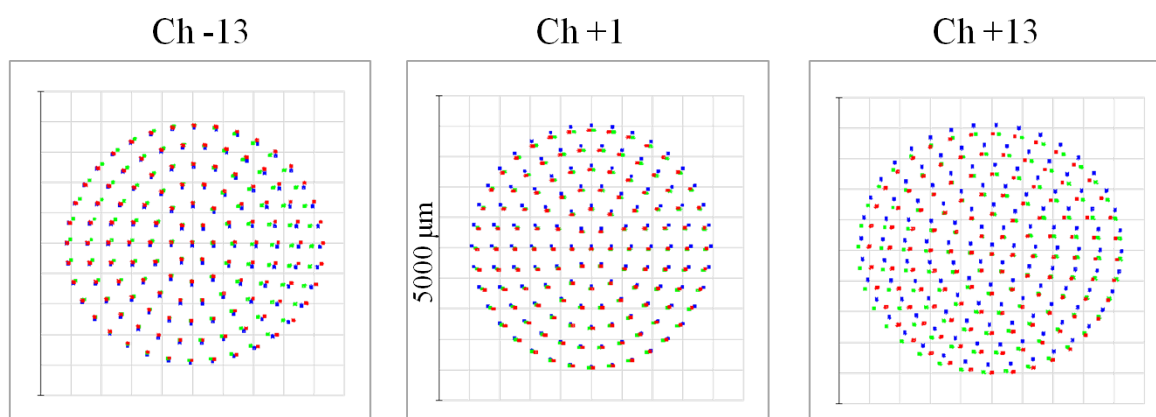


Fig. 4.12 A full field of view spot diagram at S2 (pupil mirror) position. Blue is the pupil image of the center of the view, while red and green are those at the edge of the slitlets.

well there. The result is shown in Fig. 4.13. At the $\text{Ch}\pm 13$, the pupils of the edge and center of the slitlets are not at the same position, and mismatch with the cold stop, which result in light loss at the cold stop of $\sim 12\%$.

4.5 Tolerance estimation

4.5.1 Tolerance values of each component

In this section, we estimate how much error is allowed for each optical element. First of all, we perform sensitivity analysis. In Section 4.4.3, we identify that the worst degradation of

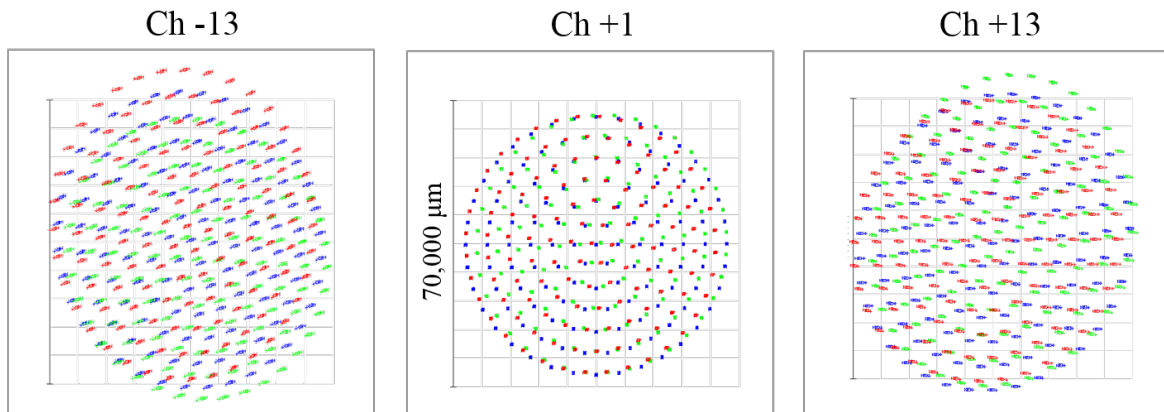


Fig. 4.13 A full-field spot diagram at the cold stop position within SWIMS. Blue is the pupil image of the center of the view, while red and green are those at the edge of the slitlets.

spot size occurs at the edge of Ch–13. Thus, it is possible to obtain the most severe value of error for all channel by estimating the tolerance for Ch–13.

We give deviations of translation ($\Delta X, \Delta Y, \Delta Z$) and rotation (R_X, R_Y) and shape error of the optical surface to each optical element, and estimate how much defocusing occurs. Since the optical element without S2 has an axisymmetric shape, it is not necessary to consider the rotation around the Z-axis. For S2 using off-axis ellipsoid, it is confirmed that defocusing occurring in the range of $R_Z = \pm 0.01$ degrees is negligible.

Table 4.7 summarizes the defocus ratio for each deviation when giving $\pm 50 \mu\text{m}$ for translation, ± 0.01 degrees for rotation, and $0.1 \mu\text{m}$ P-V for shape error. In the magnifying optical system, the contribution of PO2 is the largest. Shape error and deviation in the X-axis and Z-axis directions produce defocus of 6–8%. The mirror array generally produces a large amount of error, which is a contribution of $\sim 65\%$ of the total. This result clearly shows that high precision manufacturing and alignment is necessary for these optics. For S1, it is sensitive to the shape error and the angle error around the Y-axis, each contributing $\sim 10\%$. S2 has the largest contribution among all the optical elements, and an aberration of 6–10% is generated from the shape error and the deviation in Y-axis and the Z-axis direction, respectively. S3 is sensitive to the deviation of both X-axis and Y-axis, resulting in defocusing of 6–8%. Based on the results of the sensitivity analysis, we can estimate which deviations contribute significantly to each optical element.

Next, we determine the tolerance value for each optical element. Ch–13 has the maximum spot size of $0.''4$ on the detector plane, and we define the maximum allowable spot size as $0.''5$. In other words, the sum of defocus amounts generated from each optical element needs to be kept within $0.''1$.

Table 4.7 Sensitivity analysis for Ch–13

	Shape error	$\Delta X^{(a)}$	$\Delta Y^{(a)}$	$\Delta Z^{(a)}$	$R_X^{(b)}$	$R_Y^{(b)}$	Defocusing ^(c)
Given error	0.1 ^(d) [μm]	± 50 [μm]	± 50 [μm]	± 50 [μm]	± 0.01 [degree]	± 0.01 [degree]	–
PO0	0.2	0.0	0.0	0.0	2.4	1.5	4.2
PO1-1	0.1	3.1	0.8	0.6	0.1	0.1	4.9
PO1-2	0.0	3.6	0.7	4.2	0.1	0.2	8.9
PO2	3.6	6.9	0.5	3.5	2.0	0.0	16.5
S1	10.2	0.0	0.0	1.0	2.3	6.5	20.0
S2	10.3	0.3	8.6	6.3	1.8	0.1	27.3
S3	0.4	6.4	8.3	0.1	1.7	1.3	18.2
						Sum	100.0%

^(a) Deviation in X, Y, and Z-axis direction. The definition of each axis is shown in Fig. 4.7.

^(b) Rotation around X and Y-axis. Since each optical element is axisymmetric, rotation around the Z-axis is not considered.

^(c) Percentage of defocus under each error.

^(d) The value in peak-to-valley.

Tolerance values of each optical element determined based on the results of sensitivity analysis are shown in Table 4.8. These values include both manufacturing tolerance and assembly error. We allocate $\sim 40\%$ to the fore optics and $\sim 60\%$ to the three mirror arrays as error budget. An accuracy of $\pm 40 \mu\text{m}$ is typically required for the translational direction. Especially for specific degrees of freedom of PO2, S2, and S3, we require an accuracy of $\pm 20 \mu\text{m}$ since they are sensitive to translational error. Regarding the angular error, an accuracy of ± 0.01 degrees is set as a required value. Considering manufacturing feasibility, shape error is set to $0.1 \mu\text{m}$. The sum of defocus arising from these deviations is estimated to be $0.1''$ from ray tracing, which agrees with the required value.

We define the accuracy shown in Table 4.8 as the requirement for IFU. These values are based on the analysis for Ch–13 where the aberration is the worst, and can be regarded as the most severe requirement accuracy. Fabrication with this accuracy has already been realized in the existing near-infrared IFU such as VLT/KMOS (Dubbeldam et al., 2012), and it is considered to be sufficiently achievable. Particularly by using monolithic processing by ultra-precision processing, fabrication errors and alignment of each facet in a mirror array can be achieved within the required accuracy.

Table 4.8 Tolerance table of each component

	Shape error [μm]	ΔX [μm]	ΔY [μm]	ΔZ [μm]	R_X [degree]	R_Y [degree]	Defocusing [arcsec]
PO0	0.1	± 40	± 40	± 40	± 0.01	± 0.01	0.01
PO1-1	0.1	± 40	± 40	± 40	± 0.01	± 0.01	0.01
PO1-2	0.1	± 40	± 40	± 40	± 0.01	± 0.01	0.01
PO2	0.1	± 20	± 40	± 20	± 0.01	± 0.01	0.01
S1	0.1	± 40	± 40	± 40	± 0.01	± 0.01	0.02
S2	0.1	± 40	± 20	± 20	± 0.01	± 0.01	0.02
S3	0.1	± 20	± 20	± 40	± 0.01	± 0.01	0.02
					Sum		0.10

4.5.2 Alignment Strategy

We describe the strategy of alignment of optical elements within the IFU. We will monolithically fabricate not only each surface in mirror arrays, but also each optical elements in the unit. As shown in Fig. 4.14 same color means that the optical surfaces will be fabricated from one piece of alloy. Number of components can be dramatically reduced, and there are only three-components (red, blue, and green one in Fig. 4.14) to be aligned in the unit. The alignment of each optical surface in a component can be determined by machining accuracy ($< 1 \mu\text{m}$). The position of each component is fixed by position-adjusting pins with thin spacer to adjust moderate offset. These strategies reduce alignment process and provide high-precision alignment.

The supporting structure of the SWIMS-IFU and each mirror are made of CTE-matched special aluminum alloy described in Chapter 6. Assuming that all components in the IFU are isotropically shrunk under a uniform temperature distribution, alignment of the optical axis adjusted at room temperature will not deviate greatly even at low temperatures. For the doublet lens of the magnifying optical system, the influence of heat shrinkage is considered to be sufficiently small as compared with the assembly error and manufacturing tolerance since the diameter ($\sim \phi 10 \text{ mm}$) is small.

4.5.3 Throughput Estimation

In order to evaluate a throughput of the IFU, we consider two contributions to a throughput of a mirror. One is scattering due to an unevenness on a surface and the other is reflectance determined by a refractive index of a material. This can be modeled as follows (Ogilvy, 1987).

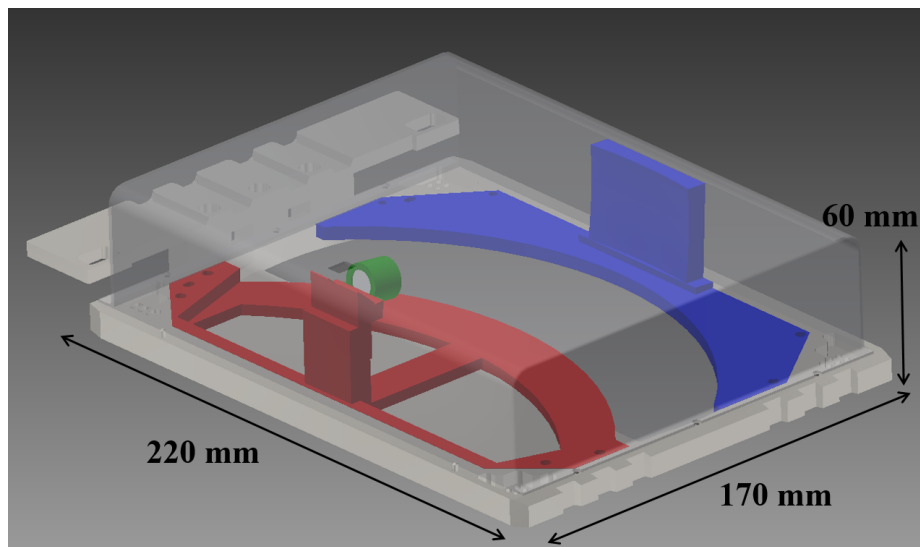


Fig. 4.14 A CAD image of conceptual design of SWIMS-IFU structure. The size of the unit is $60 \times 170 \times 220 \text{ mm}^3$. The image is false-colored and the same color means *one* optical component. A housing of the unit is made transparent for the purpose of illustration, and the actual parts will be painted in black in near-infrared to avoid stray light. The red component is a combination of PO0, S1, and S3 while the blue component is a combination of PO2 and S2. The green cylinder is represented as the lens barrel (PO1) of the magnifying optical system.

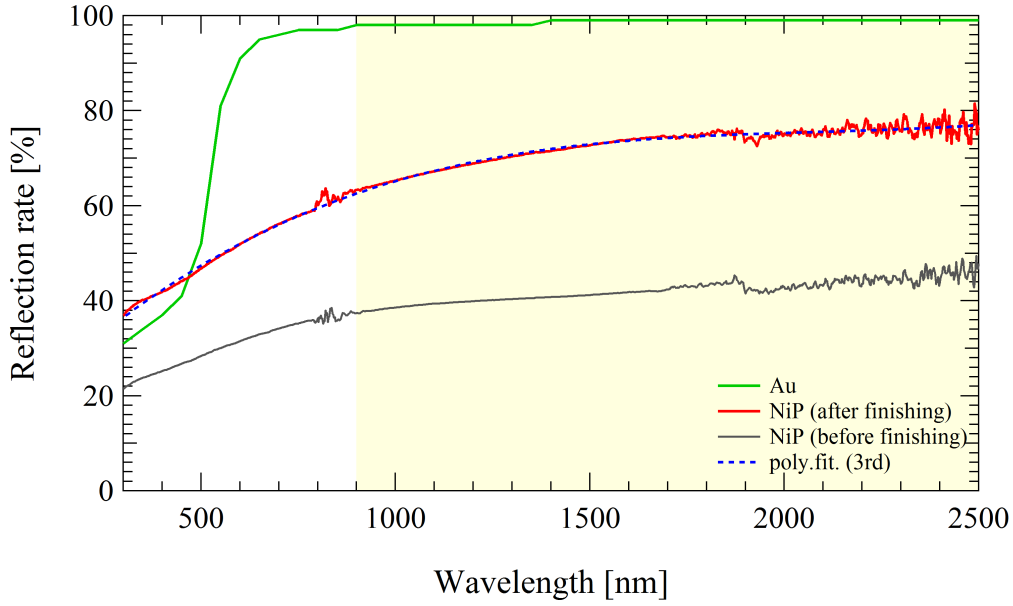


Fig. 4.15 The measured reflection of NiP surface mirror. The yellow filled area shows the wavelength range of SWIMS. The ripples seen at ~ 800 nm and ~ 1800 nm are caused by the exchange of detectors. The curve of finished workpiece (2nm rms) is fitted with a cubic function and results is as follows. $R = 15.01 + 0.082544 \lambda - 3.8578 \times 10^{-5} \lambda^2 + 6.1892 \times 10^{-9} \lambda^3$.

$$R = R_0 \exp \left[-8(\pi\sigma \sin \theta / \lambda)^2 \right] \quad (4.43)$$

R_0 is the ideal reflectance (*i.e.* there is no roughness or shape error) of the mirror material. λ and θ is wavelength and incoming angle of incident light, respectively. σ represents a root-mean-square roughness (rms) measured in the same unit as the wavelength. The exponential term is Debye-Waller factor that represents a scattering effect due to the surface roughness. Since λ and σ are on the order of $\sim 1 \mu\text{m}$ and $\sim 0.001 \mu\text{m}$ in our application, respectively, we can assume that $\sigma/\lambda \ll 1$. By assuming $\theta = 0$ (*i.e.* light comes into the mirror perpendicularly.) and rewriting the above equation, we obtain

$$R \simeq R_0 \left[1 - (4\pi\sigma/\lambda)^2 \right] \quad (4.44)$$

In the following discussion we evaluate the contribution of both the reflectance and the scattering. We measure the reflectance of surfaces of NiP in 240 nm to 2600 nm using Solid Spec-3700. We prepare finished NiP with a good surface roughness of 2 nm rms and non-finished surface with $\sigma \sim 1000$ nm.

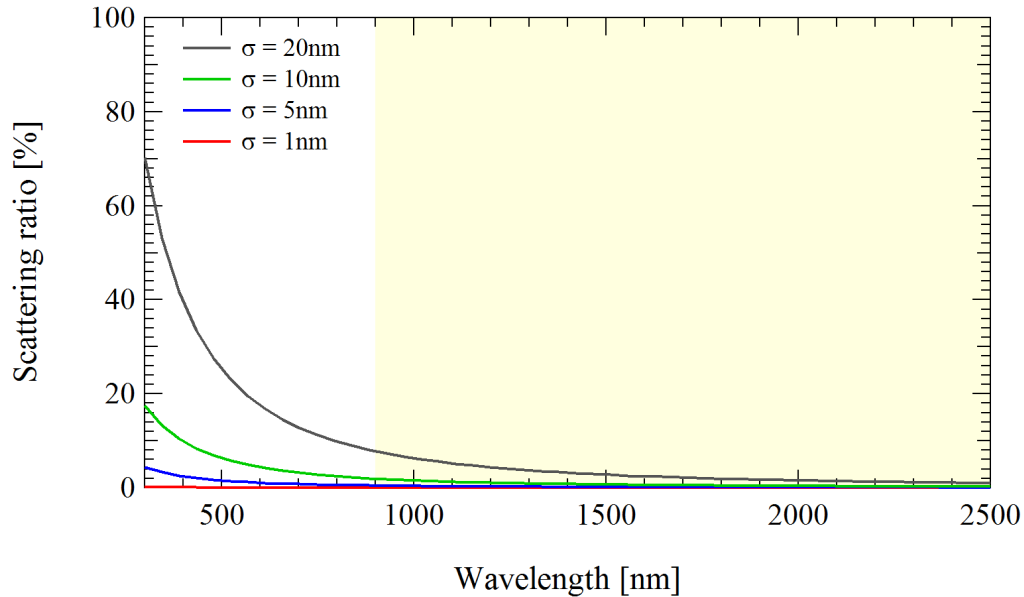


Fig. 4.16 The calculated scattering rate with the surface roughness of $\sigma = 1, 5, 10,$ and 20 nm.

Fig 4.15 shows the results. The surface with 2nm roughness measured reflectance curves have wavelength dependence with $R_0 \propto \lambda^3$. The reflectance rapidly decreases especially below $1.6 \mu\text{m}$ (*i.e.* J - and H -band) and is almost constant in the K -band. Since the surface roughness is 2 nm , the influence of scattering due to the roughness is considered to be negligible even at $\lambda = 1 \mu\text{m}$, and the wavelength dependence is considered to be the intrinsic reflectance of electroless NiP. This result suggests we have to apply a gold coating on a NiP mirror in order to achieve a high throughput of $\sim 98\%$.

Next, we calculate the Debye-Waller factor with $\sigma = 1, 5, 10,$ and 20 nm , respectively. Calculated scattering rate $S_\sigma(\lambda)$ is shown in Fig 4.16. We evaluate influence of scattering at the $\lambda = 900 \text{ nm}$ which is most sensitive to the surface roughness, and find that the influence is almost negligible when $\sigma < 5 \text{ nm}$ ($S_5(900\text{nm}) < 0.5\%$). At $\sigma = 10 \text{ nm}$, $S_{10}(900\text{nm})$ is $\sim 2\%$, and this value is also acceptable for our observations. In other words, a mirror surface should be finished with a roughness less than 10 nm .

Combining the effect of both the reflectance and the scattering, we estimate the total throughput of SWIMS-IFU which contains five mirror surfaces. Calculation is performed assuming the all mirror to be coated with thin gold film. Fig. 4.17 shows the throughputs dependence on the surface roughnesses. In the case of the surface roughness is $\sigma = 20 \text{ nm}$, the throughput drops to $\sim 60\%$, which is not a realistic value for scientific observations. We can obtain a throughput of 82% at $\sigma = 10 \text{ nm}$ and 90% at $\sigma < 5 \text{ nm}$. Based on these results

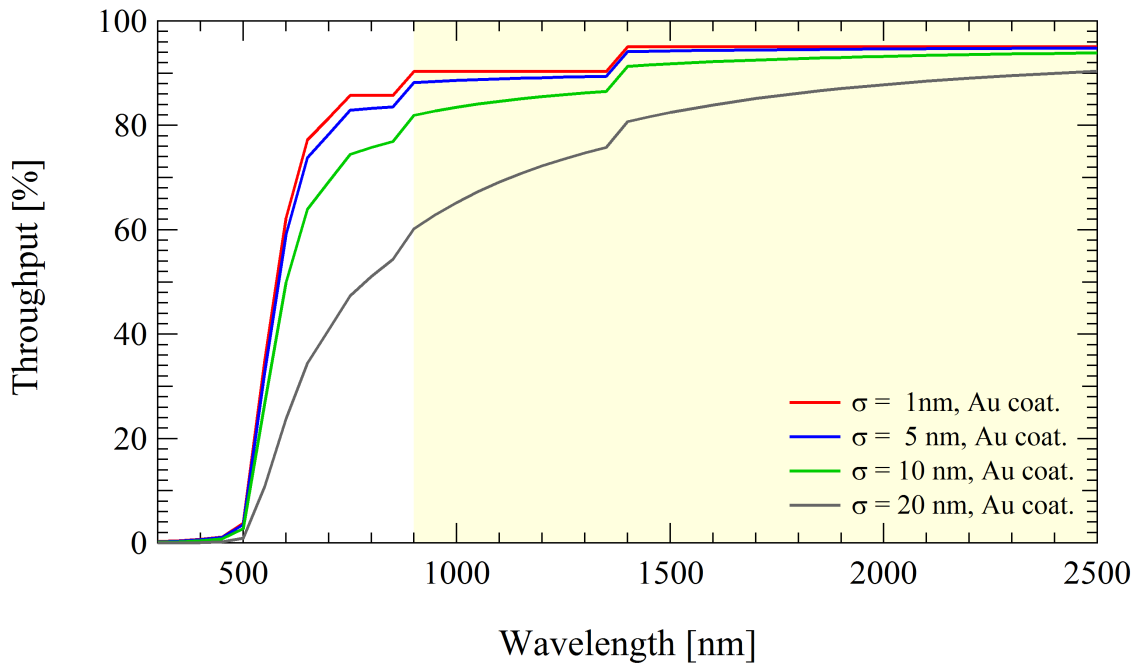


Fig. 4.17 Estimated total throughput of SWIMS-IFU. We assume there are five gold-coated NiP mirrors in the IFU.

we define the required accuracy for a surface roughness as 10 nm since the values can be sufficiently achieved using a current ultra-precision cutting machine.

Alignment error and manufacturing tolerance of the optical element will cause a displacement of the pupil in the SWIMS, resulting in loss of light intensity. Considering the error of each optical element given to Table 4.8, we estimate the influence on a throughput to $\sim 10\%$ at the maximum. As a results we conclude that the throughput of the IFU is $\sim 70\text{--}80\%$ (varying with channel) when a surface roughness of 10 nm is achieved.

4.6 Summary of Optical Design

In this chapter, we perform optical design to add an IFS mode to SWIMS spectrograph as a compact optical module. SWIMS has been originally designed as an imager and multi-object spectrograph, and all components have already been manufactured. The most important point in design is that an optical layout of SWIMS-IFU must be designed to be consistent with both the mechanical and optical systems of SWIMS without any modifications of them. This restriction requires an extremely compact optical layout that has not been achieved with existing IFUs. There is a compact IFU as before (*e.g.* FOCAS-IFU, GMOS-IFU in the optical and GNIRS in the near-infrared), however, the thickness of SWIMS-IFU in the direction

of the optical axis of the telescope is only 60 mm, and there has been no IFU design under such a size limit. It gives the most severe restrictions on our optical design, and leads to the following design difficulties. First of all, it is very unclear whether an optical layout that satisfies size restrictions can be constructed. In addition, since incident light is reflected in a small space, there is a possibility that the aberration may become large at the end channel.

In order to overcome these design difficulties, we first perform paraxial calculations to search possible optical layouts under given parameter related to the size. This formulation provides a clear perspective under a given constraints, so that we are able to identify the range of existence of paraxial solutions. Next, ray tracing is performed based on the obtained paraxial solution, and careful optimization is performed so that the aberration become minimized at about 80 optical surfaces included in the IFU. In particular optimization of the outer channels in the pupil mirror array is one of the design difficulties since the light ray from the slice mirror is reflected at a steep angle, which leads to bad slit images. We employ aspheric surfaces for the outer channel of the pupil mirror, and confirm the image quality is improved to the same degree as the center channel. Manufacturability of the pupil mirror array is also taken into consideration by adopting the minimum number of aspherical surfaces. Through careful optimization, we finally succeed in constructing an optical layout that satisfies the severe size restriction and required optical performance for seeing-limited observations. As a result, the obtained optical layout of SWIMS-IFU has become the most compact IFU.

Chapter 5

Monolithic Fabrication of a Slicing Mirror Array

5.1 Application of Ultra-Precision Cutting to IFU optics

Optical elements are the heart of astronomical instruments. Quality of an optical element such as a surface roughness or a shape error is important factor which greatly influences science data quality. Up to now, an optical surface is mainly fabricated by two different methods. One is polishing, and the other is cutting process.

Polishing has been used to make mirrors and lenses for optics since the beginning of astronomical telescopes (Jones, 1890; Li et al., 2016; Lubliner and Nelson, 1980; Martin et al., 1990). This is because the polishing can achieve an excellent surface roughness and can easily produce not only infrared but also visible wavelength optical elements. However, the polishing takes time for processing, which has become a problem that cannot be ignored for optical systems which become large in recent years. Also, for metal substrate for a metal mirror which is optimum for use under cryogenic condition, the polishing cannot achieve an enough surface roughness for use at the visible wavelength.

Cutting process has been originally used for other than optical surfaces such as structures, but with the evolution of processing machines in recent years, high-precision has been achieved. In particular, ultra-precision processing technology using diamond tools can create mirror surfaces with accuracy that can sufficiently meet requirements in the near-infrared to the optical wavelength. Ultra-precision machining creates a shape by transferring the motion trajectory of a diamond tool to a workpiece. Some examples achieve a surface roughness of < 10 nm for metal materials (Dubbeldam et al., 2012).

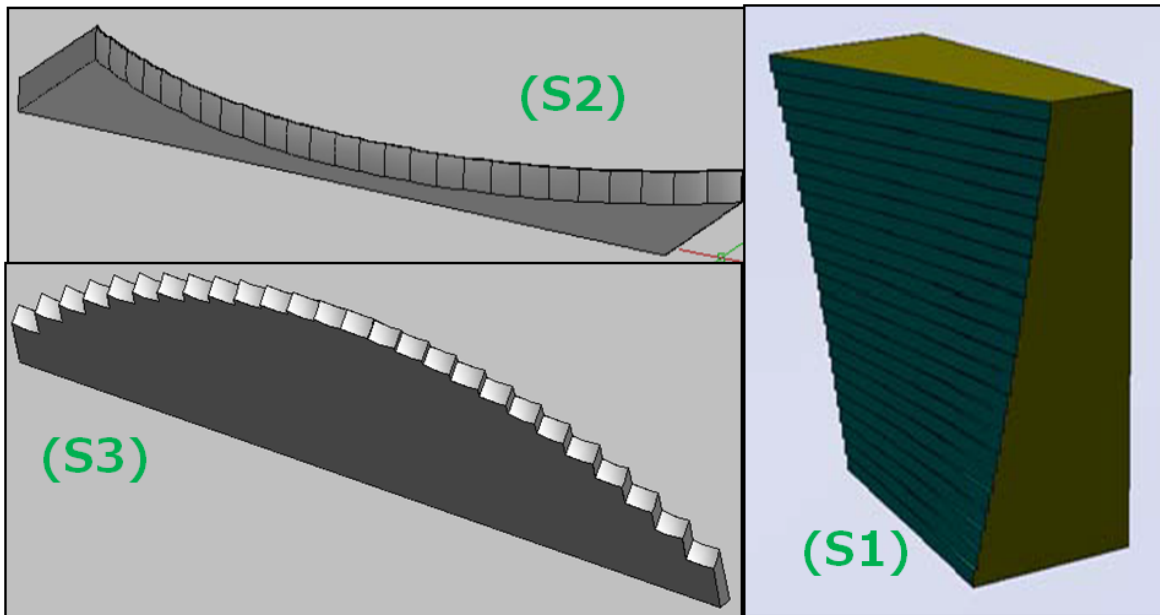


Fig. 5.1 Conceptual image of IFU optics. (S1) Slicing mirror array (S2) Pupil mirror array (S3) Slit mirror array. Each mirror array has 25 reflective surfaces.

In recent years, the ultra-precision cutting technology has become an important technique for production of optical elements of near infrared IFUs. An image slicer type IFU requires faceted mirror arrays as shown in Fig 5.1, and the ultra-precision cutting is suitable for fabricating such mirror arrays. This is because that it is easier to create a complex shape than polishing and a mirror array can be monolithically fabricated (Dubbeldam et al., 2004). Especially one of the advantages of using ultra-precision cutting technology is that it is very good at figuring metal materials thanks to hardness of diamond tools. Also, once we establish the processing method, it is easy to create many mirrors with the same shape and same quality. This will have a big influence for development of multi-object IFUs that are being studied for next-generation instruments (Dubbeldam et al., 2012). These advantages remarkably reduce the time for optical alignment and is a very important technology in optical systems with many optical surfaces like IFUs (Rolt and Robertson, 2008)

However, IFU optics have complicated shapes, and to precisely fabricate them is a challenging task (Dubbeldam et al., 2012; Kitagawa et al., 2016; Lee et al., 2006). Especially in near infrared instruments, it is typically required that shape error should be $< 0.1 \mu\text{m}$ and a surface roughness should satisfy $< 10 \text{ nm}$. It is a very challenging goal to monolithically fabricate IFU mirror arrays with such specifications even using the ultra-precision cutting process, and in this study we explore its possibility.

Processing of image slicers in recent years is made of both glass or metal as shown in Table 5.1. In the case of employing a glass materials, each thin reflecting mirror is polished

Table 5.1 Examples of recent fabrications of image slicers †

	Glass	Aluminum alloy (w/o plating)	Nickel phosphorus plating
Polishing	SPIFFI ^(a) , MUSE ^(b) FOCAS-IFU ^(c)	–	–
Cutting	–	KMOS ^(d) , FISICA ^(e) MIR-IFU for TMT ^(f)	SWIMS-IFU ^(g)

† Note that only the IFUs in which both mirror material and processing method are describe are listed in the table.

^(a) Tecza et al. (2000)

^(b) Laurent et al. (2008)

^(c) Ozaki et al. (2014)

^(d) Dubbeldam et al. (2012)

^(e) Eikenberry et al. (2004)

^(f) Sakon et al. (2016)

^(g) Kitagawa et al. (2016)

and is assembled using a high-precision jig for alignment. It is adopted as an optical image slicer which does not need to cool the optical system (Laurent et al., 2008; Ozaki et al., 2014). For the infrared image slicer, monolithic processing of raw metallic materials (*e.g.* an aluminum alloys) is commonly used (Dubbeldam et al., 2012; Eikenberry et al., 2004; Sakon et al., 2016). However, a surface roughness of raw metallic materials tends to be lower compared with a glass with polishing processing due to defects on a surface. In order to further improve the surface roughness, we adopt a nickel phosphorus plating as a mirror material.

As a first step, we conduct a proof-of-principle experiment to fabricate the slicing mirror array of the SWIMS-IFU. This is because a surface shape of slicing mirror are simple (*i.e.* plane), and it requires multi-axis simultaneous control, which can be applied to fabrications of other mirror arrays. Therefore, this is a good way to accumulate the technique of mirror array fabrication.

5.2 Specifications and Methods

We perform monolithic test fabrications of the slicing mirror array of the SWIMS-IFU. Specification of the slicing mirror is shown in Table 5.2. We prepare an A5052 substrate pre-figured to the shape of the final mirror array and coated with nickel phosphorus (NiP) plating with a thickness of 100 μm . The aperture size of the mirror array is 10 mm x 12.5 mm and twenty-five reflective surfaces with a slice width of 500 μm are aligned on it. As shown

Table 5.2 Specifications of the slicing mirror array

Mirror materials	A5052P
Coating thickness	100 μm
Tool Diameter (ϕ)	500 μm
Aperture Size	12.5 mm \times 10 mm
Mirror shape	plane
Number of reflective surface	25
Slice width (w)	500 μm
Facet angle ($\Delta\theta$) ^(a) ^(b)	0.45–1.67 deg
Maximum angular difference ($\Delta\theta_{\text{max}}$) ^(b)	13.9 deg
Roughness	Ra < 10 nm
Shape error	P–V < 0.1 μm

^(a) Angle pitch per a reflective surface.

^(b) The definition is depicted in Fig 5.2.

in Fig. 5.2, each channel (*i.e.* each reflective plane) has an angular difference ($\Delta\theta$) with each other, and its value varies from 0.45 to 1.67 degrees for each channel. The maximum angular difference ($\Delta\theta_{\text{max}}$) between Ch 25 and Ch 1 is about 14 degrees. Ch13 is set to $\theta = 0$ degree, *i.e.* parallel to the X-axis drawn in Fig. 5.2. The shape of each reflection plane is flat, and the parameters in Table 5.2 are set to almost the same as the specifications of SWIMS-IFU.

The processing procedures are shown in Fig. 5.3. First we cut the workpiece from an aluminum plate using a NC machining center. Next, using a tungsten carbide end mill tool, we create a faceted shape with an ultra-precision processing machine. In this process, the shape takes into account the thickness of NiP plating. Then, electroless NiP plating of 100 μm thickness is coated on the workpiece. Unnecessarily plated parts are cut off with the tungsten carbide end mill tool. Finally, the surface is finished using a endmill tool made of single crystal diamond. Workpiece after the process is ultrasonically cleaned with isopropyl alcohol for 30 minutes to remove burrs.

The ultra-precision processing machine used for the mirror finishing is ULG-100A (Fig. 5.4a), which can control four-axes and has freedom of translation (X, Y, Z) and work rotation (C). The motion accuracy of each axis is 10 nm and 10^{-4} degrees. We use the end mill tool made of single crystal diamond with a diameter of 500 μm , rotated at 18500 rpm.

5.3 End mill processing with Single axis Control

In order to manufacture a slicing mirror with flat surfaces by end milling, the most straightforward method is to control the diamond tool with only one axis in the X-direction. The

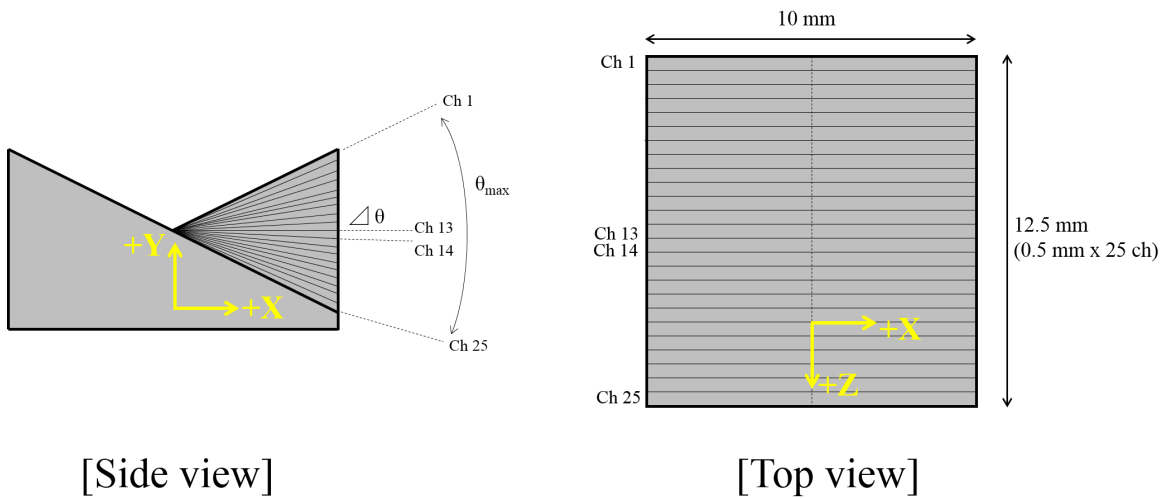


Fig. 5.2 Configuration of the slicing mirror. Each reflective surface is represented by Ch1–Ch25. The coordinates (X, Y, Z, C) correspond to those explained in Fig. 5.4a.

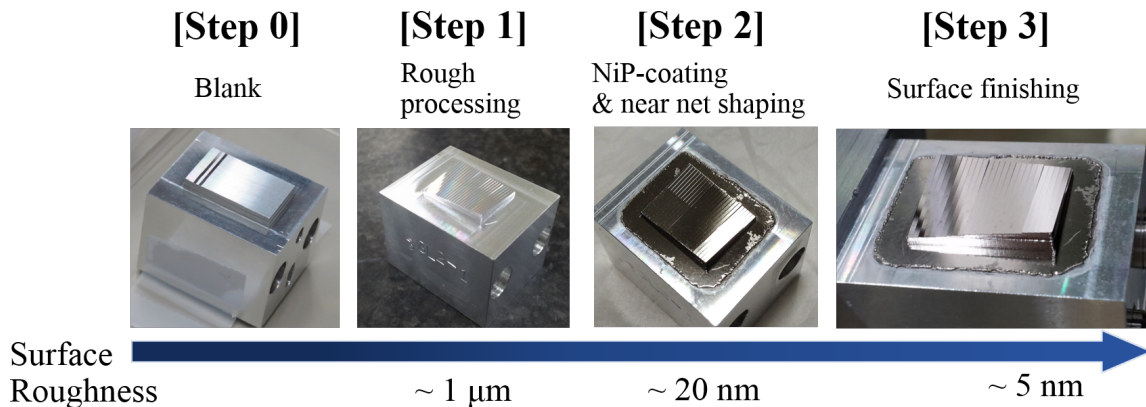
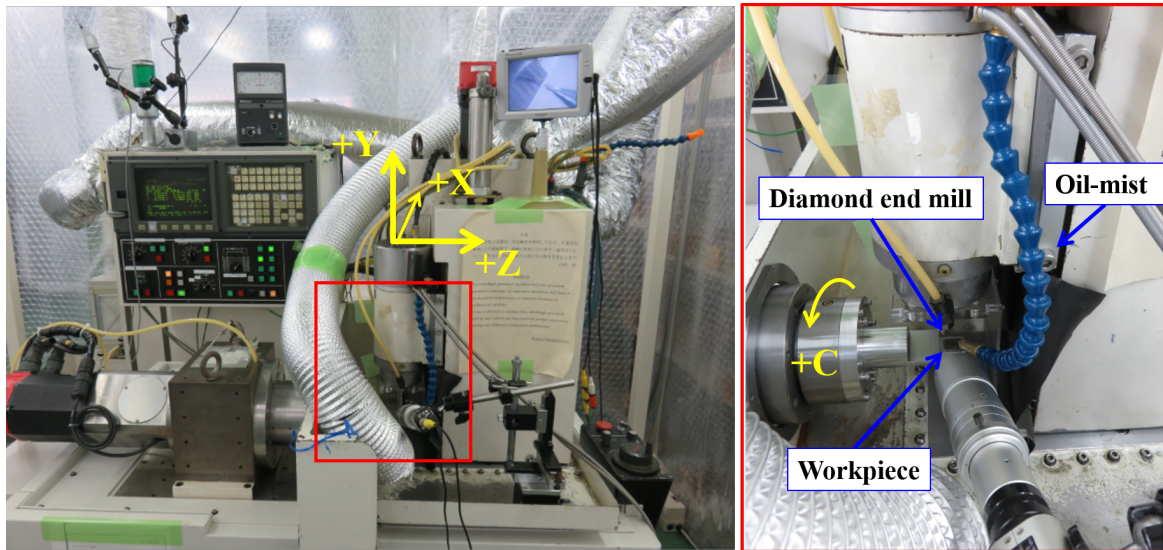
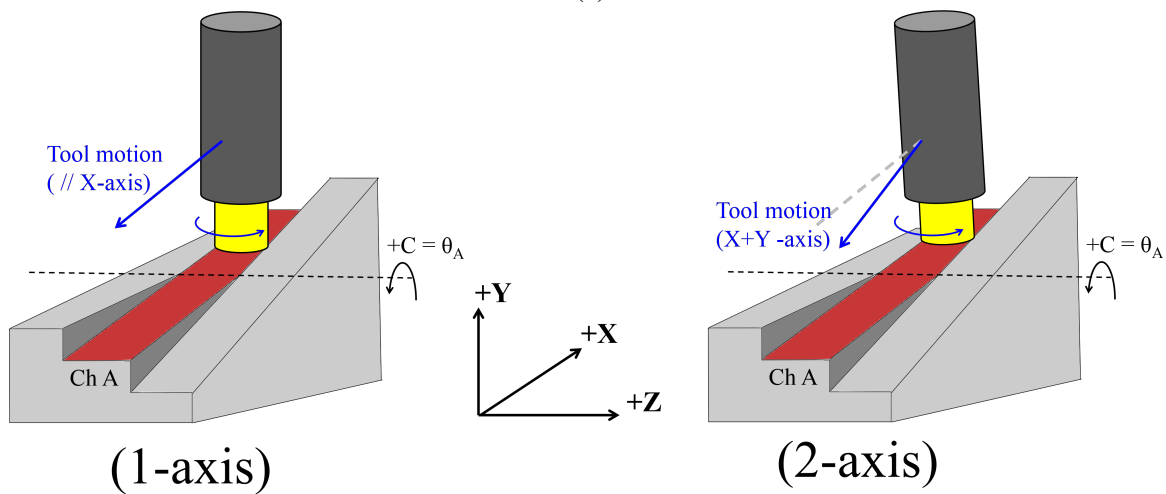


Fig. 5.3 Processing procedure of fabricating a slicing mirror. [Step 0] Prepare a blank substrate (A5052). [Step 1] Shape the blank into a mirror array using a NC machining center, and perform rough figuring using a ultra-precision cutting machine, using a cutting tool made of tungsten carbide (WC). A surface roughness after this step is a few μm . [Step 2] Coat the aluminum substrate with electroless NiP plating. Thickness of the coating is about $100\ \mu\text{m}$, which is a typical value for a ultra-precision mirror finishing. Near-net shaping is performed using a WC tool. The surface roughness becomes less than $100\ \text{nm}$ after this step. [Step 3] Finish the surface using a ultra-precision cutting machine. In order to obtain reflective surfaces a single crystal diamond tool is used. After this step, the surface roughness reaches a value of $5\text{--}10\ \text{nm}$.



(a)



(b)

Fig. 5.4 (a) Photograph of the ultra-precision cutting machine (ULG-100A), which has four degree of freedom of movement (X, Y, Z, C) indicated by yellow arrows. The right photograph is an enlarged view of the red square in the left. (b) schematic illustration of a configuration in cutting process. The diamond tool moves in the only X-axis (1-axis) or X+Y-axis (2-axis) direction, and make the red-filled area finishing.

processing concept is shown in Fig 5.4b: when we cut a certain reflecting surface (Ch A), the C-axis is first rotated so that Ch A is set parallel to the X-axis. Then, by moving the diamond end mill in the X-direction while rotating, the surface of Ch A becomes a plane parallel to the X-axis (Fig. 5.4b).

We perform a fabrication experiment of a slicing mirror which has a specifications shown in Table 5.2 As shown in Fig. 5.5 a workpiece with aluminum alloy plated with nickel phosphorus (NiP) is mirror-finished. We evaluate the surface roughness and shape of the surface-finished workpiece. For the measurement, a non-contact white interferometer ZygoNewView7200 with 10× objective lens is used. The field of view of the measurement area is $702 \mu\text{m} \times 526 \mu\text{m}$ and the central region of Ch 13 is measured.

The results are shown in Fig. 5.7(a). The surface roughness is 7.6 nm, which meets the required specification of 10 nm. The cross-sectional shape in the moving direction of the tool is about 80 nm P-V. According to the top panels of Fig. 5.7, however, a deviation from flat shape occurs in the entire field of view. As shown in the middle panel, a parabolic shape with sag of ~ 220 nm can be seen in a direction perpendicular to the processing direction. The radius of curvature (R) corresponding to the sag is $R = w^2 / (2 \times \text{sag}) \simeq 140$ mm. This power of the slicing mirror causes deviation of the pupil position and defocusing of the exit slit, which will significantly reduce the optical performance of the IFU. We also confirm that the parabolic shape occurs even if the feed rate of the tool is changed. These results suggest that a global parabolic shape appears in the case of single axis control of the tool, and a shape satisfying the specification cannot be obtained.

5.4 Correction of the Parabolic Shape Error

The most likely reason for the appearance of the parabolic shape is that the rotation axis of the diamond tool has an angular offset (α) with respect to the Y-axis as shown in Fig. 5.6(a). In this case, when moving the tool in the X-axis direction, a parabolic shape appears in the cross section, which is similar to the appearance of a parabola on the oblique cut surface of the cylinder. the angular error is estimated to be $\sin^{-1}[\text{sag}/(\phi/2)] \simeq 0.058$ degrees. If the cause of the sag is the tool misalignment, the parabolic shape should disappear when the tool moves obliquely at the angle of α using X- and Y-axis simultaneously.

We conduct a fabrication experiment to verify the above assumption. Another test piece with NiP plating is prepared, and one groove processing is performed while changing the angle of the tool. Feed speed and tool rotation speed are the same as Section 5.2.1. Fig. 5.6 shows the relationship between tool angle (ΔC) and sag depth. Clearly the sag depth varies depending on the tool angle, and it turns out that the sag converges at $\Delta C < 0$. The angle, at

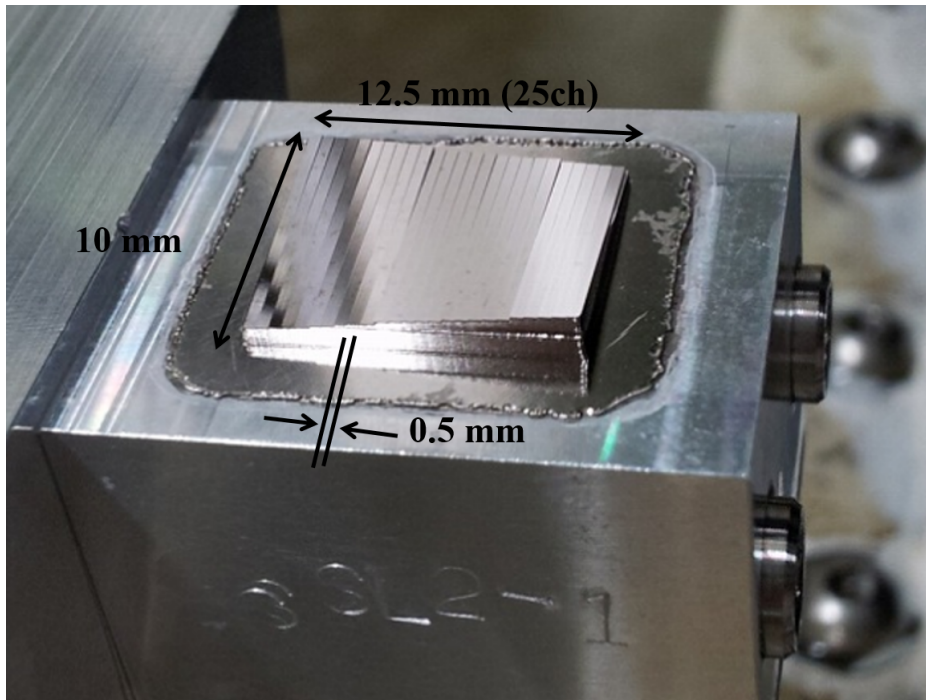


Fig. 5.5 A photograph of finished surface of a test slicing mirror array.

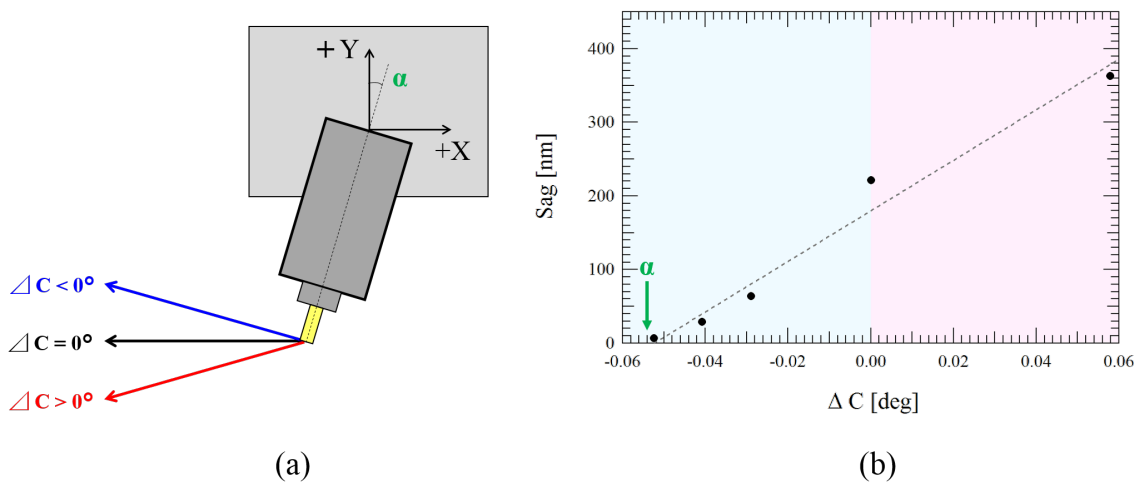


Fig. 5.6 (a) Schematic illustration of the relationship between tool motion and each axis. The definition of the sign of each axis is same as Fig. 5.4(b). Black arrow indicates movement of the diamond tool when controlled with only the X-axis. Blue and red arrows mean the tool motion when both the X-axis and the Y-axis are controlled at the same time. An angle of α represents the misalignment angle of the diamond tool with respect to the Y-axis. (b) Shape error dependence on C-axis angle. Each data point is obtained from the measurement, and the black dashed line represents the best fitting of them. The angle α can be obtained as the limit of sag $\rightarrow 0$ nm.

which $\text{sag} \rightarrow 0$ nm, corresponds to the angular error of the tool, and we obtain the value from the linear fitting of the measurement point. The estimated value is 0.052 degrees, which is in good agreement with the value of 0.058 degrees obtained from simple analysis. This result confirms that the assumption that the sag is generated by tool misalignment.

In order to obtain a plane with flat shape, correction of this angular offset is required. However, it is difficult to re-align the processing machine on the order of 0.001 degrees. Here, we show a method to correct the misalignment of the rotation axis of the tool by performing simultaneous control of the X- and Y-axes. In this method, by reflecting the estimated angle error in the toolpath, it is possible to obtain a planar shape by moving the tool parallel to the direction of the angle α .

We recalculate the tool path using $\Delta C = 0.052$ degrees and perform the fabrication of slicing mirror again under the same conditions as Section 5.3. The measurement result is shown in Fig. 5.7(b). The bottom panel shows that a global parabolic shape does not appear in the cross sectional shape perpendicular to the processing direction, and cutter marks can be clearly seen in the top panel which indicate a flat surface can be obtained. This results shows that the shape error can be corrected effectively by biaxial simultaneous control.

However, in the cross sectional shape parallel to the processing direction (the middle panel), a sawtooth-like undulation shape newly appears which is not seen in the case of the single axis control (Fig. 5.7(a)). This undulation shape has an amplitude of 160 nm and a period of 300 μm , which may cause diffraction and reduce optical performance. This is because surface accuracy generally tends to deteriorate when controlling multi-axes simultaneously, and a surface roughness satisfying the specification cannot be obtained unless appropriate cutting conditions. The result suggests that re-optimization of the cutting conditions is required when biaxial control is applied.

5.5 Optimization of Cutting Condition

One of the possible cause for the undulation shape is the vibration of the tool excited as the chips cling to the tool during processing. However, such a phenomenon is not observed with a microscopic camera, so this is not the cause of the undulation.

We investigate optimum cutting conditions experimentally by examining feed rate dependency of undulation shape. We find that the pitch of the undulation depends on the feed rate and the tendency that the pitch becomes longer as the feed rate becomes faster. Since the surface roughness tends to deteriorate as the feed rate increases, we determine that the optimum feed rate is 50 mm/min, and finally perform the zero-cut (*i.e.* cutting depth is 0 nm) to make the mirror surface finish. The final cutting condition is summarized in Table.5.3.

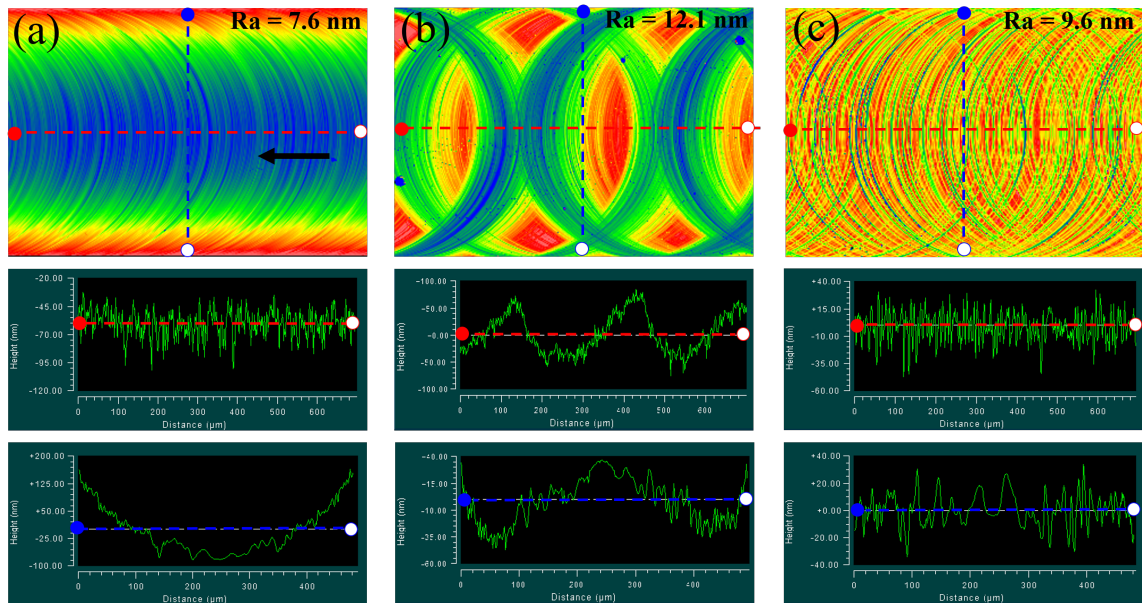


Fig. 5.7 Surface roughness after end milling. (a), (b), and (c) correspond to condition A, B, and C described in Table 5.3, respectively. Top panels represents surface profile for each conditions. Middle and bottom panels show the sectional shape of the region drawn with blue and red dashed lines in the top panel, respectively. Black arrow in the upper left panel indicates processing directions.

The result under optimization (*i.e.* biaxial control with optimized cutting condition) is shown in Fig. 5.7 (c). As show in the top panel, both the parabolic shape and the undulation shape are successfully removed. This is also seen in the mid panel and the bottom panel of Fig. 5.7 (c), and < 80 nm P-V is obtained in both the parallel and perpendicular direction to the moving direction of the tool. These values satisfy the specifications for shape error of < 100 nm. The surface roughness is 9.6 nm, and meets the specification of 10 nm. Also, we perform shape measurements as shown in Fig.5.8, and measured angles achieve an accuracy of 0.002 degrees satisfying the tolerance (Table 4.8). All the measurement results are summarized in Table 5.3.

5.6 Conclusion of the Fabrication

We conduct a proof-of-principle experiment to verify whether monolithic fabrications of a slicing mirror array is possible by end milling process of a NiP coated aluminum alloy. We optimize the processing conditions carefully by finding out the cause of various shape error based on preliminary experiments. The findings obtained through this experiment are as follows.

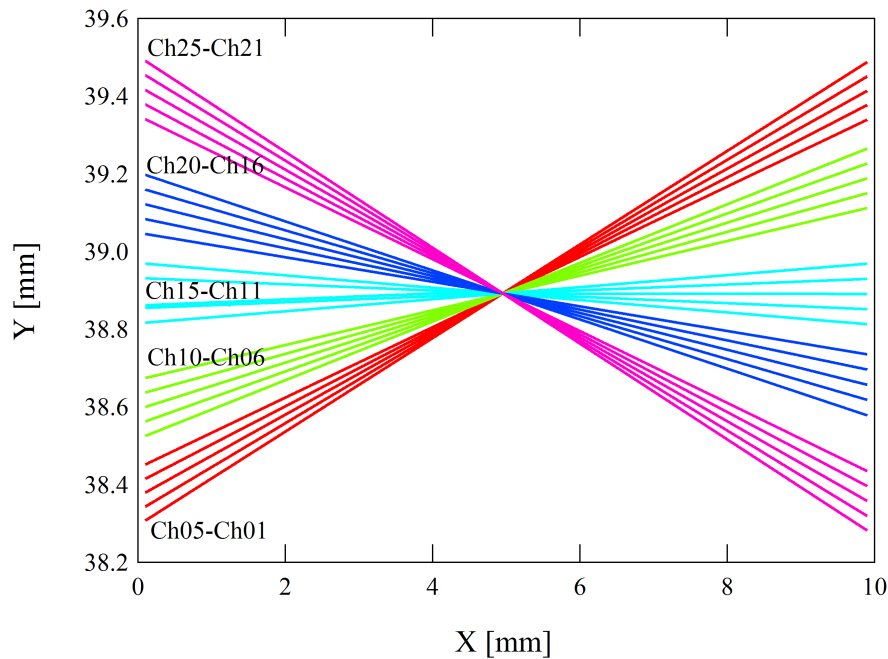


Fig. 5.8 Angle measurements of each reflective plane after finishing with the condition C. We measure the center of each reflective plane with one pass and perform linear fitting of the obtained shape to calculate the angle. The reflective planes of the slicing mirror array can be divided into five discrete groups, which vary by approximately 0.4 degrees within each group.

Table 5.3 Summary of cutting conditions and measurement results

	Condition A Single axis control	Condition B Two axis control	Condition C Two-axis + optimization
Tool motion	X-Axis ($\Delta C = 0$ deg)	X + Y-Axis ($\Delta C = 0.052$ deg)	X + Y-Axis ($\Delta C = 0.052$ deg)
Tool Rotation speed (n)		18500 rpm	
Feed rate [mm/min]	5	5	50
Cut of Depth [μm]	3	3	3 and zero-cut
Roughness (Ra) [nm]	7.6	12.1	9.6
Shape error (P-V) [nm] ^a	69.5	159.4	78.9
Shape error (P-V) [nm] ^b	221.8	83.7	62.5
Angle error (r.m.s.) [deg]	–	–	0.002

^(a) Direction depicted with red dashed line in Fig. 5.7.

^(b) Direction depicted with blue dashed line in Fig. 5.7.

- We find that the paraboloid shape appears in end mill processing with only one axis control, and experimentally identify that it is caused by tool misalignment. Furthermore, we show that amount of the misalignment can be estimated experimentally on the order of 0.001 degrees and that the parabolic shape can be corrected by biaxial control using the estimated angle.
- Experimental results of biaxial control suggest that it is necessary to carefully optimize processing conditions. Otherwise, shape errors of an order of 100 nm P-V will occur. By investigating the feed rate dependence of the shape, we find that the optimum feed rate is 50 mm/min for the best surface finishing condition. We finally achieve the shape error of ~ 80 nm and roughness of ~ 10 nm which satisfy our specification.
- This study is the first demonstration of monolithic fabrication of slicing mirror array using NiP coated aluminum. In our approach, we show that it can be manufactured with a roughness of less than 10 nm and a shape error less than 100 nm P-V by end milling.

Our method can easily be applied to correct arbitrary tool misalignment of the order of 0.001 degrees, which is difficult to correct by re-alignment of equipment. In addition, since NiP coating is compatible with diamond cutting and can also be polished, there is a possibility that the roughness can be further improved as compared with the mirror made from the conventional aluminum alloy. Further research is required for polishing processing of optical elements having complicated shapes such as slice mirror arrays.

Chapter 6

Search for Advanced Infrared Mirror Materials

6.1 Study on Diamond Cutting Performance of Metallic Alloys

6.1.1 Mirror Materials for Infrared Optics

In astronomical infrared optics, the importance of metallic mirrors is increasing year by year. This is because in infrared instruments, whose optical system should be kept under cryogenic condition, the best way to facilitate thermal design is to fabricate all support structures and mirrors from a same material. Also, the instruments for extremely large telescope such as TMT, the optical system become large. The enlargement of an optical element causes a serious problem in terms of availability of materials, fabrication and cost. Then, we can construct a reflecting optical system at relatively low cost by introducing metallic mirror mirrors fabricated by ultra-high precision cutting. Also, it is possible to increase the degree of freedom of the optical system and to make the entire layout compact by introducing non-spherical surfaces, which is easy to fabricate by the ultra-precision cutting.

Various materials such as glass, ceramics, and metals have been used as mirror base materials (Jedamzik et al., 2016, 2014; Kurosawa et al., 1990; Petrovsky et al., 1994). Fig. 6.1 compares a specific stiffness and a thermal stability of typical mirror materials. A specific stiffness is defined as a Young's modulus divided by a density of materials. A quantities obtained by dividing CTE by a thermal conductivity represents thermal stability of a mirror shape with respect to a heat input. SiC shows good specific stiffness and thermal stability among them, and is widely used as a mirror material of a space telescope (Kaneda et al.,

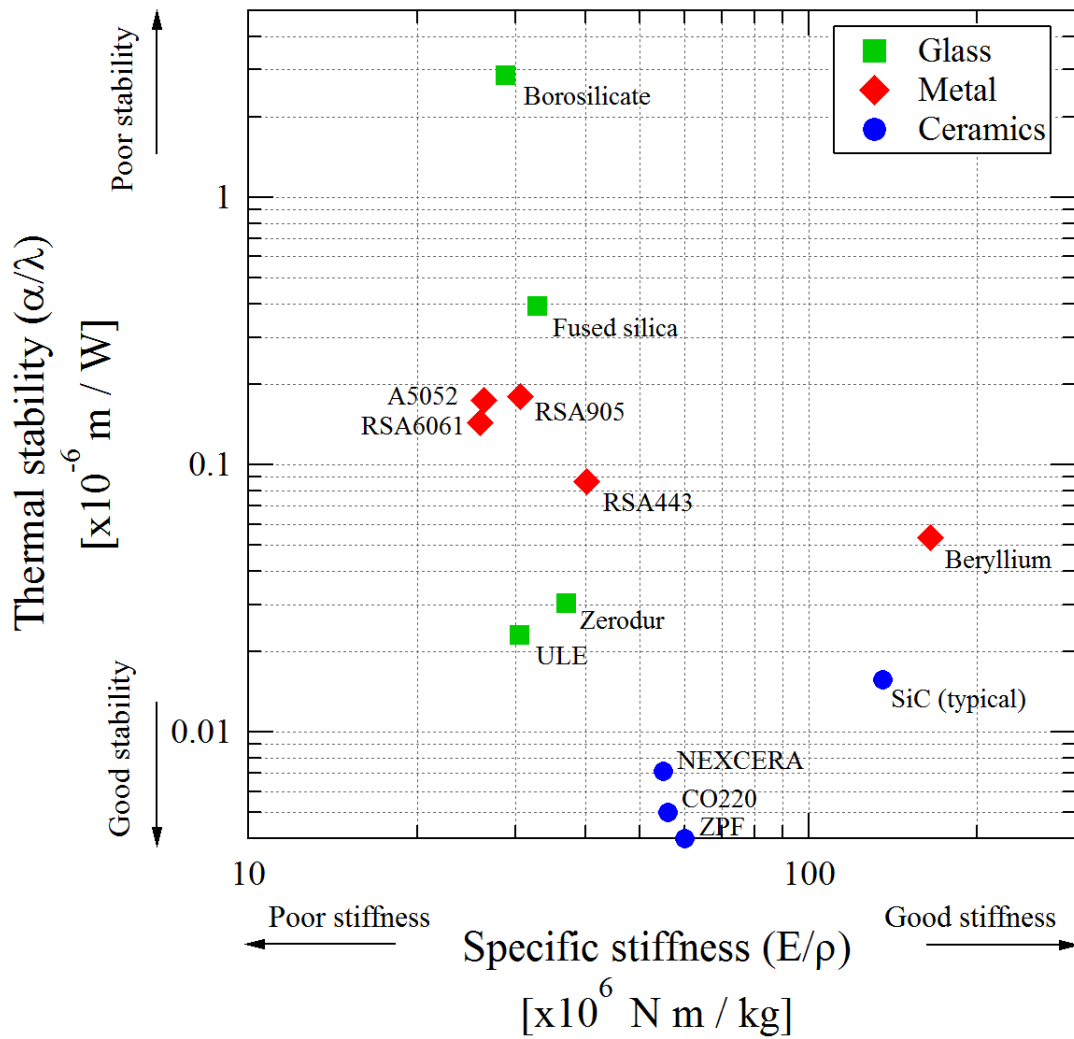


Fig. 6.1 Comparison of physical properties of mirror materials. A specific stiffness is defined as a Young's modulus (E) divided by a density (ρ) of a material, and a thermal stability is defined as a coefficient of thermal expansion (α) divided by a thermal conductivity (λ). Each point is calculated from the table in Tsuno et al. (2005) and also from the data sheets on the company's websites: KYOCERA (<http://www.kyocera.co.jp>), KROSAKI HARIMA (<http://krosaki-fc.com>), NTK CERATECH (<http://www.ceratech.co.jp>), and RSP TECHNOLOGY (<http://www.rsp-technology.com>).

2003; Pilbratt et al., 2010). Among the metallic alloys, RSA443 is the closest to SiC and significantly performs better than other glass materials. SiC has disadvantages such as high cost, fragility, and complicated processes for mirror finishing. In case of metallic alloys, it is resistant to extrinsic impact and mirror finishing can be achieved easily using cutting and polishing process. Since RSA443 has especially good thermal stability with keeping the advantages of good stiffness, it is optimal for precise optical element.

These metallic alloys, however, still have few systematic evaluation of diamond cutting performance from the viewpoint of use as an optical element (Saito, 1978; Sugano et al., 1987). Especially the evaluation of adding special aluminum materials which become available in recent years (*i.e.* for commercial use) is a new attempt (ter Horst et al., 2012). Therefore, it is an important database in the selection of the mirror material of ultra-large infrared instruments of extremely large telescopes such as TMT in the future. In this section, we performed the evaluation to find an optimum material for the metal mirrors, focusing on special aluminum alloys that appeared recently.

6.1.2 Diamond Turning Experiments

In order to evaluate which aluminum alloy is suitable for the cutting process, we carry out an experiment to find out what kind of surface defect is present and whether the surface roughness changes depending on the material. Our final goal is to find which aluminum alloy is most suitable for the base material of the IFU mirror.

The outline of the experiment is as follows. First we prepare various aluminum alloys. Each aluminum alloy is cut out into the same shape which has a mirror in a planar shape, and the planar part is finished with ultra-precision cutting with a diamond tool. Finally the surface roughness of the mirror is measured for each aluminum material. This experiment is to evaluate which aluminum is suitable for cutting.

We chose A2021, A5052, A6061, and A7075 from conventional aluminum alloy materials and RSA443, RSA6061 and RSA905 from special aluminum alloy as shown in Fig. 6.2. In addition for comparison, C1020 (oxygen-free copper) and NiP over RSA443 are chosen. These special aluminum alloy has become available in recent years. CTE of RSA443 matches to those of NiP plating by adjusting Si content ($\sim 40\%$). RSA6061 has the same composition as A6061, but grain boundary minimized by quenching in the manufacturing process, as a result, the surface roughness after cutting is improved. RSA905 can be polished directly like a glass materials. The conventional aluminum alloys; A2024, A5052, A6061, and A7075, are readily available, low cost, and it is used for various purposes.

We cut off each workpiece with a 10 mm \times 10 mm size plane aperture using an NC milling machine. After that, diamond turning is carried out in two steps using a 4-axis ultra-

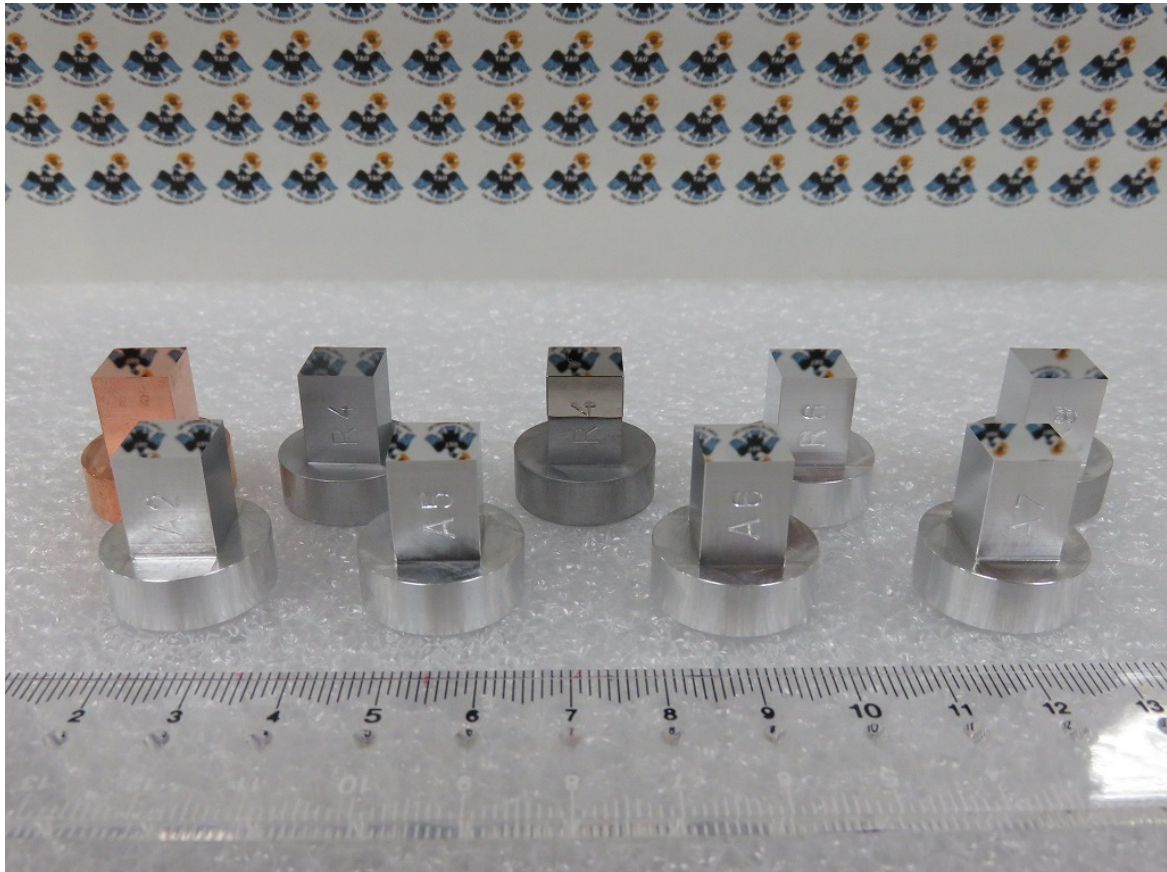


Fig. 6.2 Photograph of surface-finished mirrors made of various metallic alloys. Shown are A2024, A5052, A6061, and A7075 (conventional aluminum alloys) from the left in front row, and C1020, RSA443, NiP on RSA443, RSA6061, and RSA905 (oxygen free copper and optimized aluminum alloys) from the left in rear row. The aperture of each mirror has a planar shape and the size is 10 mm \times 10 mm.

Table 6.1 Processing conditions of diamond turning

Step	Rough processing	Surface finishing
Work rotation speed (n)	500 rpm	
Feed rate (F)	20 mm/min	5 mm/min
Feed pitch ($d = F/n$)	0.04 mm/rev	0.01 mm/rev
Cut of depth (D)	2 μm	1 μm
Number of Cuts (L)	6	2
Total cut of depth ($D' = DL$)	12 μm	2 μm
Tool radius (R_t)	1.6 mm	
Theoretical roughness (R_z)	125 nm	7.8 nm

precision cutting machine for mirror finishing. The processing conditions are determined so that the theoretical maximum height R_z is less than 10 nm, and shown in Table 6.1. After machining, the mirrors are ultrasonically cleaned with IPA (isopropyl alcohol) for 30 minutes in order to remove burrs and then dried under room condition. The cutting edge of the diamond tool is checked with a microscope, and it is confirmed that chippage and the relevant events are not occurring.

6.1.3 Results

In order to evaluate how the cutting performance varies for each material, we measured surface roughness and shape of each workpiece. Before the measurement, the workpiece is left at ambient temperature (291 K) in a thermostatic room for about 20 hours to avoid the influence of shape deformation due to temperature fluctuation.

The surface roughness is measured by Zygo NewView7200 which is a non-contact white light interferometer. The magnification of the objective lens is $10\times$ which leads to camera resolution of 1.1 μm . Surface roughness (R_a) is calculated by applying a bandpass filter to remove global waviness shape and spike-like noise. Fig 6.3 (a) shows the arrangement of measurement points. In order to evaluate fluctuations in roughness, five regions with size of $702 \mu\text{m} \times 526 \mu\text{m}$ are measured and average is and a standard deviation are calculated. The applied band-pass filter has a high-pass cutoff wavelength of 3.3 μm and a low-pass cutoff wavelength of 131.55 μm , which are three times the camera resolution and 1/4 of the width of the field of view, respectively.

Fig 6.4(a) is intensity maps, where conventional aluminum alloys such as A5052 show irregularities and scaly structures due to grain boundaries on their surfaces, while oxygen-free copper (C1020) does not show any large defects, *i.e.*, a uniform surface structure is obtained. For RSA443, the grain boundary of Si occupies most of the surface. RSA6061 seems to have

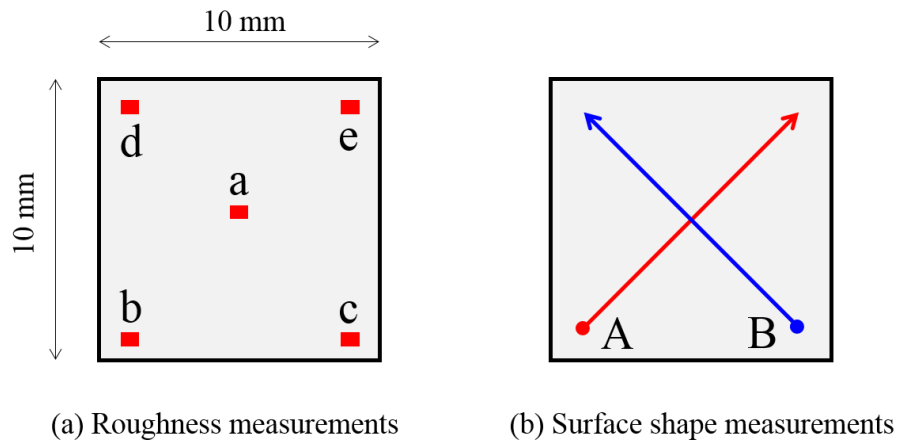


Fig. 6.3 Configuration of surface measurements. (a) Roughness is measured at five region (a–e) with size of $702 \mu\text{m} \times 526 \mu\text{m}$. (b) Surface shape is measured by scanning diagonally (path-A and -B) with length of 10 mm.

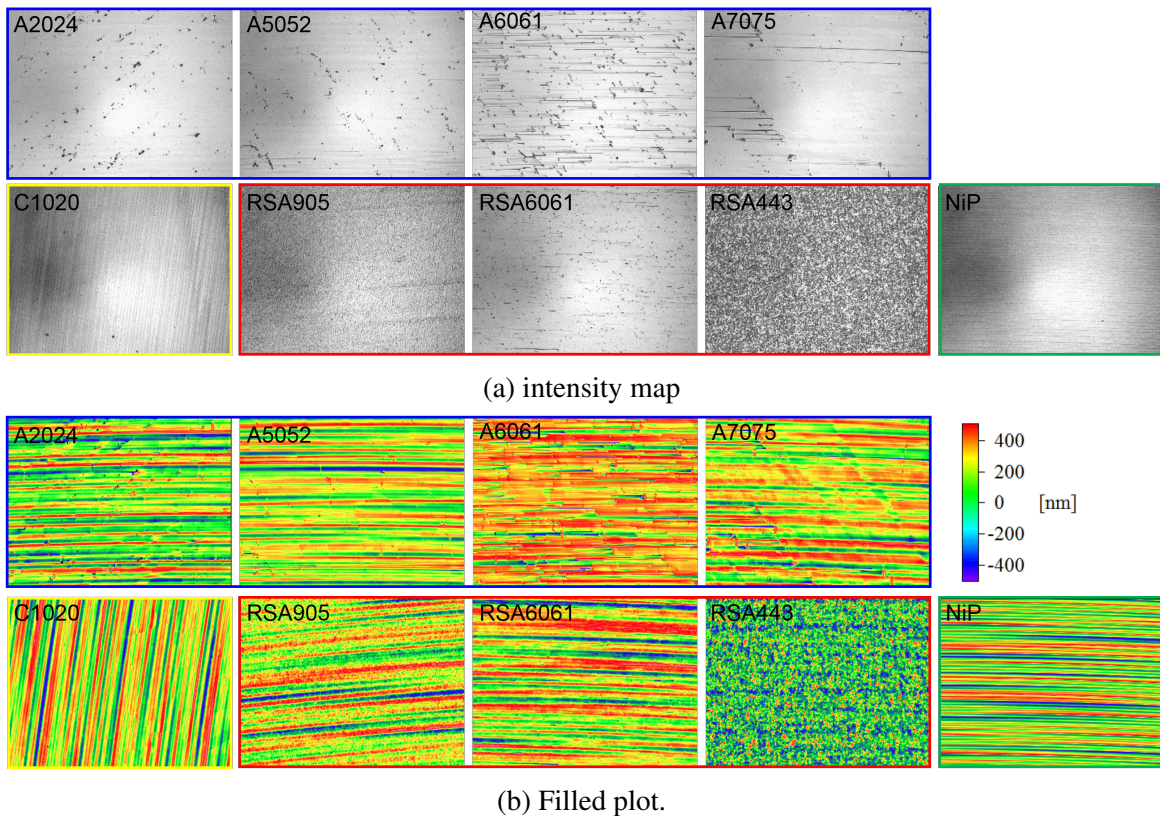


Fig. 6.4 Surface profile at the region “a” of each material with field-of-view of $702 \mu\text{m} \times 526 \mu\text{m}$ (a) Intensity maps which are useful for distinguishing fine grains (e.g. black dot-like feature) on the surface (b) Filled plots which clearly show depth and direction of cutting marks. Each field of view is same as that of (a).

a grain boundary smaller than that of A6061 which has same compounds but is manufactured by different methods. A relatively clean surface is also obtained for RSA905. There is also a feature looks like “shooting stars” which may be cutting marks by the diamond tool in Fig 6.4(a). This is clearly can be seen in filled plots of Fig 6.4(b). The differences in depth and width of the cutting marks can be found between conventional aluminum and the others. This is because the conventional aluminum alloy tends to contain large grains which affect surface profile directly, in other words, cutting performance becomes worse.

Distribution of Ra , the average surface roughness, for each material is plotted in Fig 6.5(a). Every material except RSA443 has roughness of less than 10 nm, which is sufficient for infrared optics. C1020, RSA6061, and NiP especially show good specular surface with $Ra < 5\text{nm}$.

In order to evaluate appearance of the cutting marks for each material, distributions of P-V values are shown in Fig 6.5 (b). The P-V values should reflect how fine structures such as scratches, pores and so on appear on the surface. It can be seen that even if the averaged Ra is similar, the distribution of P-V changes greatly, depending on the material. For example, in A2021, P-V has large values of 1400–2000 nm, although the averaged Ra shows small value of $\sim 5\text{ nm}$. This result indicates that there are very large scratches on the surface of A2021. On the other hand, RSA443 with Ra of $\sim 15\text{ nm}$, shows small fluctuations of the P-V values, which means the surface of RSA443 does not suffer from cutting marks. NiP and C1020 show excellent surface roughness in regard to both Ra and $P - V$ value, suggesting that they are good mirror materials.

We next carry out surface shape measurement with Mitaka PFU-3 (magnification: $100\times$) and flatness is evaluated. Measurement points are acquired in the range of 10 mm in the diagonal direction of the mirror with step of $5\ \mu\text{m}$ as shown in Fig 6.3(b),. We fitted the obtained shape data with a 20th order function, and a P-V value is calculated from the best fit function. Fig. 6.6 shows the results. Flatness of $P-V < 100\text{ nm}$ is achieved in all materials, which satisfies our specifications, except for RSA443. This is because a large number of Si grain boundaries are precipitated on the surface due to high concentration Si (see also Fig. 6.4), and makes the surface bumpy. After applying simple moving average to the data with 10 points ($= 50\ \mu\text{m}$) binning, the resultant curve falls within the above range.

The result of shape error, the shape accuracy is not affected greatly by intrinsic properties of materials, but rather determined by a processing condition (environmental temperature, cutting edge condition of the tool, and translational degree of the machine). In other words, the processing environment is stable in this experiments.

These results are summarized in Table 6.2. They suggest that NiP, C1020, and RSA6061 have excellent diamond cutting performance and high potential as a mirror material.

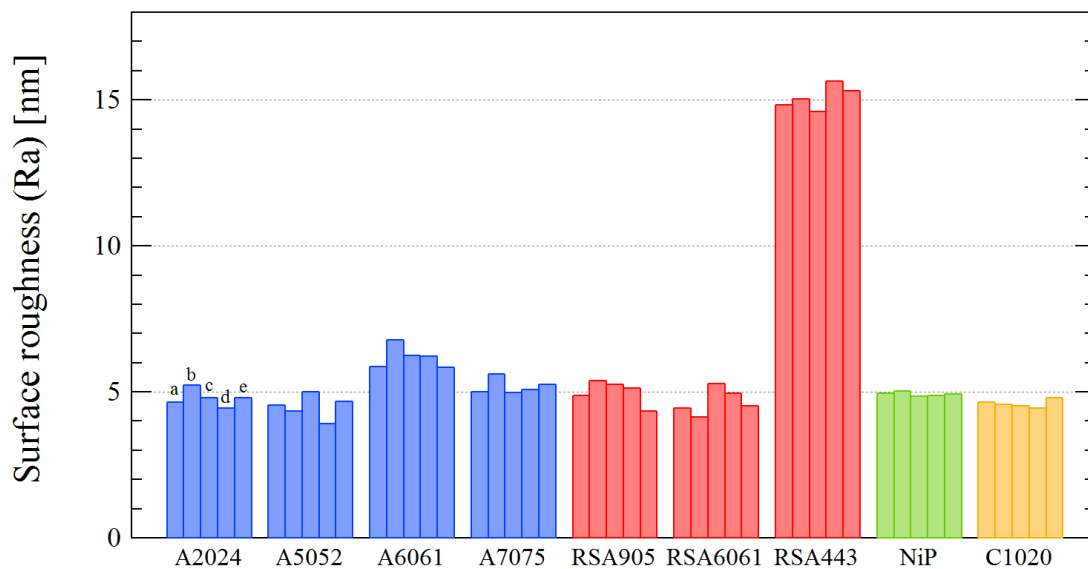
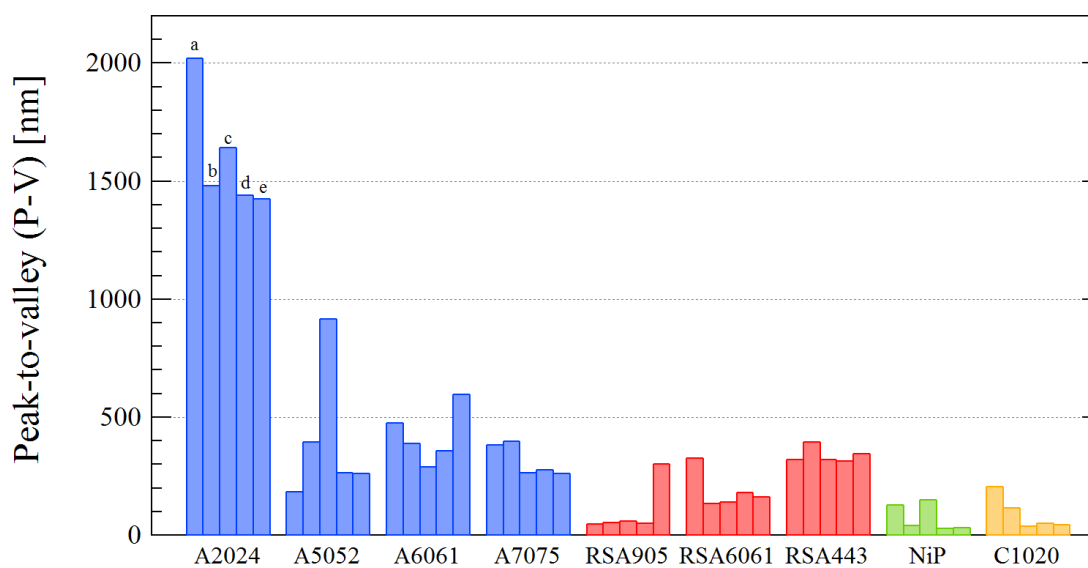
(a) Distribution of Ra values(b) Distribution of $P - V$ values

Fig. 6.5 Surface roughness measurements of surface finished mirrors. “a–c” in the figure indicate the measured regions depicted in Fig. 6.3(a).

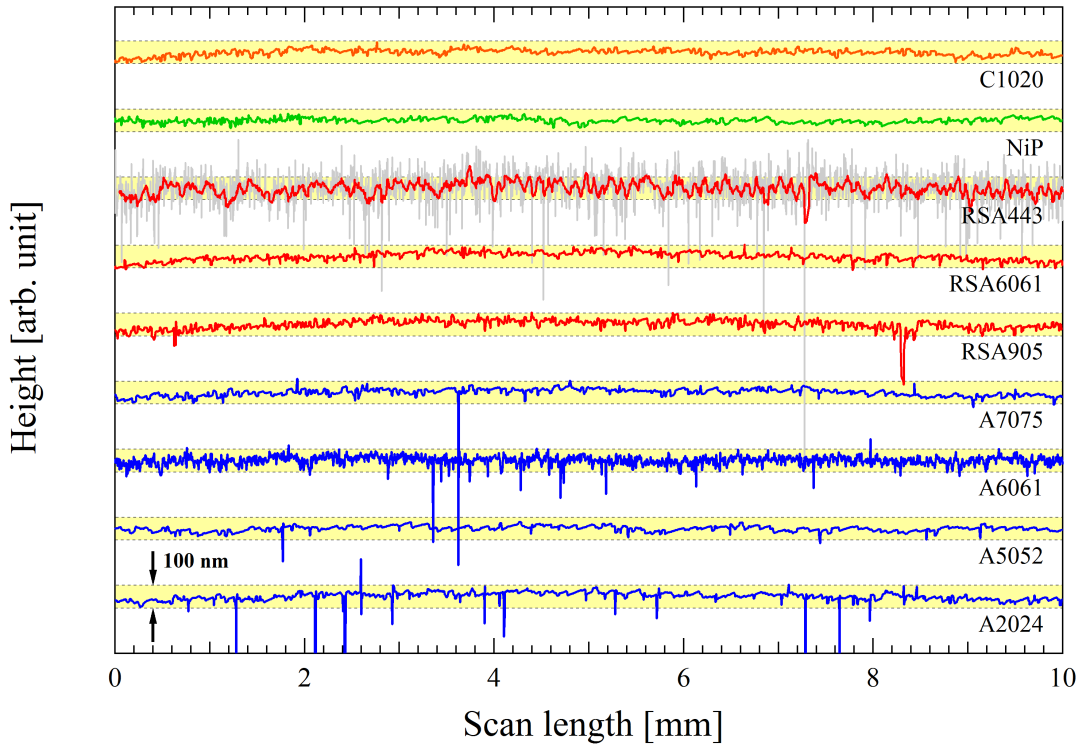


Fig. 6.6 Shape of surface finished mirrors. Plotted curve corresponds to path-A in Fig. 6.3b. The vertical axis gives an offset to improve visibility. Each yellow-filled areas indicates the range of P-V 100 nm corresponding to our requirements. The gray curve for RSA443 represents raw data, and the red curve drawn on it is obtained from simple moving average processing.

6.2 Interferometric Measurements at Cryogenic Condition

6.2.1 Bimetallic Bending Effect

NiP coated aluminum substrate has several advantages in improving optical performance (Hibbard, 1997). NiP plating has superior compatibility with ultra-precision cutting, and very good surface roughness ($\lesssim 1$ nm r.m.s.) can be achieved by diamond processing (Taylor et al., 1986). Also, by applying NiP plating, polishing becomes possible and the shape can be corrected for minute regions. It is also possible to erase cutting marks by polishing (Beaucamp et al., 2008). This is an important key technology to extend metal mirrors made with ultra-precision cutting technology to the visible wavelength range.

On the other hand, at the infrared wavelengths, it is necessary to place the entire optical system under cryogenic conditions in order to suppress thermal radiation. If the CTE of

Table 6.2 Summary of surface roughness and shape error

Materilas	Surface roughness	Shape error
A2024	4.8 ± 0.3 nm	45.5 nm
A5052	4.5 ± 0.4 nm	25.2 nm
A6061	6.2 ± 0.4 nm	29.5 nm
A7075	5.2 ± 0.3 nm	52.9 nm
RSA443	15.1 ± 0.4 nm	70.3 nm
RSA6061	4.7 ± 0.4 nm	76.5 nm
RSA905	5.0 ± 0.4 nm	50.6 nm
NiP ^a	5.0 ± 0.1 nm	21.8 nm
C1020	4.6 ± 0.1 nm	43.9 nm

^a Base matelial of NiP coating is A5052. The thickness of coating is 100 μ m

substrate and NiP plating are different, the magnitude of thermal shrinkage differs between them may cause distortion in the shape under low temperature. Since such a bimetallic bending may significantly reduce the performance of the optical system, it is important to quantitatively evaluate it by the experiment. There are still few research on shape evaluation of metal mirrors with coating under cryogenic temperature environment (DeWitt et al., 2008; Kinast et al., 2014; Robichaud et al., 1998).

In this section, we carry out mirror shape measurement at low temperature, and evaluate the effect of bimetal bending.

6.2.2 Experimental Setup

The measurement configuration is shown in Fig 6.7. The laser interferometer ZygoGPI is used for shape measurement in combination with compact low temperature dewar with an optical window to cool a sample to liquid nitrogen temperature.

As shown in Table. 6.3, A5052, RSA443 and RSA6061 are chosen for the aluminum substrate. In order to investigate the thickness dependence of bimetal effect, test pieces with various plating thickness are prepared. Each workpiece is finished with diamond turning with the same condition as described in Table 6.1 The mirror shape is set to a concave surface with a radius of curvature of 70 mm, same as that of one channel of the pupil mirror array, to estimate its shape distortion under cryogenic temperature.

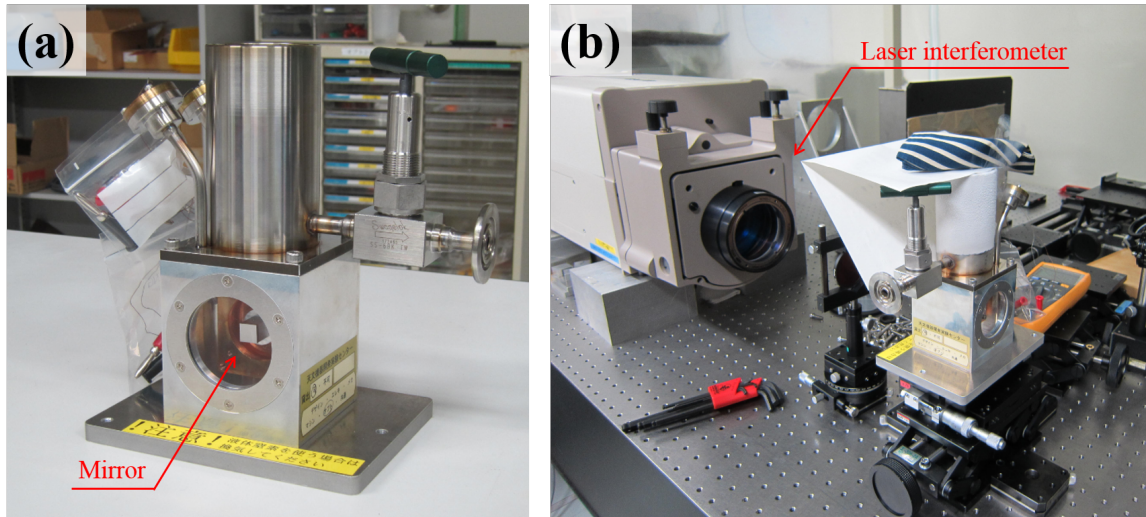


Fig. 6.7 (a) A cryo-dewar which cools mirror to LN2 temperature (~ 80 K). It has an optical window and a mirror mount made of oxygen-free copper. (b) The setup of measurement, with the laser interferometer and the dewar at the optical laboratory of Mitaka, NAOJ.

Table 6.3 Specifications of test pieces for cryo-measurements

substrate	mirror shape	Thickness [μm] ^(a)	CTE [K^{-1}] ^(b)	CTE [K^{-1}] ^(c)
A5052	Concave	100, 5	23×10^{-6}	$\sim 18 \times 10^{-6}$
RSA6061	(Size: 10 mm \times 10 mm, R = 70 mm)	20, 10	23×10^{-6}	18×10^{-6}
RSA443		100, 50	12.2×10^{-6}	$\sim 11 \times 10^{-6}$ ^(d)

(a) Thickness of NiP coating (μm)

(b) The value at 300 K.

(c) The value at $\sim 80\text{K}$.

(d) Kinast et al. (2014)

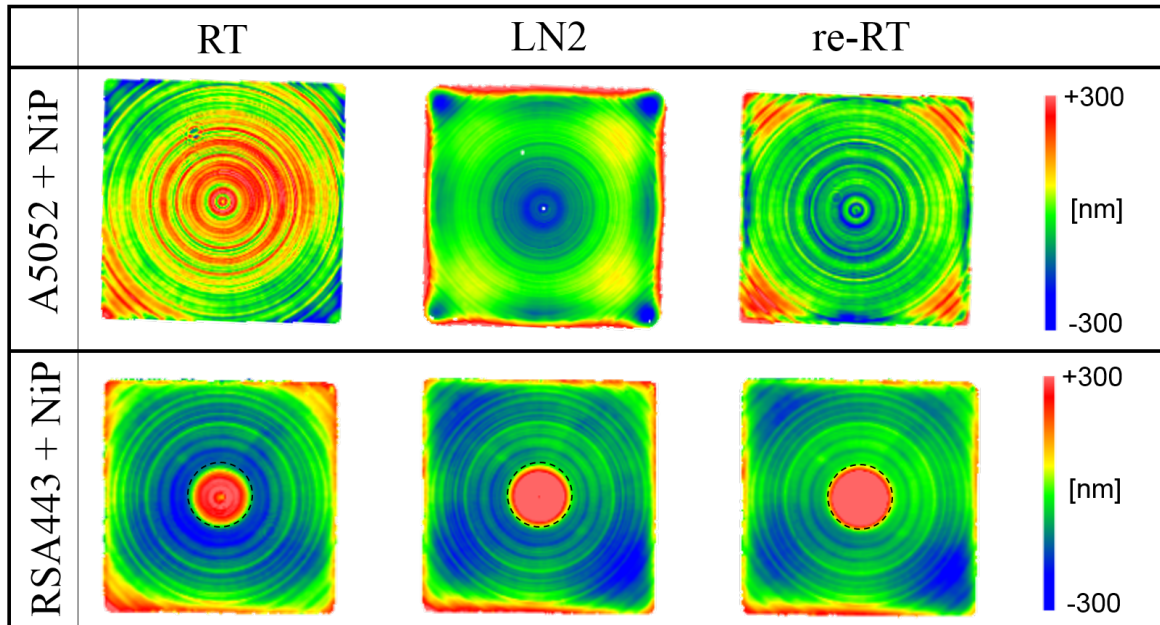


Fig. 6.8 Results of shape measurements. RT, LN2, and re-RT represent room temperature (300 K), liquid nitrogen temperature (77K), and room temperature after the thermal cycle (*i.e.* after elevating temperature). The top and bottom rows show the shape changes of A5052 and RSA443 with 100 μm of NiP plating at each temperature. Spike noise is removed by performing sigma clipping at each temperatures.

6.2.3 Results of Shape Measurement

Measurements are carried out at three temperatures of (i) room temperature, (ii) LN2 temperature, and (iii) room temperature again after cooling. The results are shown in Fig. 6.8.

In the case of A5052 substrate, a global shape change is observed. At the LN2 temperature, the deviation from the shape at room temperature is 740 μm . As the CTE of A5052 is $2.3 \times 10^{-6} \text{ K}^{-1}$, which is 1.8 times greater than that of NiP, the base material shrinks, and the concave shape tends to become a convex surface dragged by the base material. In addition, since the stress is concentrated at corners, distortion at low temperature is large. This suggests that if the mirror has the same curvature, distortion in the peripheral part is suppressed in the circular opening than in the rectangular opening.

On the other hand, in the case of RSA443 substrate, no significant change in the global shape is observed. The change in shape from room temperature is 80 μm , which clearly has a smaller value than that in the case of A5052. This is because RSA443 is designed to have almost the same CTE as that of NiP.

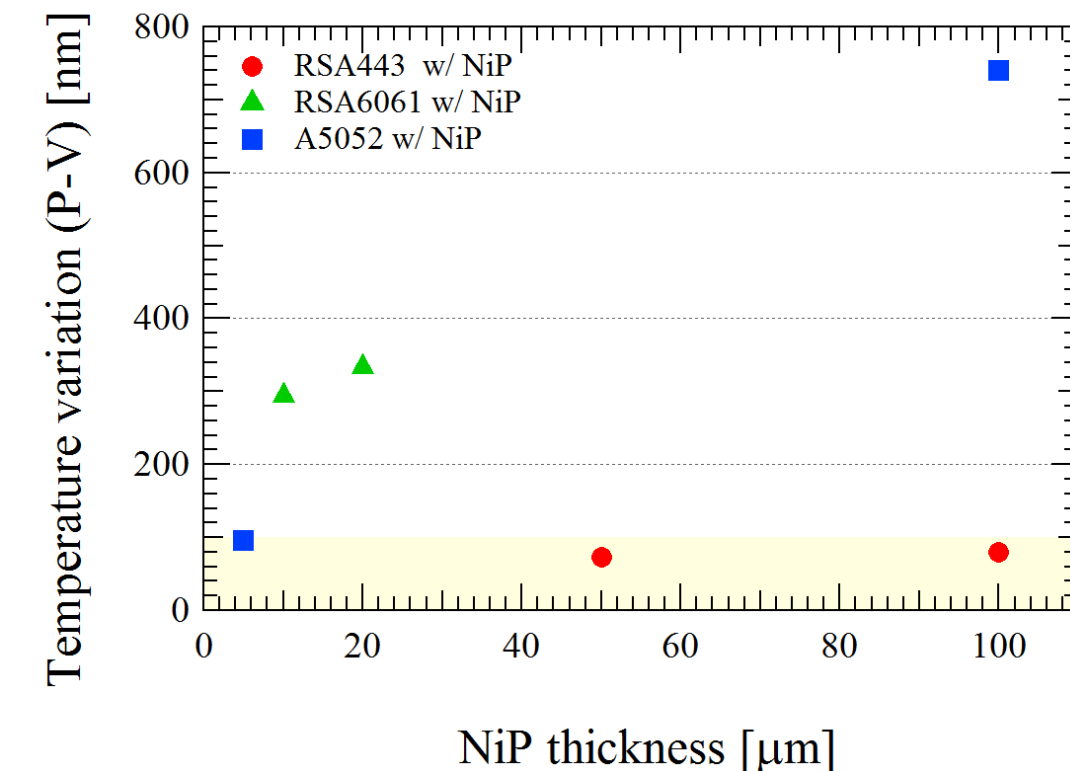
However, there is a hysteresis effect in which shape does not return to that before a thermal cycle. This trend is seen both in plating thicknesses of 100 μm and 50 μm as shown

in Fig. 6.9(b). The cause of the hysteresis may be a reduction in adhesion of plating to the substrate due to the high Si content of RSA443. Since Si is a nonmetal material, the nickel plating is supposed to be bonded only with aluminum, and has weakened in adhesion force. However, Kinast et al. (2014) has carried out , a similar experiment with NiP plated on AlSi42 with 100 μm thickness, and reported no such hysteresis. The differences between the experiments are that we do not heat-treat the base metal, and that they do not perform ultra-precision processing before plating, and the influence of mounting. However, since our workpiece is cut out from the core part of an aluminum alloy ingot, and the size is small, the influence of residual stress due to rolling can be ignored. Also, in our experiment, the axis of symmetry of the mirror is connected to a cold plate of the dewar with a single bolt and the distortion pattern should be axisymmetric, which is different from what observed. Therefore, a good surface processed by an ultra-precision machining is required before NiP plating. Improvement may be obtained by performing plating pretreatment optimized for high Si doping, but in any case further research is needed. Development of pre-treatment technique optimized for highly-doped Si aluminum is necessary, which must be a future work.

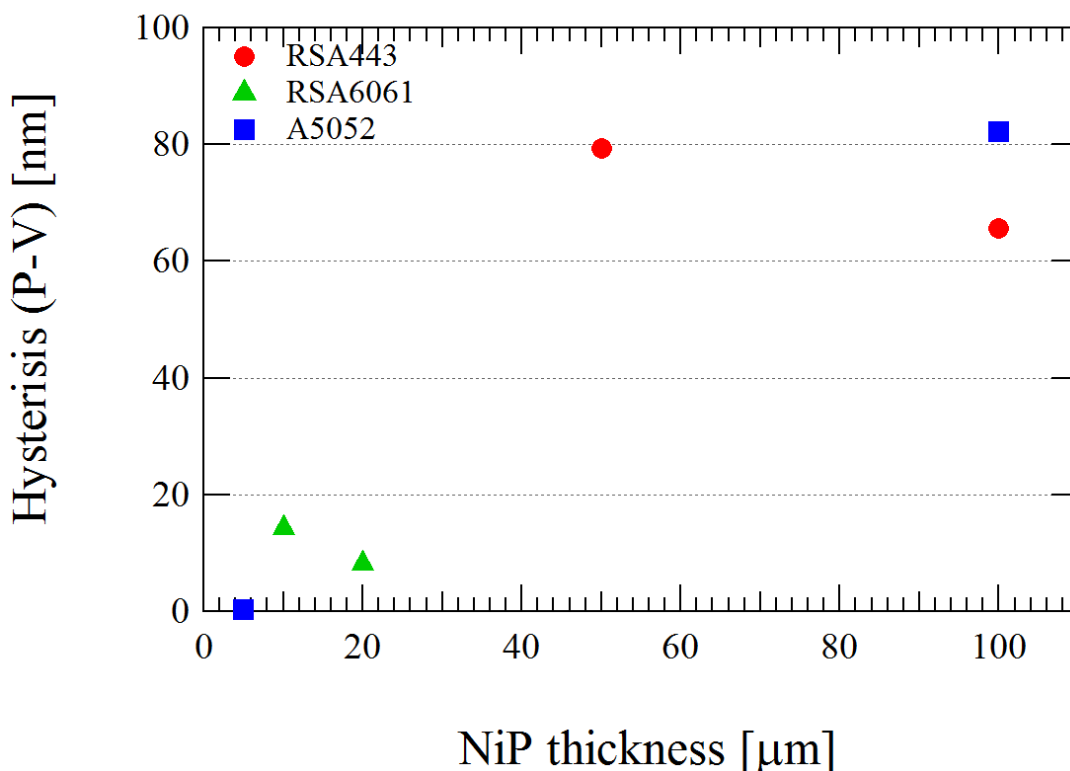
The plating-thickness dependence of deviation of shapes from those at room temperature is plotted in Fig. 6.9(a). The deviation of RA443 substrate becomes clearly smaller than that of A5052. When the plating thickness is 100 μm , deviation for RSA443 is $\sim 1/9$ of that of A5052, satisfying the specification of P-V < 0.1 μm .

Even when A5052 or RSA6061 is a substrate, shape distortion becomes smaller as plating thickness is made thinner as can be seen in Fig. 6.9(a). Note that there is no difference in CTE between RSA6061 and A5052 (Table 6.3). Fig. 6.9a(a) clearly shows that the deviation decreases almost linearly as the thickness of the plating decreases.

However, when the plating is thin, it is sensitive to the underlying conditions (surface roughness, precipitation of inclusions, etc.), and dents of plating such as pits and pinholes may be generated. Fig. 6.10 shows a profiles with the plating thickness of 5 μm , where pinholes are observed. The diameter of each pinhole is about 10–20 μm , and influence on optical performance to the near-infrared cannot be ignored. Although no shape distortion occurs plating with thickness of 5 μm cannot be practically used as a near infrared mirror because of the pinholes..



(a) Diviation component



(b) Residual component

Fig. 6.9 Dependence of deformation amount on thickness of NiP plating. Spike noise is removed by performing sigma clipping when deriving P-V values at each temperatures. (a) Difference value of P-V values between at room temperature and at liquid nitrogen temperature. Yellow-filled area indicates the range of 100 nm P-V corresponding to our requirements. (b) Difference value of P-V values between at room temperature and after elevating temperature.

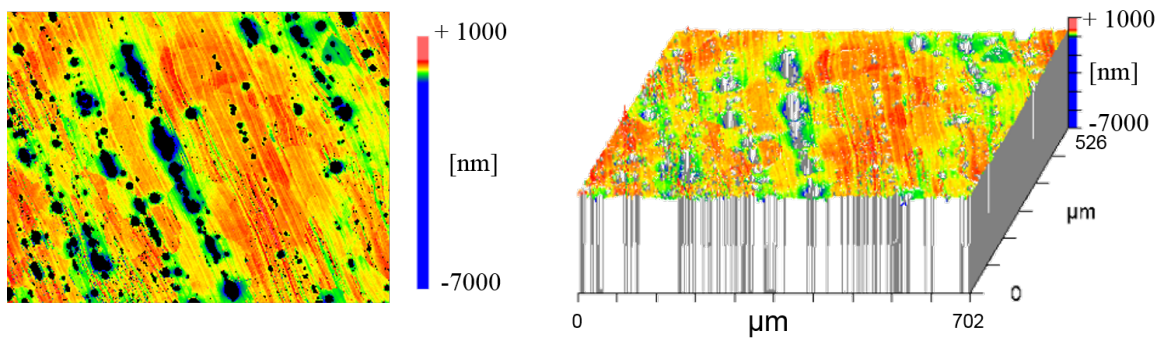


Fig. 6.10 Surface profile of NiP plating with a thickness of $5\ \mu\text{m}$. Many pores appear on the surface after diamond cutting. Some pores has a depth of $7\ \mu\text{m}$, and it reaches an aluminum substrate.

Table 6.4 P-V values of the surfaces at various temperature (row 3 to 5), of difference between room and LN2 temperature (row 6), and difference between before and after the thermal cycle (row 7).

Base alloys	Thickness (μm)	RT (nm)	LN2 (nm)	re-RT (nm)	Deviation (nm)	Residual (nm)
A5052	100	170.9	911.1	253.1	740.2	82.2
RSA443	100	412.8	492.9	478.4	80.1	65.6
RSA443	50	263.5	337.2	342.8	73.7	79.3
RSA6061	20	214.5	548.6	222.9	334.1	8.4
RSA6061	10	213.0	507.8	227.5	294.8	14.5
A5052	5	166.6	262.0	167.0	95.5	0.4

6.3 Summary

The results of our evaluation are summarized as follows.

- (1) Without a NiP plating, an oxygen-free copper is the best base material for diamond turning process. However, when we consider it as an infrared mirror for astronomy, its weight, price, and lower hardness will become problems. It is also necessary to overcome the mismatch of CTE with support structure (generally aluminum alloy). It is conceivable to use it for a metallic mirror for an optical instrument which does not require cooling.
- (2) Among aluminum alloys, RSA6061 has less surface defects and is suitable for use as a mirror. This is related to the manufacturing method of RSA6061, and it seems that the miniaturization of grain boundaries by the rapid cooling is effective. RSA905 is also very interesting, which can be directly polished, and further research will be necessary.
- (3) When plating is applied, the surface roughness of 5 nm is achieved even in cutting process. In addition, the surface profile has few defects and a homogeneous surface is obtained compared with aluminum alloy. This is due to the fact that electroless NiP has an amorphous and homogeneous structure without precipitation of grain boundaries. The greatest advantage of NiP plating is the polishability. Cutting marks can be eliminated by post-polishing after cutting, and the surface roughness of few nm can easily be achieved.
- (4) We confirmed that the bimetal effect appears with NiP coated A5052 and RSA6061 at cryogenic temperature, which caused by mismatch in CTE. The shape distortion reaches 300–800 nm P-V, and it is found that mirrors with nickel plating on these alloys cannot be used as a cryogenic temperature optical system. The dependency of the distortion on plating thickness appears clearly, which is explored in this study for the first time. When the plating thickness is 5 μm , the shape distortion due to the bimetallic effect is $\sim 0.1 \mu\text{m}$ and fit within the requirement. However, with such thin plating, many surface defects appear as shown in Fig 6.10, so it is expected that optical performance will be significantly impaired.
- (5) It is experimentally confirmed that the bimetallic effect is obviously suppressed for the special aluminum alloy RSA443 optimized to match the CTE of NiP plating, and that the required shape error of 0.1 μm is satisfied. However, a shape difference between a thermal cycle appears. This may be caused by lowered adhesion between plating and substrate, which has not been reported in previous studies (Kinast et al., 2014). Further

research such as condition of the front surface to be plated and the pretreatment of the plating are necessary.

In summary, we show that a high-Si containing aluminum alloy RSA443 is optimal for the infrared optical system, which can significantly suppress the bimetal effect.

Part II

Spatially resolved study of Starburst galaxies

Chapter 7

Introduction of Part II

7.1 Star formation main sequence

7.1.1 Integrated Study

In recent years, it has been understood that there is a strong correlation between star formation rate (SFR) and stellar mass (M_*) of star-forming galaxies. This is called “star formation main sequence (SFMS)”, which is an important concept to study galaxy formation and evolution because it can be used as a benchmark to test results of hydrodynamical simulations of galaxies (Kannan et al., 2014; Sparre et al., 2015). SFMS is investigated at various redshift from present universe to $z \sim 2-4$ (Daddi et al., 2007; Katsianis et al., 2016; Wuyts et al., 2011) in multi-wavelength observations (Elbaz et al., 2011; Tasca et al., 2015). Normalization and scatter of SFMS are important observables which reflect physical condition of star formation in galaxies at given redshift. Normalization of SFMS changes depending on redshift, and increases towards high-redshift (Whitaker et al., 2012). Scatter of distribution is affected by intrinsic (*e.g.* star formation history) or extrinsic (*e.g.* observation error) factor, and earlier studies suggest contribution from the later is small ($\sigma < 0.2-0.3$ dex) (Salmi et al., 2012; Speagle et al., 2014).

There are also galaxies with high specific star formation rate ($sSFR \equiv SFR/M_*$) deviating upward from the SFMS unlike many star-forming galaxies located on the relation, suggesting intense star formation activities. A galaxy deviated highly above the SFMS at a certain redshift is defined as “starburst galaxy.” Since the SFMS relation shows redshift evolution, a starburst galaxy at $z \sim 0$ is categorized into a “normal” star-forming galaxy at $z \sim 1-2$. This fact motivates us to study nearby starburst galaxies as local analogs of high- z star-forming galaxies.

7.1.2 Spatially-resolved Study

Recent IFS studies enable us to analyze SFMS from a spatially resolved view while all of the studies mentioned above are derived from integrated quantities. Cano-Díaz et al. (2016) shows that there are also correlation between spatially-resolved properties of star formation rate surface density (Σ_{SFR}) and stellar mass surface density (Σ_{M_*}), with optical IFS observations of local star-forming galaxies. This spatially-resolved SFMS relation has a slope and an intrinsic scatter similar to those of the integrated relation. IFS studies in the near-infrared wavelength is also important (Pereira-Santaella et al., 2016; Piqueras López et al., 2016) because starburst galaxies have a large amount of dust due to their intense star formation activities.

7.2 Role of Starbursts in Galaxy Evolution

The modern infrared astronomy opened in the 1950s, and have established an important position in the astronomy by dedicated researches using various infrared telescopes/instruments at both ground and space observatory such as UKIRT, IRAS, ISO, Hubble/NICMOS and so on (also see short reviews in Storey (2000); Walker (2000)). Intense infrared surveys found many galaxies brightly emitting in the infrared-band (Armus et al., 2009; Lonsdale et al., 2003; Sanders et al., 2003). These population are characterized by their total infrared luminosity: $L_{\text{IR}} \equiv L_{8-1000\mu\text{m}}$ and are called luminous infrared galaxies (LIRGs) for $\log(L_{\text{IR}}/L_{\odot}) = 11-12$ or ultra luminous infrared galaxies (ULIRGs) for $\log(L_{\text{IR}}/L_{\odot}) > 12$ (Sanders and Mirabel, 1996). These LIRG / ULIRG are bright in the infrared wavelength due to infrared radiation from dust re-radiation heated by intense star formation activity or AGN. Throughout this part, we refer nearby LIRG / ULIRG to “starburst galaxies.”

Thanks to recent developments in infrared optics and semiconductor detectors, infrared spectroscopic observations have brought about new developments in galactic astronomy. A redshift range of $1.4 < z < 2.5$, which is called the “redshift desert” from which the rest-optical features (e.g. $\text{H}\alpha$) move outside of the sensitivity of CCD detector, has been newly observed by near infrared spectrographs (Steidel et al., 2004). From these observations, it has become clear that the star formation activities of the universe reached a peak in the period of $z \sim 1-2$ (“cosmic noon”) (Madau and Dickinson, 2014). The cosmic noon is a era of great transition in the context of galaxy formation and evolution. The galaxies in the cosmic noon show a star formation rate which is nearly two orders of magnitude higher than that of the galaxies in the current universe (Daddi et al., 2007; Pannella et al., 2015), and it is also reported that their gas fraction is higher than that in the nearby galaxies (Scoville et al., 2016; Tacconi et al., 2013). Morphology of galaxies in the redshift range are looks quite

different from that in the present universe (Delgado-Serrano et al., 2010; Schade et al., 1996): Many star-forming galaxies have large clumpy star-forming regions within their disks. Also, there are many galaxies which have disturbed morphology (Elmegreen et al., 2009; Guo et al., 2015) rather than grand-designed spiral or elliptical-like shape that are common feature in the present universe. Examining these high- z clumpy galaxies will give an important to understand knowing the mechanism of the emergence of the galaxy morphology.

7.3 Scope of Part II

It is important to spatially resolve each star-forming region within high- z starburst galaxies since the star formation would be governed by local physics with a scale of < 1 kpc (*i.e.* a typical size of giant molecular cloud). However, in the era of $z > 1$, the spatial resolution of current facilities is insufficient to decompose the galaxies. For example, natural seeing observations at ground-based telescopes are limited to resolutions of $\sim 0.''8$ corresponding to 8–11 kpc at $z \sim 1$ –2. Even when adaptive optics can be used for near-infrared observation, the resolution remains at $\sim 0.''2$ corresponding to 2–3 kpc. Using strong gravitational lensing, substructure of the galaxies with high-resolution of sub-kpc (Jones et al., 2010; Nierenberg et al., 2014) can be detected. However, strong gravitational lensing requires both a background source and a foreground lens aligned along a line of sight from the observer, and statistical discussion becomes difficult due to the small number of samples.

It suggests that correspondence exists between a local starbursting LIRG and a star-forming galaxy at high- z (Pannella et al., 2015; Stierwalt et al., 2013), thus we refer nearby LIRG / ULIRG to “starburst galaxies” in the following discussion. It is useful to examine nearby starburst galaxies as a counterpart of high- z galaxies, because we can easily achieve high spatial resolution in nearby galaxies. For example, if we use an adaptive optics in a galaxy at a redshift $z < 0.1$, the spatial resolution reaches < 0.4 kpc. Of course, such a high physical resolution at $z > 1$ can be achieved by extremely large telescopes such as TMT, E-ELT and GMT which will be commissioned in the 2020’s.

These local LIRG/ULIRG galaxies shows large dust extinction (Piqueras López et al., 2013), suggesting that the star-forming regions are embedded in highly dusty environments. Then, it is difficult to use hydrogen $H\alpha$ emission line in visible wavelength as a tracer of star-forming regions. In contrast, observations in far infrared rays and submillimeter waves are hardly influenced by dust absorption, but spatial resolution becomes worse as the wavelength becomes longer.

Therefore, we propose observations focusing on the Pa α emission line from ionized hydrogen in the near infrared wavelength. Since Pa α ($\lambda_0 = 1.875 \mu\text{m}$) becomes stronger than H α in dusty environment, it is a good probe of star formation activities in dusty environments.

There are several Pa α observations of nearby starburst galaxies using HST/NICMOS (Díaz-Santos et al., 2008). However, rest-wavelength of Pa α emission line is sensitive to absorption by Earth atmosphere (Konishi et al., 2015), and greatly absorbed so its observation from ground-based observatories is difficult, and we have to focus on redshifted objects. The study on the nearby starburst galaxies focusing on Pa α is unique and there is a possibility to approach the origin of the star formation activity of the starburst galaxy.

In part II, we first describe PARADISES survey using Pa α emission line as an indicator of star formation activity in chapter 8. The survey is aimed at systematically investigating spatially resolved internal structure of both star-forming activity and dynamical state within nearby starburst galaxies. As the first step of the survey, observation results of near infrared imaging with spatial resolution of sub-kpc using adaptive optics are shown in chapter 8 and 9. We show the “spatially resolved” version of SFR- M_* relationship that has played a useful role in studying star formation activities in context of galaxy evolution in Chapter 10. The result shows that the PARADISES samples also perform intense star formation activity. We discuss properties of the star formation clump detected by Pa α emission with sub-kpc resolution and also discuss similarity with giant star-forming clumps seen in high- z universe. These interesting objects obtained from the PARADISES survey can be considered to be good candidates for follow-up observation using SWIMS-IFU.

Throughout this part we adopt a standard cosmology with $\Omega_m = 0.3$, $\Omega_\Lambda = 0.7$, $H_0 = 70 \text{ km s}^{-1} \text{ Mpc}^{-1}$ (Komatsu et al., 2011). The angular size of $1.''0$ corresponds to 2.01 kpc at $z = 0.11$.

Chapter 8

Sample and Data

8.1 PARADISES Survey

8.1.1 Survey Description

We are implementing the Pa-Alpha Resolved Activity and Dynamics of Infrared Selected Extreme Starbursts (PARADISES) survey. This survey aims to dissect the star formation activity buried in dust inside the galaxy by narrow-band imaging observations of hydrogen Pa α emission in order to understand the galactic interaction and the galactic evolution process.

Pa α emission line ($\lambda_0 = 1.875 \mu\text{m}$) is an index of a massive star formation activity which is less susceptible to dust attenuation compared with visible or ultraviolet light. Intrinsically, Pa α emission is weaker than H α ($\lambda_0 = 0.653 \mu\text{m}$), but becomes stronger compared with H α in starburst galaxies with large attenuation due to dust.

This surveys are achieved by a near-infrared imager; Infrared Camera and Spectrograph for the Subaru Telescope (IRCS), and their narrow-band (NB) filters shown in Table 8.1 which cover the redshifted Pa α emission line. The targets are selected from galaxies detected in the 90 μm band by the AKARI all-sky survey (matched with SDSS), and the details are described in section 9.2.2 . The observational strategy is as follows.

(Phase 1) Observation of NB imaging by IRCS on Subaru (Kobayashi et al., 2000) is performed. Identification of the star-forming region and mapping of star formation, including those embedded in dust clouds, at the 1 kpc scale can be done by the Pa α emission line. As Pa α is less susceptible to dust attenuation, it is possible to find a star formation region buried in dust which cannot detected with H α emission line.

Table 8.1 Total number of observable targets with IRCS

Filters	λ_{cen} [μm] ($\Delta\lambda$ [μm]) ^a	Redshift	Candidate	Observed
NB2090	2.091 (0.035)	0.105 – 0.124	103	6 (2 ^b)
H ₂ (1–0)	2.122 (0.032)	0.123 – 0.140	58	3

^a A central wavelength and width of the filters.

^b Number of objects observed with AO188.

(Phase 2) Integral field spectroscopic follow-up with SWIMS-IFU is performed, and a data cube of 0.9–2.5 μm can be acquired with one exposure. This clarifies the gas motion of the star-forming regions. Also, we can derive an A_V map (*i.e.* two-dimensional dust distribution) using the Balmer decrement such as $\text{Pa}\alpha/\text{Br}\gamma$.

8.1.2 Target Selection

From the AKARI + SDSS catalog, we select LIRG/ULIRG class starburst galaxies whose $\text{Pa}\alpha$ emission line redshifts to the NB filters of IRCS (Koyama in prep). Table 8.1 shows the NB filters installed in the IRCS with their redshift range ($z \sim 0.11\text{--}0.14$) We also take into account of their observability from the Subaru telescope, and limited their declination to be $\text{Dec} > 30^\circ$. Among the candidate targets of PARADISESs survey, we observe seven galaxies under seeing conditions, and carry out high spatial resolution observations assisted by an adaptive optics facility for two targets satisfying the condition of having tip-tilt guide stars with $R < 16.5$ mag, distance $< 30''$.

These two galaxies have remarkably different features in an infrared luminosity and an optical morphology as explained below:

NB209-096: The tip-tilt guide star is located about $17''$ southwest away, and its SDSS r -band magnitude is 15.87. This galaxy is categorized into *starbursts* in SDSS DR12. Optical magnitude in the SDSS u -band and z -band are 19.89 and 17.57 in the AB-system, respectively. The K -band magnitude estimated from our observation is 13.30 in the Vega-system, and the total infrared luminosity derived from the AKARI FIR source catalog is $\log L(\text{IR}) = 12.23$ which is classified as ULIRG. The star formation rate estimated from the infrared luminosity is $\text{SFR}(\text{IR}) = 201 \text{ M}_\odot \text{ yr}^{-1}$ indicating intense star formation activity while the star formation rate estimated from $\text{H}\alpha$ without dust attenuation correction is $\text{SFR}(\text{H}\alpha) = 1.6 \text{ M}_\odot \text{ yr}^{-1}$. As seen in the left panel of Fig. 8.2, this galaxy seems to have double cores in addition to features extending north and east. Almost all the ULIRGs are merger systems in the nearby universe (Sanders and Mirabel, 1996), and the disturbed morphology of this galaxy is consistent with it.

NB209-097: The tip-tilt guide star is located about $18''$ southwest away, and its SDSS r -band magnitude is 14.33 mag. This galaxy is categorized into *star-forming* in SDSS DR12. Optical magnitude in the SDSS u -band and z -band are 17.85 and 15.48 in the AB-system, respectively. The K -band magnitude estimated from our observation is 13.54 in the Vega-system, and the total infrared luminosity derived from the AKARI FIR source catalog is $\log L(\text{IR}) = 11.86$ which is classified as LIRG. The star formation rate estimated from the infrared luminosity is $\text{SFR}(\text{IR}) = 34 M_{\odot} \text{ yr}^{-1}$ while the star formation rate estimated from $\text{H}\alpha$ without dust attenuation correction is $\text{SFR}(\text{H}\alpha) = 0.96 M_{\odot} \text{ yr}^{-1}$. As seen in the right panel of Fig. 8.2, this galaxy shows a disc-like morphology in the optical image. There is a companion with the same redshift ($z = 0.1115$) at about 20 kpc apart from the galaxy. This companion has $\text{SFR}(\text{H}\alpha) = 0.6 M_{\odot} \text{ yr}^{-1}$, and a stellar mass ratio to NB209-097 is about 1/10 (the MPA/JHU catalogue; <http://wwwmpa.mpa-garching.mpg.de/SDSS/DR7/>). Since a bridge-like feature or tidal tails are not confirmed in the optical image, it is expected that they have not experienced the first encounter and will cause minor merger in the future.

8.2 AO Observations using Subaru/IRCS

We perform near-infrared imaging observations using the Infrared Camera and Spectrograph (IRCS), which is one of the first-generation instruments of the Subaru telescope. It has capability of both imaging and spectroscopic observation at near infrared wavelength of 1–5 μm (Kobayashi et al., 2000), and still allows us to perform versatile near-infrared observations through its several major performance upgrade (Terada et al., 2004). The imaging mode of IRCS is optimized for high spatial resolution with AO facility with wider field-of-view of $60'' \times 60''$. The IRCS filter set consists of the basic J , H and K' filters for broad bands in addition to NB filters optimized for various emission lines.

One advantage of IRCS is the Subaru AO system (AO188). AO188 is an adaptive optics system installed at the Nasmyth platform of the Subaru telescope and consists of 188-elements wavefront sensor (Minowa et al., 2010). It can be operated in both natural and laser guide star modes. Therefore, we obtain high-spatial resolution images with comparable spatial resolution as that of the Hubble space telescope and with high sensitivity thanks to the large aperture of the Subaru telescope.

We conduct AO-assisted observations using the K' -band filter ($\lambda_{\text{cen}} = 2.12 \mu\text{m}$, $\Delta\lambda = 0.35 \mu\text{m}$) and the NB209-filter ($\lambda_{\text{cen}} = 2.09 \mu\text{m}$, $\Delta\lambda = 0.035 \mu\text{m}$). Total exposure times are almost the same for both targets, where 200 sec for the K' -band filter and about 1000 sec for the NB209-filter. Table 8.2 summarizes the observational logs. As shown in Fig. 8.1, the central

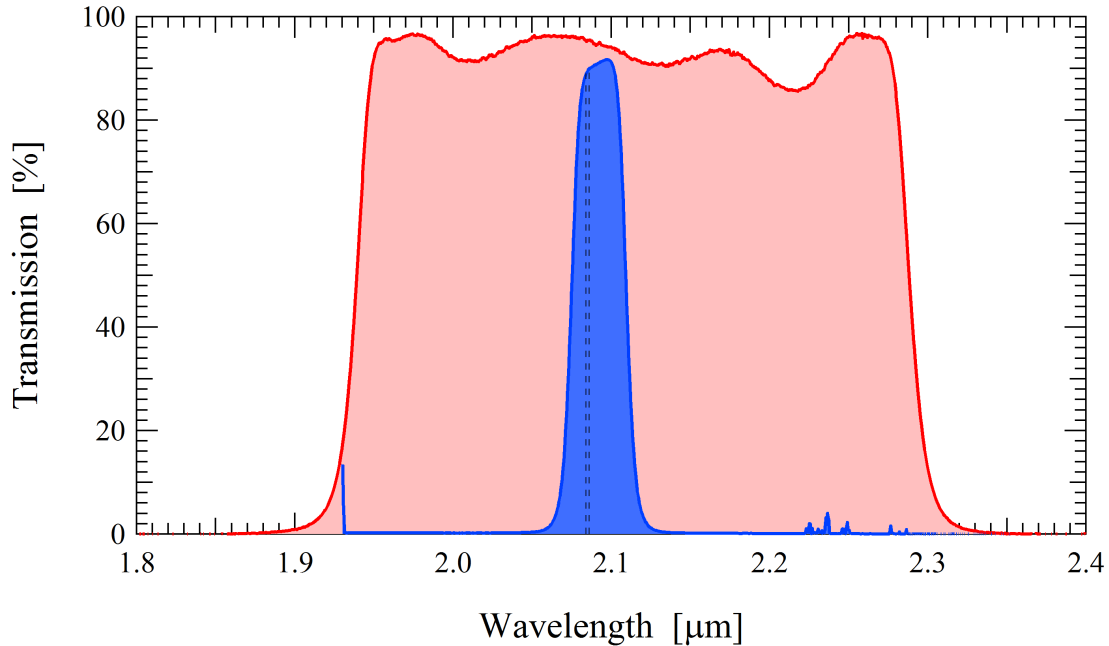


Fig. 8.1 Transmittance curve of the K' -band and the $NB209$ -filters of IRCS. The red and blue lines represent the transmittance curve of K' -band, and the $NB209$ -filters, respectively. The two dashed black lines correspond to the redshifted $\text{Pa}\alpha$ emission line of the AO188 targets ($z = 0.1125$ and 0.1115).

wavelength of the $NB209$ -filter is located almost at the center of the K' -band. The central wavelength corresponds to the wavelength at which $\text{Pa}\alpha$ emission line is redshifted to $z = 0.115$.

In this condition, we achieve FWHM of $0.''20$ in both the K -band and the $NB209$ images measured using five stars in the images, which corresponds to a resolution of 400 pc at the redshift of 0.11. We also estimate the Strehl ratios of both the K -band and $NB209$ filters of $NB209-097$ by synthesizing diffraction-limited PSFs at the wavelength of $2.12 \mu\text{m}$ and $2.09 \mu\text{m}$. We pick out a star close to the galaxy near the center of the field-of-view, and read the peak value of the star after converting its count to that of the diffraction-limited PSF. The derived Strehl ratio is 0.057 for the K -band image and 0.055 for the $NB209$ image. Although these values are not the best performance of AO observations in the K band of IRCS, they are within a reasonable range under a typical observational condition (*e.g.* Minowa et al. (2010)).

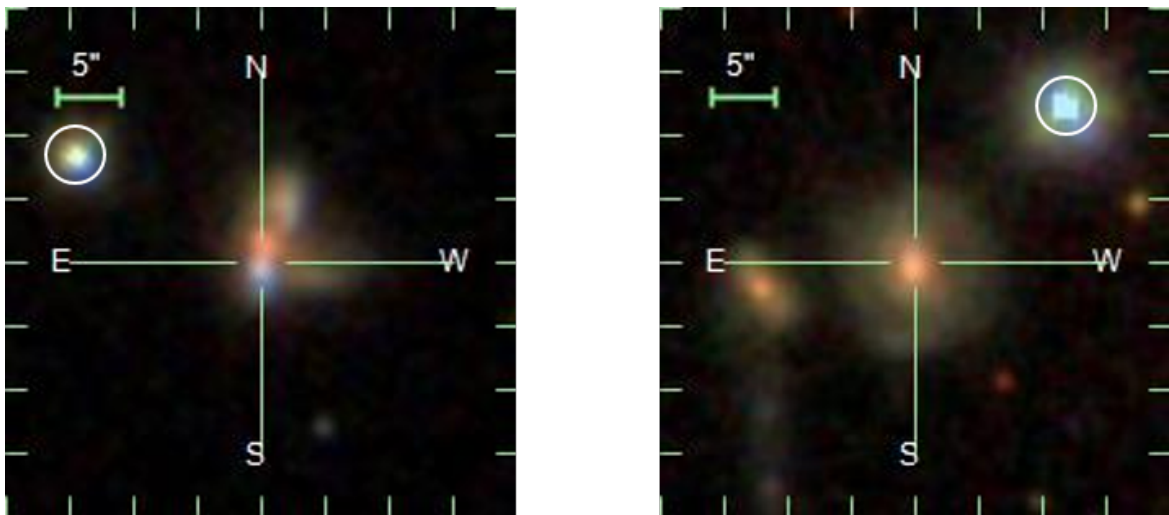


Fig. 8.2 Composite images of the targets; NB209-096 (left) and NB209-097 (right), taken from SDSS SkyServer DR12. White circles in the images indicate tip-tilt guide stars for AO188 observations.

Table 8.2 AO188 observations

ID (PARADISES)	ID (AKARI)	redshift ^a	D_L (Mpc) ^b	scale (kpc ²) ^b	K' ^c	NB209 ^c
NB209-096	AKARI-FIS-1649140+342510	0.112	522.5	2.047	200 sec	1000 sec
NB209-097	AKARI-FIS-2103012-002031	0.111	517.4	2.030	200 sec	900 sec

^a Redshift taken from SDSS DR12. The redshift of NB209-096 and NB209-097 are photometrically and spectroscopically confirmed, respectively.

^b Physical scale using *Cosmology Calculator* (Wright, 2006).

^c Total exposure time of each filter.

8.3 Data Reduction

Data reduction is performed according to the standard procedure of near-infrared imaging. First, a sky flat is created and the sensitivity unevenness of the detector is corrected using it. Then, a sky frame for each dithering set is created and sky subtraction is performed. Finally, an object position is adjusted, and coadded it to create the object image. Standard stars are acquired in both the *NB209* band and the K' -band filters and reduced in the same procedure as the targets. These series of reductions are performed using a Python-based IRCS pipeline (`ircs_imgred_v0.6`).

The image of Pa α emission line is synthesized as follows. First of all, a continuum image from the K' -band image and the narrow band image are created by the following formula.

$$f_{cont} = \frac{f_{K'} \times \Delta K' - f_{NB} \times \Delta NB}{\Delta K' - \Delta NB} \quad (8.1)$$

Here, $f_{K'}$ and f_{NB} are K band flux density and NB flux density, respectively, and $\Delta K'$ and ΔNB are the bandwidths of the K' -band and of the NB filters (Table 8.1). Here, we assume that the flux density of the continuum component is equal for both the K' -band and the NB filters, and the flux of Pa α emission line is equal for both band filters.

The synthesized Pa α images are shown in Figs. 8.3a and 8.3b. Bright regions emitting in Pa α are detected clearly on both targets.

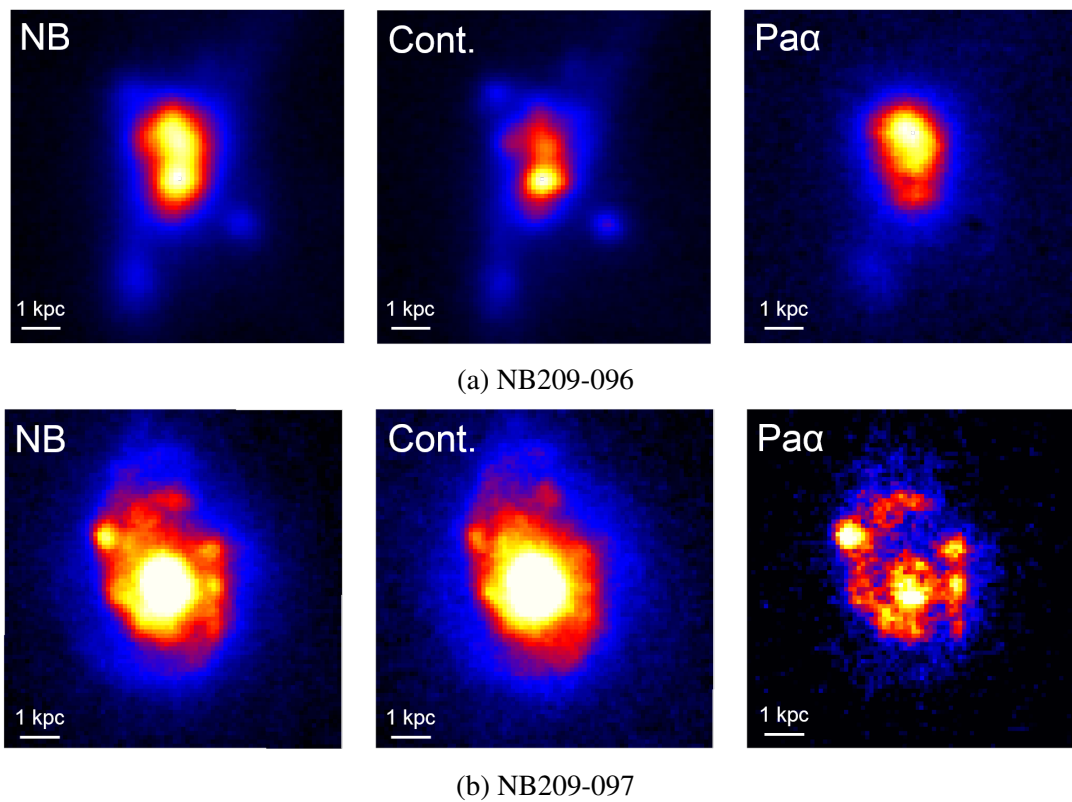


Fig. 8.3 NB, continuum, and derived Pa α images.

Chapter 9

Resolved Star Formation Activities

9.1 Deriving Physical Quantities

9.1.1 Star Formation Rate

Accurately estimating the star formation rate (SFR) of a galaxy is one of the important tasks of galaxy astronomy. Continuum components or bright emission lines of various wavelengths have been used as tracers of star formation (Calzetti (2013); Kennicutt and Evans (2012) and references therein). In our research, we focus on the near-infrared hydrogen recombination emission line, Pa α . The advantage of using Pa α is that it directly traces star formation regions and also is less affected by dust attenuation compared with H α ($A_{H\alpha}/A_{Pa\alpha} \simeq 0.18$, Alonso-Herrero et al. (2006)). Furthermore, it can achieve high spatial resolution compared to far infrared and submillimeter wavelength.

Star formation rates are estimated from Pa α luminosities as follows. A relationship between H α luminosity and star formation rate is taken from Kennicutt (1998a) where Salpeter IMF is assumed;

$$SFR [M_{\odot}\text{yr}^{-1}] = 7.9 \times 10^{-42} L_{H\alpha} [\text{erg s}^{-1}]. \quad (9.1)$$

By applying the intrinsic line intensity ratio of H α /Pa α = 8.6 assuming $T = 10000$ K and $n_e = 10^4 \text{ cm}^{-3}$ (Hummer and Storey, 1987), the following equation is obtained.

$$SFR [M_{\odot}\text{yr}^{-1}] = 6.8 \times 10^{-41} L_{Pa\alpha} [\text{erg s}^{-1}]. \quad (9.2)$$

We adopt the Salpeter IMF (Salpeter, 1955) and no dust attenuation correction is performed. When previous studies use a different IMF, we employ the conversion factors of 1.59

and 1.44 (Calzetti et al., 2007; Kennicutt et al., 2009)) for Chabrier IMF (Chabrier, 2003) and Kroupa IMF (Kroupa, 2001), respectively, to compare with our results.

The total Pa α luminosities are measured with aperture with diameters of 20.''8 and 10.''4 diameters for NB209-096 and NB209-097, respectively, which are chosen to be large enough to contain nearly all flux of the galaxies. The center of the apertures are set at a peak of the contour of the continuum image of each object. The obtained SFR is summarized in Table 9.1. The star formation rates without dust correction are about 117 $M_{\odot}\text{yr}^{-1}$ and 34 $M_{\odot}\text{yr}^{-1}$ for each galaxies, which are nearly one order of magnitude higher than that of a typical star-forming galaxy at the redshift of ~ 0.1 .

Fig. 9.1 shows that the spatial distribution of star formation activity is quite different in each galaxy. In NB209-096, there is no substructure in the star formation activity, and intense star formation activity is seen in the whole region. On the other hand, NB209-097 has a ring-shaped star formation region with a radius of ~ 1.5 kpc surrounding the center, and several star-forming blobs are seen in it.

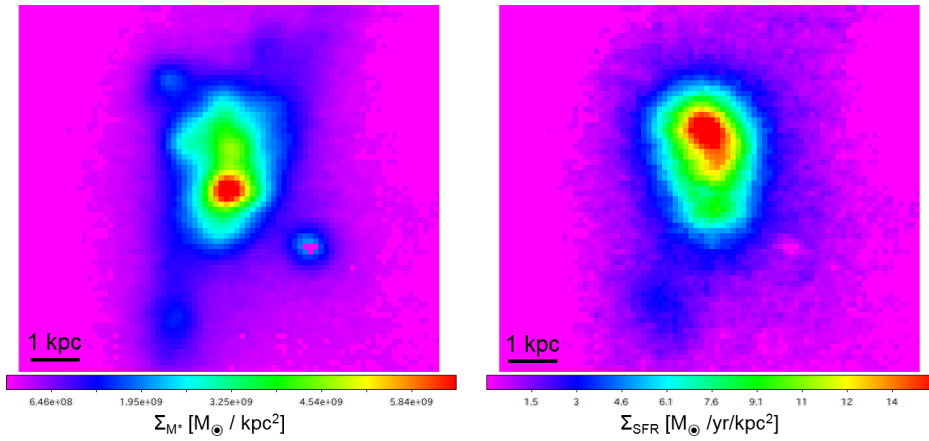
9.1.2 Stellar Mass

We estimate the stellar mass of the galaxies using a stellar mass-to-light ratio (M/L) of the K -band derived in Zibetti et al. (2009). They adopt the stellar population synthesis model developed by Bruzual and Charlot (2003), which incorporates the evolutionary phase of the thermally pulsing asymptotic giant branch stars, and derive the relation of the total stellar mass-to-light ratio using L_K with an optical color correction.

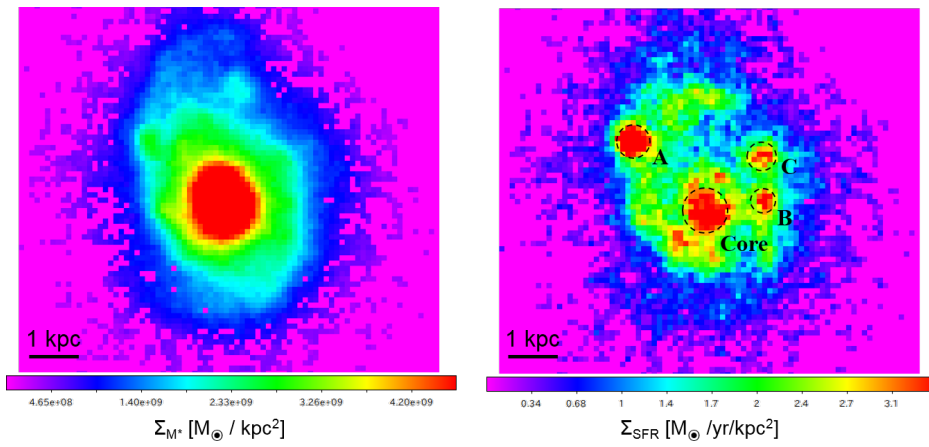
$$\log(M/L_K) = -1.405 + 1.157 \times (r - z). \quad (9.3)$$

The colors used are shown in Table 9.1. An integrated stellar mass (M_*) is calculated from the K' -band luminosity in solar units (L_K) measured in the continuum image with the same aperture sizes as described above. We apply the fixed values of M/L_K in Table 9.1 to each pixels in the continuum images to derive spatially resolved stellar mass maps (*i.e.* stellar mass surface density maps).

Fig. 9.1 shows the stellar mass density maps obtained for the both galaxies. An offset of about 1 kpc is seen in the peak of stellar mass accumulation and that of star formation activity for NB209-096, whereas the peaks of the largest star-forming clump and star mass accumulation nearly matches in NB209-097.



(a) NB209-096



(b) NB209-097

Fig. 9.1 Surface density map of stellar mass (left) and SFR (right) of the galaxies. The black circles shown in the lower right panel represent the identified Pa α clumps.

Table 9.1 Summary of SFR and stellar mass

ID (PARADISES)	SFR(Pa α) [M $_{\odot}$ /yr]	sSFR [1/Gyr]	Σ_{SFR} [M $_{\odot}$ /yr/kpc 2]	sdss (r-z)	$\log(M/L_K)$	M_* [M $_{\odot}$]
NB209-096	117.2 \pm 20.5	2.2 \pm 0.4	0.33 \pm 0.06	0.52 \pm 0.03	-0.80 \pm 0.04	(5.1 \pm 0.4) \times 10 10
NB209-097	33.8 \pm 5.9	0.50 \pm 0.09	0.39 \pm 0.07	0.75 \pm 0.01	-0.54 \pm 0.01	(6.8 \pm 0.2) \times 10 10

9.2 Results

9.2.1 Integrated $SFR - M_*$ relation

The relationship between star formation rate and stellar mass is shown in Fig. 9.2 and the physical quantities derived for each object are summarized in Table 9.1. The sSFR of our targets shows 1–2 orders of magnitude larger than those of the main sequence galaxies at the same redshift of $z = 0.1$. This suggests that these objects are categorized into starburst galaxies at $z = 0.1$, and are almost located on SFMS at $z \sim 1-2$. We will discuss this in detail in Chapter 10.

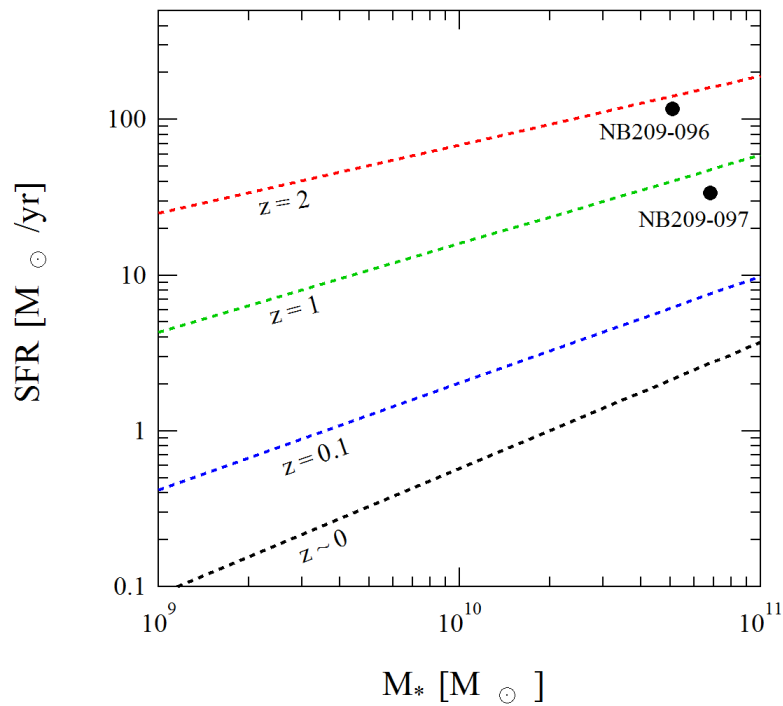


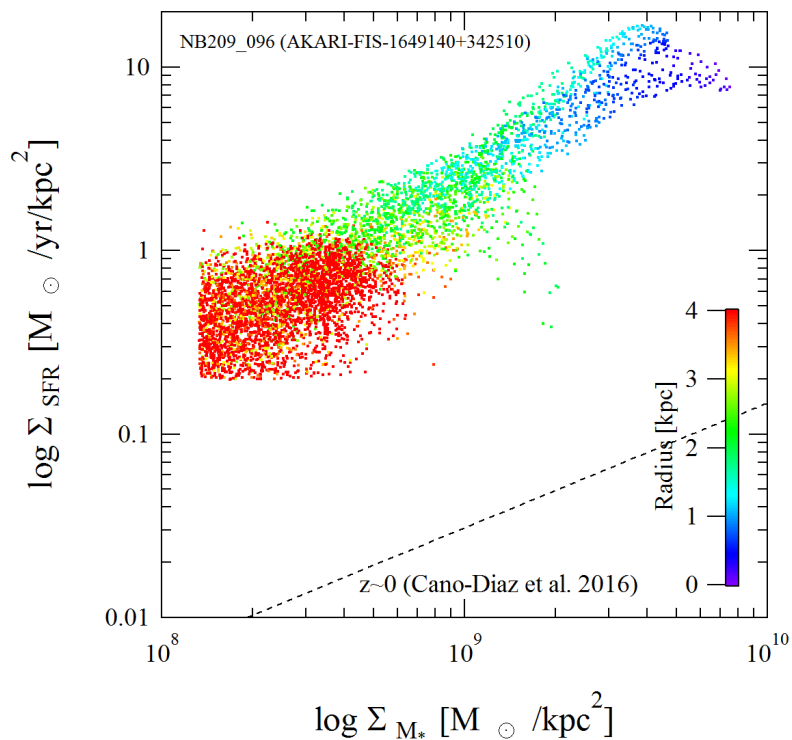
Fig. 9.2 Star-formation rate versus stellar-mass plot. Our targets are represented by black filled circles. Star formation rate and stellar mass are estimated as described in Section 10.1. The black dotted line shows the main sequence relation in local spiral galaxies obtained from the CALIFA survey covering the redshift of $0.005 < z < 0.03$ (Cano-Díaz et al., 2016). The blue, green, and red dotted lines indicate the relationship at $z = 0.1$, 1 and 2, respectively, of which the slope and the normalization are calculated using analytical equation given by Whitaker et al. (2012). Our targets at $z = 0.11$ largely exceed the main sequence relation at the same redshift.

9.2.2 Mapping Σ_{SFR} vs. Σ_{M_*}

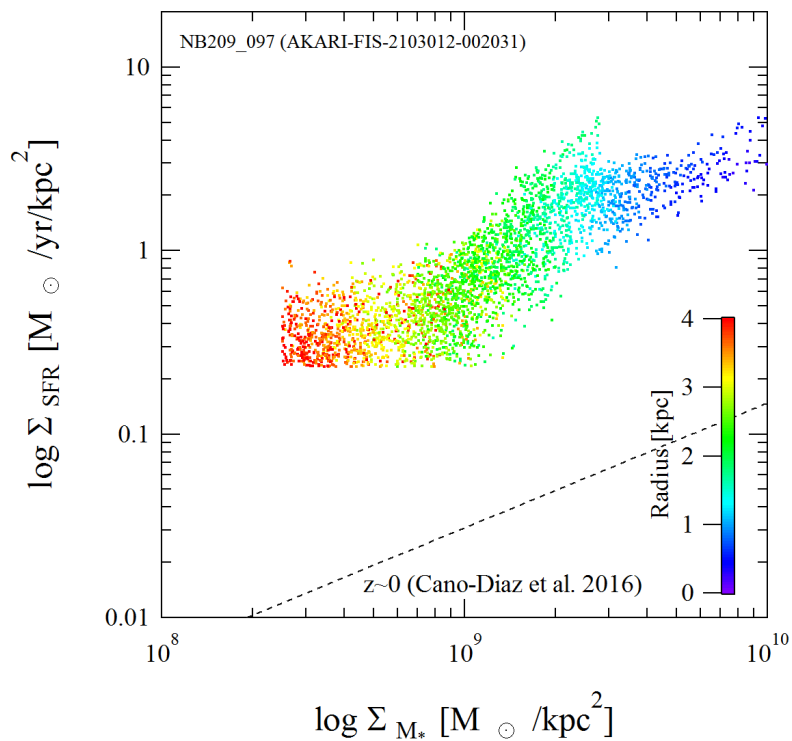
Next, we show the relationship between star formation surface density (Σ_{SFR}) and stellar mass surface density (Σ_{M_*}). This is a pixel-to-pixel plot of the star formation rate map and the stellar mass map shown in Fig. 9.1. We set thresholds of $SN > 3$ for the Pa α image and $SN > 10$ for the continuum image, and extract only pixels satisfying both conditions.

The spatially resolved SFR versus M_* plots obtained for each object is shown in Fig. 9.3. Here, we can clearly see a correlation between Σ_{SFR} and Σ_{M_*} . Even in the Σ_{SFR} and Σ_{M_*} plot, the “main-sequence track” can be seen in both galaxies. This indicates that the known correlation between SFR - M_* is kept even in surface density unit, i.e. Σ_{SFR} and Σ_{M_*} .

Furthermore, the both relations are offset upward from those of normal star-forming galaxies at $z \sim 0$ obtained from optical IFS observation (Cano-Díaz et al., 2016). The specific star formation rate for each pixel ($sSFR \equiv \Sigma_{SFR}/\Sigma_{M_*}$) shows higher value compared with those of the $z \sim 0$ galaxies not only in Pa α clumps (i.e. star-forming clumps) as seen in Fig. 9.1 but also in inter-clump regions. Fig. 9.4 plots the binned pixel with $0.''2$ sampling for both galaxies, and the tight correlations can be obtained which suggests Enhanced $sSFR$ throughout entire region can also be seen in Fig 9.5. The $sSFR$ for each pixel as a function of radius shows roughly constant value of $\sim 0.5 \text{ Gyr}^{-1}$ and $\sim 2.3 \text{ Gyr}^{-1}$ for NB209-097 and NB209-096 from a radius of 1 kpc to 4 kpc.



(a) NB209-096



(b) NB209-097

Fig. 9.3 Spatially resolved $\Sigma_{\text{SFR}}-\Sigma_{\text{M}^*}$. The black dashed line is taken from the resolved study of nearby normal star-forming galaxies by optical IFS survey (Cano-Díaz et al., 2016). Each pixel is color-coded with the value of radius which is the distance from a peak of continuum image.

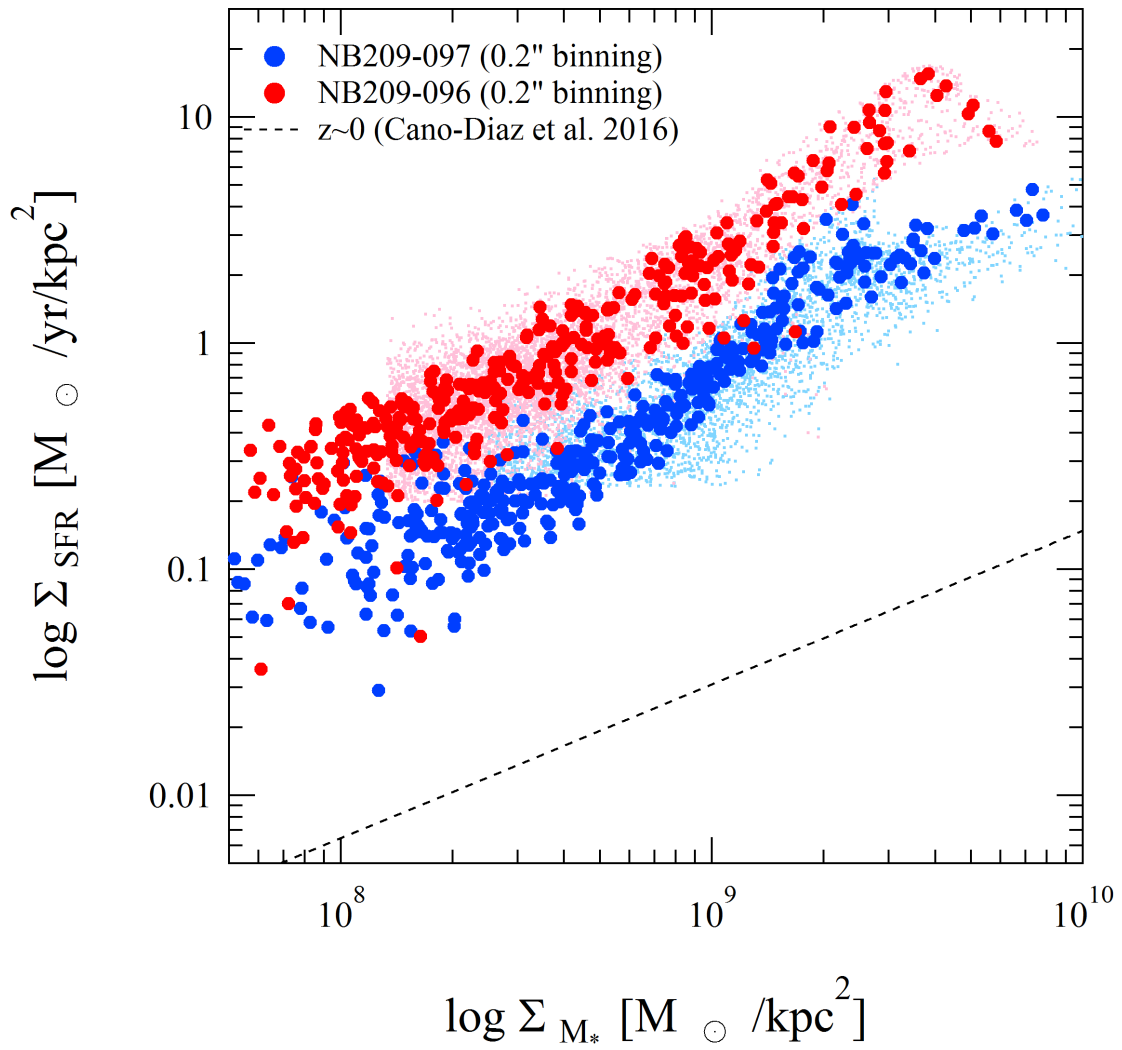
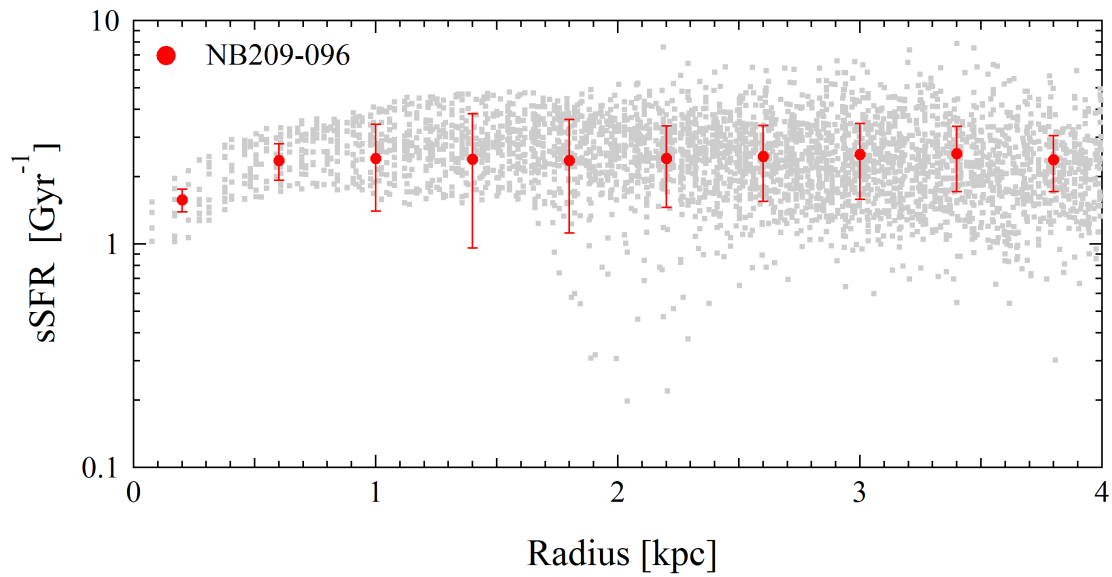
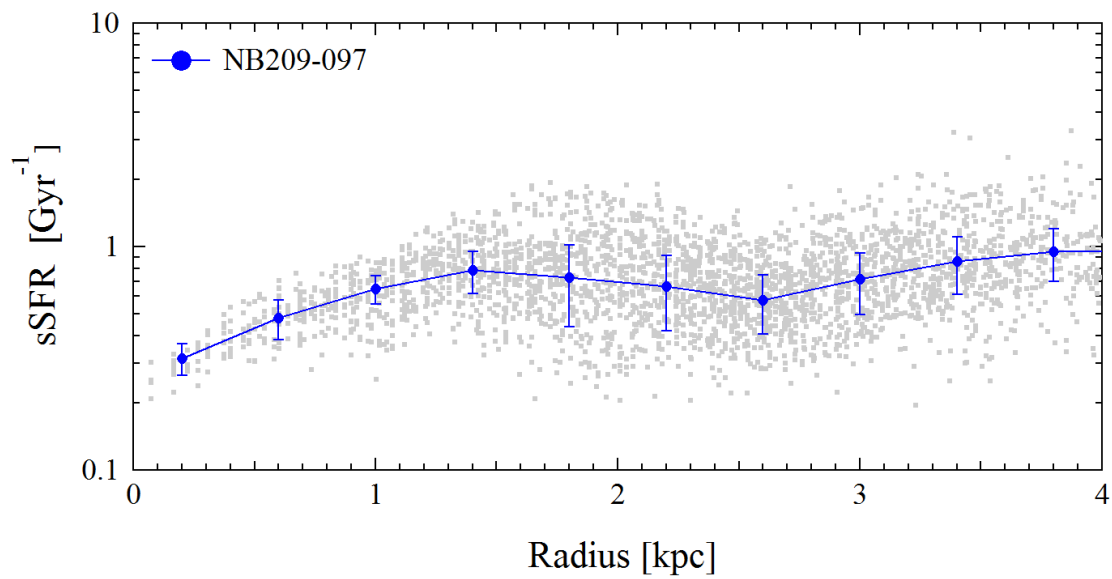


Fig. 9.4 Spatially resolved $\Sigma_{\text{SFR}}-\Sigma_{M_*}$ with $0.2''$ binning.



(a) NB209-096



(b) NB209-097

Fig. 9.5 Radial distribution of sSFR. The origin of the radius is defined as a peak of the continuum image. The definition of radius is same as Fig. 9.3.

9.2.3 Detection of Pa α clumps

We spatially resolve the interior of the two galaxies with 400 pc resolution and identify star-forming clumps in NB209-097 shown in the right panel of Fig. 9.1b. These star-forming clumps show Pa α luminosity of $\gtrsim 10^{40}$ erg/s have a higher specific star formation rate within the galaxy. We visually identify four clumps: the “core” located at the center of the galaxy and the “clump-A, B and C” embedded in the ring-shaped star formation region around the center. Two-dimensional gaussian fitting are performed for each clump to measure its size defining the peak of Pa α flux as the center of the clump. We define a clump diameter using a best fitting FWHM_x and FWHM_y as follows: $D_{\text{clump}} = \sqrt{(\text{FWHM}_x^2 + \text{FWHM}_y^2)}/2$.

Star formation rates and stellar masses of the clumps are measured with an aperture size of D_{clump} , and results are summarized in Table 9.2. The largest core has a size of ~ 900 pc, and also has the largest stellar mass, which is about 4 times larger than those of other clumps. The clump-A, B, and C, which are located at the same distance of ~ 1.5 kpc from the center of the galaxy, have diameters of 450–650 pc and SFRs of 0.5–1.3 M_{\odot}/yr . They mean that stellar mass surface densities (Σ_{M_*}) of the clump-A, B, and C are not as high as that of the core while all of the clumps have a similar star formation rate surface density (Σ_{SFR}) of $\sim 3\text{--}4 M_{\odot} \text{ yr}^{-1}$, in other words, the clump-A, B, and C have higher sSFRs than that of the core.

These features appear as difference of the location on the $\Sigma_{\text{SFR}}\text{--}\Sigma_{M_*}$ plane. Fig.9.6a shows that the core occupies the high-mass end of the “main sequence” of the NB209-097 while the other clumps are deviated from it and occupy almost the same position on the plot. The clump-A, B, and C have high sSFRs of 1.1–1.6 Gyr^{-1} , meaning that star formation activities of the clump-A, B, and C are enhanced. Since these clumps are close to the limit of the resolution of the observation (~ 400 pc), it is impossible to disassemble the internal structures of the clumps. Possibility that the high star formation rate of the Pa α clumps can be explained by accumulation of smaller star-forming regions is discussed in Chapter 10.

Table 9.2 Summary of SFR and stellar mass of Pa α clumps

Name	Distance [kpc]	D_{clump} [pc]	SFR [M_{\odot}/yr]	Σ_{SFR} [$M_{\odot}/\text{yr}/\text{kpc}^2$]	M_{*} [M_{\odot}/kpc^2]	$\Sigma_{M_{*}}$ [M_{\odot}/kpc^2]	sSFR [1/Gyr]
Core	~ 0.3	920 ± 30	2.3 ± 0.2 (6.9%) ^a	3.5 ± 0.4	$(5.9 \pm 0.3) \times 10^9$ (8.7%) ^b	$(8.9 \pm 0.7) \times 10^9$	0.39 ± 0.04
Clump-A	~ 1.7	650 ± 20	1.3 ± 0.1 (3.7%)	3.8 ± 0.4	$(7.9 \pm 0.1) \times 10^8$ (1.2%)	$(2.3 \pm 0.4) \times 10^9$	1.6 ± 0.3
Clump-B	~ 1.3	450 ± 40	0.48 ± 0.05 (1.4%)	3.1 ± 0.6	$(4.2 \pm 0.6) \times 10^8$ (0.6%)	$(2.7 \pm 0.6) \times 10^9$	$1.1 \sim 0.2$
Clump-C	~ 1.5	600 ± 40	0.74 ± 0.09 (2.2%)	2.7 ± 0.5	$(6.2 \pm 0.1) \times 10^8$ (0.9%)	$(2.2 \pm 0.5) \times 10^9$	$1.2 \sim 0.3$

^a Percentage to total star formation rate.^b Percentage to total mass.

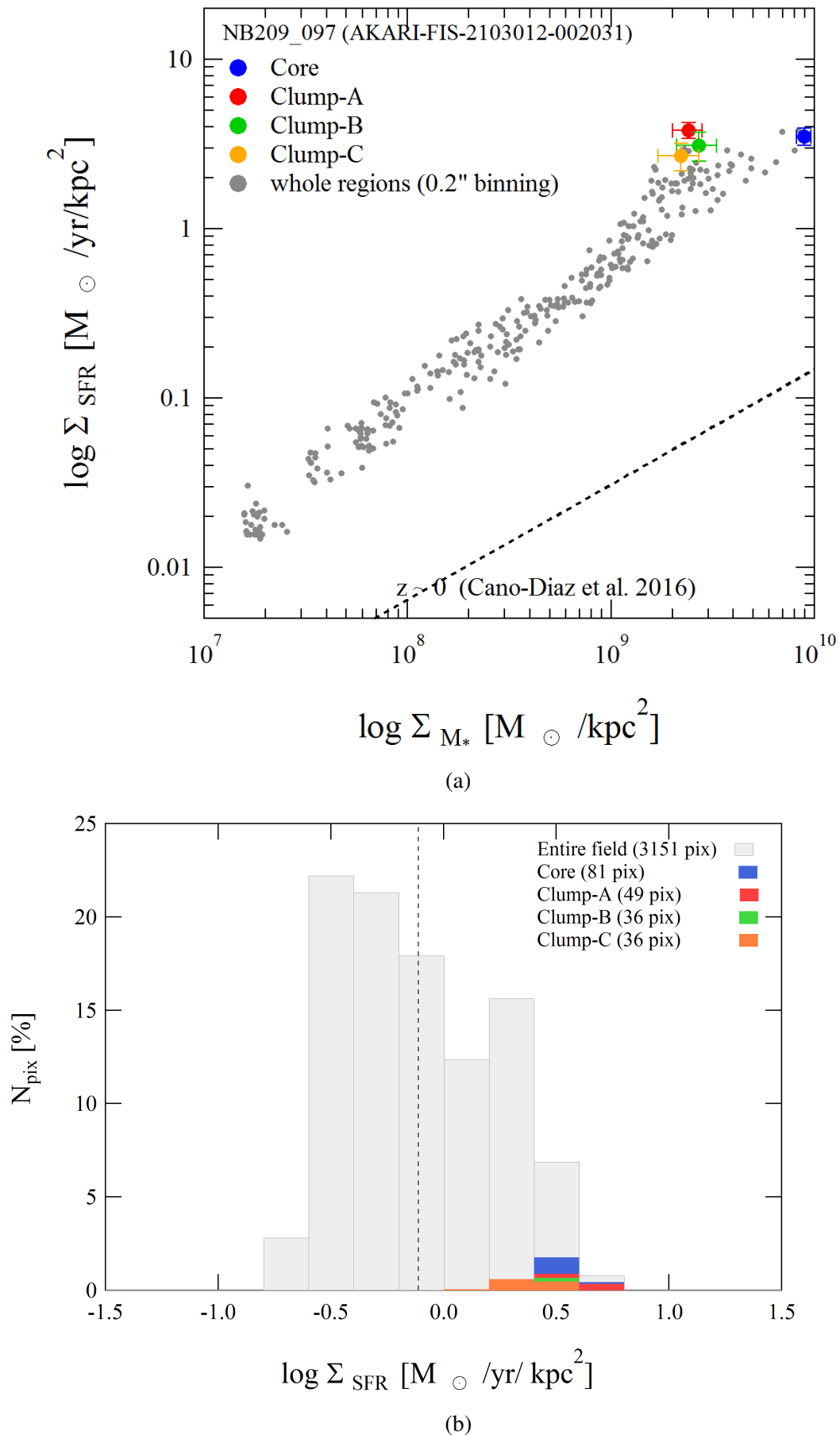


Fig. 9.6 (a) Pa α clumps in $\Sigma_{\text{SFR}}-\Sigma_{\text{M}^*}$ plane. (b) Distribution of Σ_{SFR} of Pa α clumps. The black dashed line indicates $-0.11 \text{ M}_{\odot}/\text{yr}/\text{kpc}^2$ which is the mean value of the whole galaxy.

Chapter 10

Discussion

10.1 Origin of Bursty Star Formation Activities

The galaxies we observe have large sSFR, deviating largely from the main sequence relation at $z \sim 0.1$ as shown in Fig 9.2. In addition, Fig. 9.4 indicates that star formation activities are enhanced not only for the integrated quantities but also in spatially-resolved surface density.

The large star formation surface densities suggest that a high gas surface densities in these galaxies. We recover gas properties by converting the star formation surface density into gas surface density using the Kennicutt-Schmidt law (Kennicutt, 1998b),

$$\Sigma_{\text{SFR}} = A \Sigma_{\text{gas}}^N \quad (10.1)$$

with $A = (2.5 \pm 0.7) \times 10^{-4}$ and $N = 1.40 \pm 0.15$ for circumnuclear starbursts. The gas mass properties derived from above equation are summarized in Table. 10.1. For both galaxies the gas mass surface densities (Σ_{gas}) show similar value of $\Sigma_{\text{gas}} \sim 200 \text{ M}_{\odot}/\text{pc}^2$. This value is comparable to those of high- z galaxies of $\Sigma_{\text{gas}} \sim 100\text{--}1000 \text{ M}_{\odot}/\text{pc}^2$ obtained from CO(3–2) survey of star-forming galaxies at $z \sim 1\text{--}3$ (Tacconi et al., 2013). In other words, higher gas density environment may be realized in these galaxies compared with those in nearby normal star-forming galaxies of $\Sigma_{\text{gas}} \sim 1\text{--}100 \text{ M}_{\odot}/\text{pc}^2$ (Kennicutt, 1998b). Also, $\tau_{\text{dep}} \sim 0.5 \text{ Gyr}$ indicates higher star formation activity in the galaxies while the nearby normal galaxies with $\log M_{*} = 10.4\text{--}11.4$ have $\sim 1\text{--}2 \text{ Gyr}$ (Bigiel et al., 2011). Such high gas density environment and star formation activity may have caused by a gas-inflow or compression of gas through merger event. We will discuss it from the viewpoint of merger stage in the following.

Table 10.1 Gas properties derived from KS-law

Name	$\Sigma_{\text{gas}}^{(a)}$ [M_{\odot}/pc^2]	$M_{\text{gas}}^{(b)}$ [M_{\odot}]	$f_{\text{gas}}^{(c)}$	$\tau_{\text{dep}}^{(d)}$ [Gyr]
NB209-096	170±100	$(6\pm3) \times 10^{10}$	0.5±0.2	0.5±0.3
NB209-097	190±100	$(2\pm1) \times 10^{10}$	0.2±0.1	0.5±0.3
Core	900±700	$(6\pm5) \times 10^8$	0.09±0.06	0.3±0.2
Clump-A	1000±700	$(3\pm2) \times 10^8$	0.3±0.2	0.3±0.2
Clump-B	800±600	$(1\pm1) \times 10^8$	0.2±0.1	0.3±0.2
Clump-C	800.0±600	$(2\pm2) \times 10^8$	0.3±0.1	0.3±0.2

^(a) Gas mass surface density derived by KS law.

^(b) The total gas mass is obtained by multiplying the Σ_{gas} by the area of the photometric aperture.

^(c) Gas fraction is defined as $f_{\text{gas}} = M_{\text{gas}}/(M_{\text{gas}} + M_{*})$.

^(d) Gas depletion time is defined as $\tau_{\text{dep}} = M_{\text{gas}}/SFR$.

NB209-096: mid-stage of a merger event

As shown in Fig. 8.2, this galaxy shows disturbed morphology with double core. We find an offset of 1 kpc between the peak of the continuum image and of the Pa α image in Fig 8.3a. One peak has sSFR similar to the integrated value of the galaxy, while the other enhanced. Such double cores have been reported in various merger system, which strongly support that NB209-096 is in the midst of a merger event. Thus, the star formation activity and high gas surface density of NB209-096 are considered to be the result of such a merger event. Through collision between galaxies, hydrodynamical simulations suggest that gas loses angular momentum due to dynamical friction, and as a result the gas quickly drops to the center of gravitational potential and fuel the kpc-scale starbursts (Barnes and Hernquist, 1998; Di Matteo et al., 2007).

NB209-097: early-stage of a merger event?

This galaxy seems to have a stable disk structure in the optical image (Fig. 8.2), and we detect clumpy active star-forming regions around the center thanks to sub-kpc spatial resolution (Fig. 9.6a). As described in Chapter 8 there is a companion about 20 kpc apart from the galaxy, which have same redshift and stellar mass ratio of 1/10. These facts suggest that NB209-097 and the companion may be at an early stage of a merger. As gravitational potential interfere with each other from the relatively large distance to a companion of 20 kpc (*e.g.* Bignone et al. (2017)), star formation may be induced. However, it is difficult to distinguish this scenario only by imaging observation data, and spatially resolved kinematic information by IFS observations is necessary, which may provide us information of velocity

field and velocity dispersion field (*i.e.* local turbulent component). It will provide us signs of gas inflow or disturbance of velocity field. They may be an important science target for an IFS follow-up observation in the future.

10.2 Star-forming clumps in Starbursts galaxies

A relationship between a size and a star formation rate (or luminosity) of a star-forming region is a useful tool for investigating their physical properties. Fig. 10.1 shows the size-SFR relation of the star-forming clumps detected by various SF tracers. Our samples of Pa α clumps have diameters ranging from 450 to 900 pc and star formation rates of 0.5–2.3 $M_{\odot} \text{ yr}^{-1}$. The star formation rates are nearly one order of magnitude higher than those of normal HII regions found in nearby spiral galaxies, and their star formation rate densities of $\sim 3\text{--}4 M_{\odot} \text{ yr}^{-1} \text{ kpc}^{-2}$ are also high compared with normal HII regions. This value is similar to those of star-forming regions detected by H β in nearby interacting systems (*e.g.* the Antenna galaxy; Bastian et al. (2006)).

Star-formation clumps in latest studies of nearby starburst galaxies are also plotted in Fig. 10.1. One is Fisher et al. (2017), which performs HST optical imaging with a high spatial resolution of 50–150 pc and resolve star-forming regions of starburst galaxies ($\text{SFR}(\text{H}\alpha) \sim 10\text{--}40$) at two redshift ranges of ~ 0.075 and ~ 0.13 . They use the H α line as a star formation tracer and select samples from SDSS, which leads to relatively less dust obscured targets with $A_v \sim 0\text{--}3$ mag. The other is Piqueras López et al. (2016), which uses VLT/SINFONI to perform a near-infrared IFS observation of dusty LIRGs with $A_v \sim 1\text{--}20$ selected from IRAS 24 μm sources. Although their observations are performed under a natural seeing condition, high spatial resolution (~ 200 pc) is realized by selecting a sample at smaller redshift ($z \sim 0.014$ for LIRGs). They detect star-forming regions of LIRGs with the Br γ line.

Our samples show good agreement with those in Fisher et al. (2017) and Piqueras López et al. (2016) on the size-SFR relationship. It seems that the change in the optical thickness due to the different star formation tracer of each study has no big influence on the results. These results suggest that a star-forming region found in a nearby starburst galaxy has different properties that realize a high star formation rate density compared to normal HII regions of nearby spiral galaxies. Note that dust extinction has been corrected in the previous studies, and the correlation seen in the SFR-size plane does not seem to change significantly depending on the dusty environment. On the other hand, we do not perform any dust-extinction correction, which means our SFR gives lower limit for each Pa α clump.

Our samples and previous studies of nearby starburst galaxies occupy a position close to the giant star-forming clumps at $z \sim 2$ in Fig. 10.1. This suggests that the Pa α clumps

found in NB209-097 are likely to be good analogs of giant star formation clumps at $z \sim 2$. Disk galaxies with such star-forming clumps have been discovered through $z \sim 1-3$ (Guo et al., 2015; Shibuya et al., 2016), and their formation mechanisms can be modeled by self-gravitational instability and fragmentation (*i.e.* the Toomre instability; Toomre (1964)) of a gaseous disk (Noguchi, 1999).

The diameters of clump-A, B, and C are 450–650 pc, which are close to the limit of resolution of our observation (~ 400 pc). This means that an internal structure of these clumps is not fully decomposed and we cannot exclude the possibility that their high star formation rate is a result from an aggregation of smaller star formation regions. According to Alonso-Herrero et al. (2002) which investigated star-forming regions of ULIRGs/LIRGs in the Pa α emission line using HST/NICMOS, most of the star-forming regions of ULIRGs/LIRGs are not aggregation of HII regions seen in nearby spiral galaxies, but rather tend to have larger sizes intrinsically. As shown in Fig. 10.1, many star-forming clumps with a diameter of 400-600 pc have been identified with a resolution of < 200 pc, and also been reported up to a diameter of 1000 pc (Fisher et al., 2017; Piqueras López et al., 2016). Our Pa α clumps have size and star formation rate similar to those of the previous studies, which indicates that our samples are likely to be a single star-forming region. However, in order to investigate an internal structure of star-forming region of a LIRGs at $z \sim 0.11$, it is necessary to wait for a next-generation facilities such as TMT, which has capability to realize a diffraction-limited observation in the near-infrared wavelength.

Table 10.1 summarizes the gas properties of each Pa α clump derived by the same method used in Section 9.1.2. Their gas mass surface density of 800–900 M_{\odot}/pc^2 is one or two order of magnitude greater than that of a typical HII region found in spiral arms of a nearby galaxy (Heyer et al., 2004), indicating that they have denser gas environment than typical star forming regions. In addition, gas fractions ($f_{\text{gas}} \equiv M_{\text{gas}} / (M_{*} + M_{\text{gas}})$) of clump-A, B, and C are estimated to be 0.2–0.3, which is comparable to those of clumpy galaxies at $z \sim 1-2$ of 0.2–0.8 (Bournaud and Elmegreen, 2009).

While the similarity of individual star-forming clump exists, the difference is also seen. Pa α clumps in NB209-097 are detected on the circumnuclear star forming rings, but high- z giant star-forming clumps are rather detected in a wide area of the disk. Also, our sample may be influenced by early stage of a merger event, although clumps at high- z are considered to be consequence of disk instability (Genzel et al., 2011). It is difficult to clarify the cause of these differences because information of gas motion is missing. Clumpy galaxies like NB209-097 may be further discovered in the PARADISES survey, and the origin of starbursts can be validated using near-infrared IFS observation by estimating turbulent gas motion.

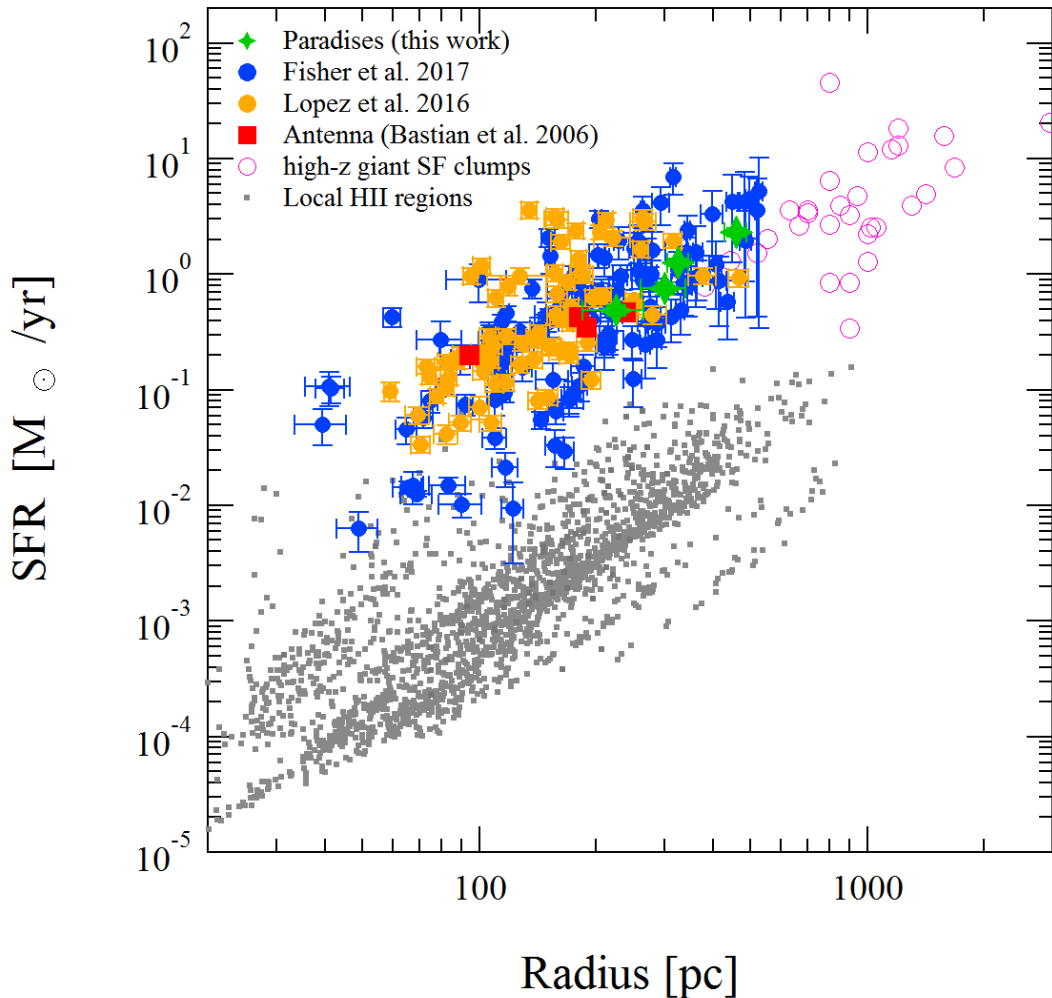


Fig. 10.1 Scaling relation between a size and a SFR of star-forming clumps. The green stars show the four star-forming regions detected NB209-097 using the Pa α line. The filled blue circle represents the star formation region detected in the 10 LIRGs at $z \sim 0.014$ using the Br γ line (Piqueras López et al., 2016). The filled orange circle represents the star formation region detected in the 10 starburst galaxies at $z = 0.075\text{--}0.13$ (Fisher et al., 2017) using the H α line. The sizes of these star-forming regions are determined by the definition described in Section 9.2.3 except Fisher et al. (2017), which employs the geometric mean for the size definition. The data of “Local HII region” is taken from SINGS (Kennicutt et al., 2003), Bordalo and Telles (2011), González Delgado et al. (1997), Terlevich and Melnick (1981), and Rozas et al. (2006). It also contains the HII regions of NGC4321 (Arsenault et al., 1990) and NGC4449 (Fuentes-Masip et al., 2000). The antenna galaxies (NGC4038/4039) is plotted as an example of nearby merger system (Bastian et al., 2006). The high- z samples are taken from Arcs (Jones et al., 2010), WiggleZ (Wisnioski et al., 2012), SINS (Genzel et al., 2011), and SHIZELS (Swinbank et al., 2012).

Chapter 11

Conclusion of the thesis

SWIMS-IFU is a new slicer-type IFU for the near-infrared spectrograph SWIMS, which is the 1st generation instrument of TAO 6.5-m telescope. It has wide field of view of $> 200 \square''$ at the TAO 6.5-m telescope and wide spectral coverage of 0.9–2.5 μm simultaneously. The module-like design of SWIMS-IFU enable us to quickly exchange observation modes between imaging, long-slit (or multi-slit) spectroscopy, and integral field spectroscopy. These capabilities will make an observation strategy more flexible, and realize efficient IFS survey in the near-infrared wavelength which is still rare, but already implemented in the optical wavelength (*e.g.* CALIFA, SAMI, and MaNGA). In Part I, we have developed SWIMS-IFU as follows :

- (1) We successfully obtain an optical layout solution satisfying the requirements of image quality as well as the volume limitation ($< 170 \text{ mm} \times 220 \text{ mm} \times 60 \text{ mm}$) by performing paraxial calculation and optimization. The optical design is optimized for seeing-limited condition and with wide field of view of $145 \square''$ and $220 \square''$ at the Subaru and TAO 6.5-m telescope, respectively, as well as wide spectral coverage of 0.9–2.5 μm . All the optical surfaces are packed into volume of $150 \text{ mm} \times 185 \text{ mm} \times 50 \text{ mm}$, respectively, and experimentally confirmed that the mask exchange unit can handle safely the dummy IFU with the same size and weight as the designed values. Optical performance shows that the worst spot diameter is $0.''39$ which is approximately equal to the IFU spatial sampling. Considering that SWIMS-IFU performs seeing-limited observation, this is within the allowable range .
- (2) We next perform a proof-of-principle experiment of fabrication of a slicing mirror array which is the heart of the IFU optics. Simultaneous control of two axes of the diamond end-mill tool results in surface roughness of 10 nm and shape error of 80 nm for NiP plated aluminum blocks. They satisfy the specifications required to achieve the IFU

throughput of 70% at $\lambda = 900$ nm. Since once we establish the processing method, it is easy to create many mirrors with the same figure and same quality. Thus, the results will have a big influence for development of multi-object IFUs that are being studied for next-generation instruments

- (3) Further we verify diamond cutting performance and conduct cryogenic shape measurements. Comprehensive study of various mirror materials shows surface roughness of ~ 5 nm can be achieved by diamond cutting, especially for aluminum coated with NiP, C1020, and RSA6061, and their surface roughness can be achieved $\lesssim 5$ nm and have few surface defects. In addition, we show that RSA443 is effective for suppressing bimetallic effect by measuring a surface shape at 80 K. These results indicate that the RSA443 coated with NiP is optimal as a material for the infrared metallic mirror used under cryogenic temperature in terms of both surface roughness and shape.

Technological challenges still remain for the development of an image slicer type IFUs in the near-infrared wavelength. Since once we establish the processing method, it is easy to create many mirrors with the same figure and same quality, thus the results obtained in this study will be useful for development of multi-object IFUs that are being studied for next-generation instruments.

In Part II we perform Pa α imaging at the resolution of $0.''2$ using Subaru/IRCS assisted by the AO188. We observe two starburst galaxies, one is a mid-stage merger NB209-096 and the other may be a early-stage merger NB209-097, and star-formation knots emitting in Pa α are detected clearly in both galaxies. The observational results are as follows:

- (4) We discover a strong correlation between the star formation rate surface density and the stellar mass surface density. This relationship is the near-infrared version of the $\Sigma_{\text{SFR}}-\Sigma_{M_*}$ relationship which have been reported by optical IFS observations, and we detected it in the starburst galaxies using the near-infrared Pa α line for the first time. Our relation shows an order of magnitude higher than those found in the local star-forming galaxies. We also find that star formation is enhanced not only in Pa α clumps but also throughout the galaxy.
- (5) NB209-096 is an interaction galaxy during merger with double core, one shows advanced stellar mass accumulation and the other has higher SFR than that of other region in the galaxy. NB209-097 may be at an early stage of merger event, and it shows circumnuclear star forming region. Bursty star formation activities in both galaxies may be induced through merger event, but in order to verify it, spatially resolved spectral information is needed in order to distinguish their internal gas motion, and this is future tasks for SWIMS-IFU.

- (6) We have identified four clumps in NB209-097 whose star formation rate surface density is $\Sigma_{\text{SFR}} \sim 3\text{--}4 \text{ M}_{\odot}/\text{yr}/\text{kpc}^2$, higher compared with those of HII regions in the nearby normal galaxies. They are similar to giant star forming clumps in clumpy galaxies at $z = 1\text{--}2$. From the gas surface density and gas fraction derived assuming the K-S law, these Pa α clumps may be a local analogs of those of $z = 1\text{--}2$ clumpy galaxies.

Clumpy galaxies like NB209-097 may be further discovered in the PARADISES survey, and the origin of starbursts can be validated using near-infrared IFS observation by measuring turbulent gas motion. Our study provides an interesting sample for future near-infrared IFS survey using SWIMS-IFU, and it is a good demonstration of spatially-resolved study with the Pa α emission line.

Acknowledgements

First of all, I would like to give deep appreciation to my supervisor, Associate Professor Kentaro Motohara from the University of Tokyo. He is one of the prominent researchers deeply understanding a wide range of fields from astronomical instruments to galactic astronomy. I am very proud of what I can study under such a wonderful leader. He always give me advice that flew meaningfully and suggestively.

I also sincerely thank the members of the SWIMS development team at the Institute of Astronomy (IoA), the University of Tokyo. Masahiro Konishi teach me various analysis methods using Python. Through his concrete advice, my research has been able to go beyond the great bar many times. Hidenori Takahashi is a professional in instrument development and I learn many experimental manners from him. Natsuko M. Kato make various support in helping me smoothly carry out my research. I also enjoy studying together for all the graduate students in the team. Ken Tateuchi, Soya Todo and Yutaka Kobayakawa left valuable assets in the development of SWIMS. Also I am able to share short, but valuable time with Yasunori Terao and Hirofumi Ohashi. I am convinced that they will play an important role in the first light of SWIMS at the Subaru telescope.

I have learned the techniques of optical design of an IFU using ZEMAX from Dr. Sinobu Ozaki from the National Astronomical Observatory of Japan. He is the leading expert in an IFU development in Japan, and the design of SWIMS-IFU has been successfully completed thanks to his training.

In the experiments of ultra-precision cutting, I am indebted to the member of the Ultrahigh Precision Optics Technology Team of RIKEN Center for Advanced Photonics (RCAP), RIKEN. D.Eng. Yutaka Yamagata, the PI of RCAP, and Prof. Shin-ya Morita from the Tokyo Denki University teach me a lot of basic knowledge and technique about an ultra-precision processing. Dr. Takuya Hosobata and Masahiro Takeda always answer politely to my repeated questions. M. Tamamitsu and Dr. K. Nakagawa propose a different interesting theme of using a slicing mirror and also provide a commitment to our experiment. Thanks to their cooperation, complicated processing on the slicing mirror can also be successful.

It is a valuable experience for me to observe using the Subaru telescope with Dr. Yusei Koyama, Dr. Ichi Tanaka, and Dr. Yosuke Minowa. They give me various advice on the

analysis of the AO data and the interpretation of the results. Thanks to their suggestive advice, I gain more interesting findings in the data.

I send a stimulating research life thanks to all the colleague at the IoA. Mitsuru Kokubo, Takuma Izumi, and Kazushi Okada are doing excellent research, and their works always inspire me.

I would like to express my appreciation to many researchers who give me various support and advice through my PhD. If this thesis plays some role in future astronomy, that is my greatest pleasure.

Part of the this work is supported by Grant-in-Aid for Japan Society for the Promotion of Science (JSPS) Research Fellow (266780), and the grant of Joint Development Research supported by the Research Coordination Committee, National Astronomical Observatory of Japan (NAOJ).

References

- Adam, G., Bacon, R., Courtes, G., Georgelin, Y., Monnet, G., and Pecontal, E. (1989). Observations of the Einstein Cross 2237+030 with the TIGER Integral Field Spectrograph. *A&A*, 208:L15–L18.
- Allington-Smith, J. (2006). Basic principles of integral field spectroscopy. *New A Rev.*, 50:244–251.
- Allington-Smith, J. and Content, R. (1998). Sampling and Background Subtraction in Fiber-Lenslet Integral Field Spectrographs. *PASP*, 110:1216–1234.
- Allington-Smith, J., Murray, G., Content, R., Dodsworth, G., Davies, R., Miller, B. W., Jorgensen, I., Hook, I., Crampton, D., and Murowinski, R. (2002). Integral Field Spectroscopy with the Gemini Multiobject Spectrograph. I. Design, Construction, and Testing. *PASP*, 114:892–912.
- Allington-Smith, J. R., Content, R., Dubbeldam, C. M., Robertson, D. J., and Preuss, W. (2006). New techniques for integral field spectroscopy - I. Design, construction and testing of the GNIRS IFU. *MNRAS*, 371:380–394.
- Alonso-Herrero, A., Rieke, G. H., Rieke, M. J., Colina, L., Pérez-González, P. G., and Ryder, S. D. (2006). Near-Infrared and Star-forming Properties of Local Luminous Infrared Galaxies. *ApJ*, 650:835–849.
- Alonso-Herrero, A., Rieke, G. H., Rieke, M. J., and Scoville, N. Z. (2002). Massive Star Formation in Luminous Infrared Galaxies: Giant H II Regions and Their Relation to Super-Star Clusters. *AJ*, 124:166–182.
- Armus, L., Mazzarella, J. M., Evans, A. S., Surace, J. A., Sanders, D. B., Iwasawa, K., Frayer, D. T., Howell, J. H., Chan, B., Petric, A., Vavilkin, T., Kim, D. C., Haan, S., Inami, H., Murphy, E. J., Appleton, P. N., Barnes, J. E., Bothun, G., Bridge, C. R., Charmandaris, V., Jensen, J. B., Kewley, L. J., Lord, S., Madore, B. F., Marshall, J. A., Melbourne, J. E., Rich, J., Satyapal, S., Schulz, B., Spoon, H. W. W., Sturm, E., U, V., Veilleux, S., and Xu, K. (2009). GOALS: The Great Observatories All-Sky LIRG Survey. *PASP*, 121:559–576.
- Arsenault, R., Roy, J.-R., and Boulesteix, J. (1990). Large-scale formation of massive stars in the spiral galaxy NGC 4321. *A&A*, 234:23–39.
- Bacon, R., Accardo, M., Adjali, L., Anwand, H., Bauer, S., Biswas, I., Blaizot, J., Boudon, D., Brau-Nogue, S., Brinchmann, J., Caillier, P., Caponi, L., Carollo, C. M., Contini, T., Couderc, P., Daguisé, E., Deiries, S., Delabre, B., Dreizler, S., Dubois, J., Dupieux, M., Dupuy, C., Emsellem, E., Fechner, T., Fleischmann, A., François, M., Gallou, G.,

- Gharsa, T., Glindemann, A., Gojak, D., Guiderdoni, B., Hansali, G., Hahn, T., Jarno, A., Kelz, A., Koehler, C., Kosmalski, J., Laurent, F., Le Floch, M., Lilly, S. J., Lizon, J.-L., Loupiau, M., Manescau, A., Monstein, C., Nicklas, H., Olaya, J.-C., Pares, L., Pasquini, L., Pécontal-Rousset, A., Pelló, R., Petit, C., Popow, E., Reiss, R., Remillieux, A., Renault, E., Roth, M., Rupprecht, G., Serre, D., Schaye, J., Soucail, G., Steinmetz, M., Streicher, O., Stuik, R., Valentin, H., Vernet, J., Weilbacher, P., Wisotzki, L., and Yerle, N. (2010). The MUSE second-generation VLT instrument. In *Ground-based and Airborne Instrumentation for Astronomy III*, volume 7735 of Proc. SPIE, page 773508.
- Barnes, J. E. and Hernquist, L. (1998). Transformations of Galaxies. II. Gasdynamics in Merging Disk Galaxies: Addendum. *ApJ*, 495:187–188.
- Bastian, N., Emsellem, E., Kissler-Patig, M., and Maraston, C. (2006). Young star cluster complexes in NGC 4038/39. Integral field spectroscopy using VIMOS-VLT. *A&A*, 445:471–483.
- Beaucamp, A., Freeman, R., Morton, R., Ponudurai, K., and Walker, D. D. (2008). Removal of diamond-turning signatures on x-ray mandrels and metal optics by fluid-jet polishing. In *Advanced Optical and Mechanical Technologies in Telescopes and Instrumentation*, volume 7018 of Proc. SPIE, page 701835.
- Benn, C., Talbot, G., and Bacon, R. (2003). OASIS at the WHT. *The Newsletter of the Isaac Newton Group of Telescopes*, 7:21.
- Bigiel, F., Leroy, A. K., Walter, F., Brinks, E., de Blok, W. J. G., Kramer, C., Rix, H. W., Schrubba, A., Schuster, K.-F., Usero, A., and Wiese Meyer, H. W. (2011). A Constant Molecular Gas Depletion Time in Nearby Disk Galaxies. *ApJ*, 730:L13.
- Bignone, L. A., Tissera, P. B., Sillero, E., Pedrosa, S. E., Pellizza, L. J., and Lambas, D. G. (2017). Non-parametric morphologies of mergers in the Illustris simulation. *MNRAS*, 465:1106–1122.
- Bordalo, V. and Telles, E. (2011). The L- σ Relation of Local H II Galaxies. *ApJ*, 735:52.
- Bournaud, F. and Elmegreen, B. G. (2009). Unstable Disks at High Redshift: Evidence for Smooth Accretion in Galaxy Formation. *ApJ*, 694:L158–L161.
- Bruzual, G. and Charlot, S. (2003). Stellar population synthesis at the resolution of 2003. *MNRAS*, 344:1000–1028.
- Bryant, J. J., Owers, M. S., Robotham, A. S. G., Croom, S. M., Driver, S. P., Drinkwater, M. J., Lorente, N. P. F., Cortese, L., Scott, N., Colless, M., Schaefer, A., Taylor, E. N., Konstantopoulos, I. S., Allen, J. T., Baldry, I., Barnes, L., Bauer, A. E., Bland-Hawthorn, J., Bloom, J. V., Brooks, A. M., Brough, S., Cecil, G., Couch, W., Croton, D., Davies, R., Ellis, S., Fogarty, L. M. R., Foster, C., Glazebrook, K., Goodwin, M., Green, A., Gunawardhana, M. L., Hampton, E., Ho, I.-T., Hopkins, A. M., Kewley, L., Lawrence, J. S., Leon-Saval, S. G., Leslie, S., McElroy, R., Lewis, G., Liske, J., López-Sánchez, Á. R., Mahajan, S., Medling, A. M., Metcalfe, N., Meyer, M., Mould, J., Obreschkow, D., O’Toole, S., Pracy, M., Richards, S. N., Shanks, T., Sharp, R., Sweet, S. M., Thomas, A. D., Tonini, C., and Walcher, C. J. (2015). The SAMI Galaxy Survey: instrument specification and target selection. *MNRAS*, 447:2857–2879.

- Bundy, K., Bershad, M. A., Law, D. R., Yan, R., Drory, N., MacDonald, N., Wake, D. A., Cherinka, B., Sánchez-Gallego, J. R., Weijmans, A.-M., Thomas, D., Tremonti, C., Masters, K., Coccatto, L., Diamond-Stanic, A. M., Aragón-Salamanca, A., Avila-Reese, V., Badenes, C., Falcón-Barroso, J., Belfiore, F., Bizyaev, D., Blanc, G. A., Bland-Hawthorn, J., Blanton, M. R., Brownstein, J. R., Byler, N., Cappellari, M., Conroy, C., Dutton, A. A., Emsellem, E., Etherington, J., Frinchaboy, P. M., Fu, H., Gunn, J. E., Harding, P., Johnston, E. J., Kauffmann, G., Kinemuchi, K., Klaene, M. A., Knapen, J. H., Leauthaud, A., Li, C., Lin, L., Maiolino, R., Malanushenko, V., Malanushenko, E., Mao, S., Maraston, C., McDermid, R. M., Merrifield, M. R., Nichol, R. C., Oravetz, D., Pan, K., Parejko, J. K., Sanchez, S. F., Schlegel, D., Simmons, A., Steele, O., Steinmetz, M., Thanjavur, K., Thompson, B. A., Tinker, J. L., van den Bosch, R. C. E., Westfall, K. B., Wilkinson, D., Wright, S., Xiao, T., and Zhang, K. (2015). Overview of the SDSS-IV MaNGA Survey: Mapping nearby Galaxies at Apache Point Observatory. *ApJ*, 798:7.
- Calzetti, D. (2013). *Star Formation Rate Indicators*, page 419.
- Calzetti, D., Kennicutt, R. C., Engelbracht, C. W., Leitherer, C., Draine, B. T., Kewley, L., Moustakas, J., Sosey, M., Dale, D. A., Gordon, K. D., Helou, G. X., Hollenbach, D. J., Armus, L., Bendo, G., Bot, C., Buckalew, B., Jarrett, T., Li, A., Meyer, M., Murphy, E. J., Prescott, M., Regan, M. W., Rieke, G. H., Roussel, H., Sheth, K., Smith, J. D. T., Thornley, M. D., and Walter, F. (2007). The Calibration of Mid-Infrared Star Formation Rate Indicators. *ApJ*, 666:870–895.
- Cano-Díaz, M., Sánchez, S. F., Zibetti, S., Ascasibar, Y., Bland-Hawthorn, J., Ziegler, B., González Delgado, R. M., Walcher, C. J., García-Benito, R., Mast, D., Mendoza-Pérez, M. A., Falcón-Barroso, J., Galbany, L., Husemann, B., Kehrig, C., Marino, R. A., Sánchez-Blázquez, P., López-Cobá, C., López-Sánchez, Á. R., and Vilchez, J. M. (2016). Spatially Resolved Star Formation Main Sequence of Galaxies in the CALIFA Survey. *ApJ*, 821:L26.
- Cappellari, M., Emsellem, E., Krajnović, D., McDermid, R. M., Scott, N., Verdoes Kleijn, G. A., Young, L. M., Alatalo, K., Bacon, R., Blitz, L., Bois, M., Bournaud, F., Bureau, M., Davies, R. L., Davis, T. A., de Zeeuw, P. T., Duc, P.-A., Khochfar, S., Kuntschner, H., Lablanche, P.-Y., Morganti, R., Naab, T., Oosterloo, T., Sarzi, M., Serra, P., and Weijmans, A.-M. (2011). The ATLAS^{3D} project - I. A volume-limited sample of 260 nearby early-type galaxies: science goals and selection criteria. *MNRAS*, 413:813–836.
- Chabrier, G. (2003). Galactic Stellar and Substellar Initial Mass Function. *PASP*, 115:763–795.
- Content, R. (1997). New design for integral field spectroscopy with 8-m telescopes. In Ardeberg, A. L., editor, *Optical Telescopes of Today and Tomorrow*, volume 2871 of Proc. SPIE, pages 1295–1305.
- Cortese, L., Fogarty, L. M. R., Bekki, K., van de Sande, J., Couch, W., Catinella, B., Colless, M., Obreschkow, D., Taranu, D., Tescari, E., Barat, D., Bland-Hawthorn, J., Bloom, J., Bryant, J. J., Cluver, M., Croom, S. M., Drinkwater, M. J., d'Eugenio, F., Konstantopoulos, I. S., Lopez-Sanchez, A., Mahajan, S., Scott, N., Tonini, C., Wong, O. I., Allen, J. T., Brough, S., Goodwin, M., Green, A. W., Ho, I.-T., Kelvin, L. S., Lawrence, J. S., Lorente, N. P. F., Medling, A. M., Owers, M. S., Richards, S., Sharp, R., and Sweet, S. M. (2016).

- The SAMI Galaxy Survey: the link between angular momentum and optical morphology. *MNRAS*, 463:170–184.
- Cresci, G., Hicks, E. K. S., Genzel, R., Schreiber, N. M. F., Davies, R., Bouché, N., Buschkamp, P., Genel, S., Shapiro, K., Tacconi, L., Sommer-Larsen, J., Burkert, A., Eisenhauer, F., Gerhard, O., Lutz, D., Naab, T., Sternberg, A., Cimatti, A., Daddi, E., Erb, D. K., Kurk, J., Lilly, S. L., Renzini, A., Shapley, A., Steidel, C. C., and Caputi, K. (2009). The SINS Survey: Modeling the Dynamics of $z \sim 2$ Galaxies and the High- z Tully-Fisher Relation. *ApJ*, 697:115–132.
- Daddi, E., Dickinson, M., Morrison, G., Chary, R., Cimatti, A., Elbaz, D., Frayer, D., Renzini, A., Pope, A., Alexander, D. M., Bauer, F. E., Giavalisco, M., Huynh, M., Kurk, J., and Mignoli, M. (2007). Multiwavelength Study of Massive Galaxies at $z \sim 2$. I. Star Formation and Galaxy Growth. *ApJ*, 670:156–172.
- de Zeeuw, P. T., Allington-Smith, J. R., Bacon, R., Bureau, M., Carollo, C. M., Copin, Y., Davies, R. L., Emsellem, E., Kuntschner, H., Miller, B. W., Monnet, G., Peletier, R. F., and Verolme, E. K. (2000). The One Eye that Sees All: Integral Field Spectroscopy with SAURON on the WHT. *The Newsletter of the Isaac Newton Group of Telescopes*, 2:11–15.
- Delgado-Serrano, R., Hammer, F., Yang, Y. B., Puech, M., Flores, H., and Rodrigues, M. (2010). How was the Hubble sequence 6 Gyr ago? *A&A*, 509:A78.
- DeWitt, C., Eikenberry, S., Cuevas Cardona, S., Chapa, O., Espejo, C., Keiman, C., and Sanchez, B. (2008). Cryogenic tests of bimetallic diamond-turned mirrors for the FRIDA integral field unit. In *Ground-based and Airborne Instrumentation for Astronomy II*, volume 7014 of Proc. SPIE, page 70142X.
- Di Matteo, P., Combes, F., Melchior, A.-L., and Semelin, B. (2007). Star formation efficiency in galaxy interactions and mergers: a statistical study. *A&A*, 468:61–81.
- Díaz-Santos, T., Alonso-Herrero, A., Colina, L., Packham, C., Radomski, J. T., and Telesco, C. M. (2008). Understanding the $8 \mu\text{m}$ versus Pa α Relationship on Subarcsecond Scales in Luminous Infrared Galaxies. *ApJ*, 685:211–224.
- Dopita, M., Hart, J., McGregor, P., Oates, P., Bloxham, G., and Jones, D. (2007). The Wide Field Spectrograph (WiFeS). *Ap&SS*, 310:255–268.
- Dubbeldam, C. M. (2006). Design and construction of the GNIRS IFU. *New A Rev.*, 50:342–345.
- Dubbeldam, C. M., Clark, P., Content, R., Kirby, A. K., Parkin, K., Robertson, D. J., Rolt, S., Ryder, D. A., and Sharples, R. M. (2012). The KMOS Integral Field System: fabrication, alignment, and test of 1000+ optical surfaces. In *Modern Technologies in Space- and Ground-based Telescopes and Instrumentation II*, volume 8450 of Proc. SPIE, page 84501M.
- Dubbeldam, C. M., Robertson, D. J., and Preuss, W. (2004). Freeform diamond machining of complex monolithic metal optics for integral field systems. In Atad-Ettedgui, E. and Dierickx, P., editors, *Optical Fabrication, Metrology, and Material Advancements for Telescopes*, volume 5494 of Proc. SPIE, pages 163–175.

- Eikenberry, S. S., Elston, R., Guzman, R., Julian, J., Raines, S. N., Gruel, N., Boreman, G., Glenn, P. E., Hull-Allen, C. G., Hoffman, J., Rodgers, M., Thompson, K., Flint, S., Comstock, L., and Myrick, B. (2004). FISICA: the Florida image slicer for infrared cosmology and astrophysics. In Moorwood, A. F. M. and Iye, M., editors, *Ground-based Instrumentation for Astronomy*, volume 5492 of Proc. SPIE, pages 1264–1273.
- Eisenhauer, F., Abuter, R., Bickert, K., Biancat-Marchet, F., Bonnet, H., Brynnel, J., Conzelmann, R. D., Delabre, B., Donaldson, R., Farinato, J., Fedrigo, E., Genzel, R., Hubin, N. N., Iserlohe, C., Kasper, M. E., Kissler-Patig, M., Monnet, G. J., Roehrl, C., Schreiber, J., Stroebele, S., Tecza, M., Thatte, N. A., and Weisz, H. (2003). SINFONI - Integral field spectroscopy at 50 milli-arcsecond resolution with the ESO VLT. In Iye, M. and Moorwood, A. F. M., editors, *Instrument Design and Performance for Optical/Infrared Ground-based Telescopes*, volume 4841 of Proc. SPIE, pages 1548–1561.
- Eisenhauer, F. and Raab, W. (2015). Visible/Infrared Imaging Spectroscopy and Energy-Resolving Detectors. *ARA&A*, 53:155–197.
- Elbaz, D., Dickinson, M., Hwang, H. S., Díaz-Santos, T., Magdis, G., Magnelli, B., Le Borgne, D., Galliano, F., Pannella, M., Chanial, P., Armus, L., Charmandaris, V., Daddi, E., Aussel, H., Popesso, P., Kartaltepe, J., Altieri, B., Valtchanov, I., Coia, D., Dannerbauer, H., Dasyra, K., Leiton, R., Mazzarella, J., Alexander, D. M., Buat, V., Burgarella, D., Chary, R.-R., Gilli, R., Ivison, R. J., Juneau, S., Le Floc'h, E., Lutz, D., Morrison, G. E., Mullaney, J. R., Murphy, E., Pope, A., Scott, D., Brodwin, M., Calzetti, D., Cesarsky, C., Charlot, S., Dole, H., Eisenhardt, P., Ferguson, H. C., Förster Schreiber, N., Frayer, D., Giavalisco, M., Huynh, M., Koekemoer, A. M., Papovich, C., Reddy, N., Surace, C., Teplitz, H., Yun, M. S., and Wilson, G. (2011). GOODS-Herschel: an infrared main sequence for star-forming galaxies. *A&A*, 533:A119.
- Elmegreen, D. M., Elmegreen, B. G., Marcus, M. T., Shahinyan, K., Yau, A., and Petersen, M. (2009). Clumpy Galaxies in Goods and Gems: Massive Analogs of Local Dwarf Irregulars. *ApJ*, 701:306–329.
- Fisher, D. B., Glazebrook, K., Damjanov, I., Abraham, R. G., Obreschkow, D., Wisnioski, E., Bassett, R., Green, A., and McGregor, P. (2017). DYNAMO-HST survey: clumps in nearby massive turbulent discs and the effects of clump clustering on kiloparsec scale measurements of clumps. *MNRAS*, 464:491–507.
- Förster Schreiber, N. M., Genzel, R., Bouché, N., Cresci, G., Davies, R., Buschkamp, P., Shapiro, K., Tacconi, L. J., Hicks, E. K. S., Genel, S., Shapley, A. E., Erb, D. K., Steidel, C. C., Lutz, D., Eisenhauer, F., Gillessen, S., Sternberg, A., Renzini, A., Cimatti, A., Daddi, E., Kurk, J., Lilly, S., Kong, X., Lehnert, M. D., Nesvadba, N., Verma, A., McCracken, H., Arimoto, N., Mignoli, M., and Onodera, M. (2009). The SINS Survey: SINFONI Integral Field Spectroscopy of $z \sim 2$ Star-forming Galaxies. *ApJ*, 706:1364–1428.
- Förster Schreiber, N. M., Genzel, R., Lehnert, M. D., Bouché, N., Verma, A., Erb, D. K., Shapley, A. E., Steidel, C. C., Davies, R., Lutz, D., Nesvadba, N., Tacconi, L. J., Eisenhauer, F., Abuter, R., Gilbert, A., Gillessen, S., and Sternberg, A. (2006). SINFONI Integral Field Spectroscopy of $z \sim 2$ UV-selected Galaxies: Rotation Curves and Dynamical Evolution. *ApJ*, 645:1062–1075.

- Fuentes-Masip, O., Muñoz-Tuñón, C., Castañeda, H. O., and Tenorio-Tagle, G. (2000). On the Size and Luminosity versus Velocity Dispersion Correlations from the Giant H II Regions in the Irregular Galaxy NGC 4449. *AJ*, 120:752–762.
- Genzel, R., Newman, S., Jones, T., Förster Schreiber, N. M., Shapiro, K., Genel, S., Lilly, S. J., Renzini, A., Tacconi, L. J., Bouché, N., Burkert, A., Cresci, G., Buschkamp, P., Carollo, C. M., Ceverino, D., Davies, R., Dekel, A., Eisenhauer, F., Hicks, E., Kurk, J., Lutz, D., Mancini, C., Naab, T., Peng, Y., Sternberg, A., Vergani, D., and Zamorani, G. (2011). The Sins Survey of $z \sim 2$ Galaxy Kinematics: Properties of the Giant Star-forming Clumps. *ApJ*, 733:101.
- Glazebrook, K. (2013). The Dawes Review 1: Kinematic Studies of Star-Forming Galaxies Across Cosmic Time. *PASA*, 30:e056.
- González Delgado, R. M., Pérez, E., Cid Fernandes, R., García-Benito, R., de Amorim, A. L., Sánchez, S. F., Husemann, B., Cortijo-Ferrero, C., López Fernández, R., Sánchez-Blázquez, P., Bekeraite, S., Walcher, C. J., Falcón-Barroso, J., Gallazzi, A., van de Ven, G., Alves, J., Bland-Hawthorn, J., Kennicutt, R. C., Kupko, D., Lyubenova, M., Mast, D., Mollá, M., Marino, R. A., Quirrenbach, A., Vílchez, J. M., and Wisotzki, L. (2014). The star formation history of CALIFA galaxies: Radial structures. *A&A*, 562:A47.
- González Delgado, R. M., Pérez, E., Tadhunter, C., Vilchez, J. M., and José Miguel Rodríguez-Espinosa, a. (1997). H II Region Population in a Sample of Nearby Galaxies with Nuclear Activity. I. Data and General Results. *ApJS*, 108:155–198.
- Goto, T., Arnouts, S., Inami, H., Matsuhara, H., Pearson, C., Takeuchi, T. T., Le Floch, E., Takagi, T., Wada, T., Nakagawa, T., Oyabu, S., Ishihara, D., Mok Lee, H., Jeong, W.-S., Yamauchi, C., Serjeant, S., Sedgwick, C., and Treister, E. (2011). Luminosity functions of local infrared galaxies with AKARI: implications for the cosmic star formation history and AGN evolution. *MNRAS*, 410:573–584.
- Goto, T., Takagi, T., Matsuhara, H., Takeuchi, T. T., Pearson, C., Wada, T., Nakagawa, T., Ilbert, O., Le Floch, E., Oyabu, S., Ohya, Y., Malkan, M., Lee, H. M., Lee, M. G., Inami, H., Hwang, N., Hanami, H., Im, M., Imai, K., Ishigaki, T., Serjeant, S., and Shim, H. (2010). Evolution of infrared luminosity functions of galaxies in the AKARI NEP-deep field. Revealing the cosmic star formation history hidden by dust. *A&A*, 514:A6.
- Guo, Y., Ferguson, H. C., Bell, E. F., Koo, D. C., Conselice, C. J., Giavalisco, M., Kassin, S., Lu, Y., Lucas, R., Mandelker, N., McIntosh, D. M., Primack, J. R., Ravindranath, S., Barro, G., Ceverino, D., Dekel, A., Faber, S. M., Fang, J. J., Koekemoer, A. M., Noeske, K., Rafelski, M., and Straughn, A. (2015). Clumpy Galaxies in CANDELS. I. The Definition of UV Clumps and the Fraction of Clumpy Galaxies at $0.5 < z < 3$. *ApJ*, 800:39.
- Heyer, M. H., Corbelli, E., Schneider, S. E., and Young, J. S. (2004). The Molecular Gas Distribution and Schmidt Law in M33. *ApJ*, 602:723–729.
- Hibbard, D. L. (1997). Electroless nickel for optical applications. In Ealey, M. A., Paquin, R. A., and Parsonage, T. B., editors, *Advanced Materials for Optics and Precision Structures*, Proc. SPIE, pages 179–205.

- Hill, G. J., MacQueen, P. J., Smith, M. P., Tufts, J. R., Roth, M. M., Kelz, A., Adams, J. J., Drory, N., Grupp, F., Barnes, S. I., Blanc, G. A., Murphy, J. D., Altmann, W., Wesley, G. L., Segura, P. R., Good, J. M., Booth, J. A., Bauer, S.-M., Popow, E., Goertz, J. A., Edmonston, R. D., and Wilkinson, C. P. (2008). Design, construction, and performance of VIRUS-P: the prototype of a highly replicated integral-field spectrograph for HET. In *Ground-based and Airborne Instrumentation for Astronomy II*, volume 7014 of Proc. SPIE, page 701470.
- Hopkins, A. M. and Beacom, J. F. (2006). On the Normalization of the Cosmic Star Formation History. *ApJ*, 651:142–154.
- Hummer, D. G. and Storey, P. J. (1987). Recombination-line intensities for hydrogenic ions. I - Case B calculations for H I and He II. *MNRAS*, 224:801–820.
- Jedamzik, R., Kunisch, C., Nieder, J., Weber, P., and Westerhoff, T. (2016). Progress on glass ceramic ZERODUR enabling nanometer precision. In *Society of Photo-Optical Instrumentation Engineers (SPIE) Conference Series*, volume 9780 of Proc. SPIE, page 97801K.
- Jedamzik, R., Kunisch, C., Nieder, J., and Westerhoff, T. (2014). Glass ceramic ZERODUR enabling nanometer precision. In *Optical Microlithography XXVII*, volume 9052 of Proc. SPIE, page 90522I.
- Jones, G. S. (1890). How a Telescope Mirror is Ground, Polished and Figured. *Sidereal Messenger*, vol. 9, pp.353-363, 9:353–363.
- Jones, T., Ellis, R. S., Richard, J., and Jullo, E. (2013). The Origin and Evolution of Metallicity Gradients: Probing the Mode of Mass Assembly at $z \sim 2$. *ApJ*, 765:48.
- Jones, T. A., Swinbank, A. M., Ellis, R. S., Richard, J., and Stark, D. P. (2010). Resolved spectroscopy of gravitationally lensed galaxies: recovering coherent velocity fields in subluminal $z \sim 2$ -3 galaxies. *MNRAS*, 404:1247–1262.
- Kaneda, H., Onaka, T., Kawada, M., and Murakami, H. (2003). Cryogenic optical testing of sandwich-type silicon carbide mirrors. *Appl. Opt.*, 42(4):708–714.
- Kannan, R., Stinson, G. S., Macciò, A. V., Brook, C., Weinmann, S. M., Wadsley, J., and Couchman, H. M. P. (2014). The MaGICC volume: reproducing statistical properties of high-redshift galaxies. *MNRAS*, 437:3529–3539.
- Katsianis, A., Tescari, E., and Wyithe, J. S. B. (2016). The Relation between Star-Formation Rate and Stellar Mass of Galaxies at $z \sim 1$ -4. *PASA*, 33:e029.
- Kennicutt, R. C. and Evans, N. J. (2012). Star Formation in the Milky Way and Nearby Galaxies. *ARA&A*, 50:531–608.
- Kennicutt, Jr., R. C. (1998a). Star Formation in Galaxies Along the Hubble Sequence. *ARA&A*, 36:189–232.
- Kennicutt, Jr., R. C. (1998b). The Global Schmidt Law in Star-forming Galaxies. *ApJ*, 498:541–552.

- Kennicutt, Jr., R. C., Armus, L., Bendo, G., Calzetti, D., Dale, D. A., Draine, B. T., Engelbracht, C. W., Gordon, K. D., Grauer, A. D., Helou, G., Hollenbach, D. J., Jarrett, T. H., Kewley, L. J., Leitherer, C., Li, A., Malhotra, S., Regan, M. W., Rieke, G. H., Rieke, M. J., Roussel, H., Smith, J.-D. T., Thornley, M. D., and Walter, F. (2003). SINGS: The SIRTf Nearby Galaxies Survey. *PASP*, 115:928–952.
- Kennicutt, Jr., R. C., Hao, C.-N., Calzetti, D., Moustakas, J., Dale, D. A., Bendo, G., Engelbracht, C. W., Johnson, B. D., and Lee, J. C. (2009). Dust-corrected Star Formation Rates of Galaxies. I. Combinations of H α and Infrared Tracers. *ApJ*, 703:1672–1695.
- Kinast, J., Hilpert, E., Lange, N., Gebhardt, A., Rohloff, R.-R., Risse, S., Eberhardt, R., and Tünnermann, A. (2014). Minimizing the bimetallic bending for cryogenic metal optics based on electroless nickel. In *Advances in Optical and Mechanical Technologies for Telescopes and Instrumentation*, volume 9151 of Proc. SPIE, page 915136.
- Kitagawa, Y., Ozaki, S., Motohara, K., Konishi, M., Takahashi, H., Tateuchi, K., Todo, S., Kato, N., and Yoshikawa, T. (2014). Concept and optical design of the near-infrared integral field unit for SWIMS. In *Advances in Optical and Mechanical Technologies for Telescopes and Instrumentation*, volume 9151 of Proc. SPIE, page 91514P.
- Kitagawa, Y., Yamagata, Y., Morita, S.-y., Motohara, K., Ozaki, S., Takahashi, H., Konishi, M., Kato, N. M., Kobayakawa, Y., Terao, Y., and Ohashi, H. (2016). Fabrication of a wide-field NIR integral field unit for SWIMS using ultra-precision cutting. In *Society of Photo-Optical Instrumentation Engineers (SPIE) Conference Series*, volume 9912 of Proc. SPIE, page 991225.
- Kobayashi, N., Tokunaga, A. T., Terada, H., Goto, M., Weber, M., Potter, R., Onaka, P. M., Ching, G. K., Young, T. T., Fletcher, K., Neil, D., Robertson, L., Cook, D., Imanishi, M., and Warren, D. W. (2000). IRCS: infrared camera and spectrograph for the Subaru Telescope. In Iye, M. and Moorwood, A. F., editors, *Optical and IR Telescope Instrumentation and Detectors*, volume 4008 of Proc. SPIE, pages 1056–1066.
- Komatsu, E., Smith, K. M., Dunkley, J., Bennett, C. L., Gold, B., Hinshaw, G., Jarosik, N., Larson, D., Nolte, M. R., Page, L., Spergel, D. N., Halpern, M., Hill, R. S., Kogut, A., Limon, M., Meyer, S. S., Odegard, N., Tucker, G. S., Weiland, J. L., Wollack, E., and Wright, E. L. (2011). Seven-year Wilkinson Microwave Anisotropy Probe (WMAP) Observations: Cosmological Interpretation. *ApJS*, 192:18.
- Konishi, M., Motohara, K., Takahashi, H., Tateuchi, K., Kitagawa, Y., Kato, N., Aoki, T., Doi, M., Handa, T., Kamizuka, T., Kawara, K., Kohno, K., Koshida, S., Minezaki, T., Miyata, T., Morokuma, T., Sako, S., Soyano, T., Tamura, Y., Tanabe, T., Tanaka, M., Tarusawa, K., and Yoshii, Y. (2012). Design and development of SWIMS: a near-infrared multi-object spectrograph for the University of Tokyo Atacama Observatory. In *Ground-based and Airborne Instrumentation for Astronomy IV*, volume 8446 of Proc. SPIE, page 84467P.
- Konishi, M., Motohara, K., Tateuchi, K., Takahashi, H., Kitagawa, Y., Kato, N., Sako, S., Uchimoto, Y. K., Toshikawa, K., Ohsawa, R., Yamamuro, T., Asano, K., Ita, Y., Kamizuka, T., Komugi, S., Koshida, S., Manabe, S., Matsunaga, N., Minezaki, T., Morokuma, T., Nakashima, A., Takagi, T., Tanabé, T., Uchiyama, M., Aoki, T., Doi, M., Handa, T., Kato, D., Kawara, K., Kohno, K., Miyata, T., Nakamura, T., Okada, K., Soyano, T., Tamura, Y.,

- Tanaka, M., Tarusawa, K., and Yoshii, Y. (2015). ANIR: Atacama near-infrared camera for the 1.0 m miniTAO telescope. *PASJ*, 67:4.
- Kroupa, P. (2001). On the variation of the initial mass function. *MNRAS*, 322:231–246.
- Kurosawa, K., Sasaki, W., Okuda, M., Takigawa, Y., and Yoshida, K. (1990). Super-polished silicon carbide mirror for high-power operation of excimer lasers in a vacuum ultraviolet spectral range. *Review of Scientific Instruments*, 61:728–731.
- Larkin, J. E., Quirrenbach, A., Krabbe, A., Aliado, T., Barczys, M., Brims, G., Canfield, J., Gasaway, T. M., LaFreniere, D., Magnone, N., Skulason, G., Spencer, M., Sprayberry, D., and Weiss, J. (2003). OSIRIS: infrared integral field spectrograph for the Keck adaptive optics system. In Iye, M. and Moorwood, A. F. M., editors, *Instrument Design and Performance for Optical/Infrared Ground-based Telescopes*, volume 4841 of Proc. SPIE, pages 1600–1610.
- Laurent, F., Renault, E., Kosmalski, J., Adjali, L., Boudon, D., Bacon, R., Caillier, P., Remillieux, A., Salaun, Y., and Delabre, B. (2008). MUSE image slicer: test results on largest slicer ever manufactured. In *Advanced Optical and Mechanical Technologies in Telescopes and Instrumentation*, volume 7018 of Proc. SPIE, page 70180J.
- Lee, D., Wells, M., Dickson, C. J., Shore, P., and Morantz, P. (2006). Development of diamond machined mirror arrays for integral field spectroscopy. In *Society of Photo-Optical Instrumentation Engineers (SPIE) Conference Series*, volume 6273 of Proc. SPIE, page 62731Y.
- Li, X., Jiang, Z., Gong, X., Zhang, H., Chen, K., Zheng, Y., Li, B., Yu, B., Xu, C., Ji, B., and Xu, Q. (2016). Stressed mirror annular polishing for scale-down TMT primary segments. In *Society of Photo-Optical Instrumentation Engineers (SPIE) Conference Series*, volume 9912 of Proc. SPIE, page 99120A.
- Lonsdale, C. J., Smith, H. E., Rowan-Robinson, M., Surace, J., Shupe, D., Xu, C., Oliver, S., Padgett, D., Fang, F., Conrow, T., Franceschini, A., Gautier, N., Griffin, M., Hacking, P., Masci, F., Morrison, G., O’Linger, J., Owen, F., Pérez-Fournon, I., Pierre, M., Puetter, R., Stacey, G., Castro, S., Polletta, M. d. C., Farrah, D., Jarrett, T., Frayer, D., Siana, B., Babbedge, T., Dye, S., Fox, M., Gonzalez-Solares, E., Salaman, M., Berta, S., Condon, J. J., Dole, H., and Serjeant, S. (2003). SWIRE: The SIRTf Wide-Area Infrared Extragalactic Survey. *PASP*, 115:897–927.
- Lubliner, J. and Nelson, J. E. (1980). Stressed mirror polishing. 1: A technique for producing nonaxisymmetric mirrors. *Appl. Opt.*, 19.
- Madau, P. and Dickinson, M. (2014). Cosmic Star-Formation History. *ARA&A*, 52:415–486.
- Magrini, L., Coccato, L., Stanghellini, L., Casasola, V., and Galli, D. (2016). Metallicity gradients in local Universe galaxies: Time evolution and effects of radial migration. *A&A*, 588:A91.
- Martin, H. M., Anderson, D. S., Angel, J. R. P., Nagel, R. H., West, S. C., and Young, R. S. (1990). Progress in the stressed-lap polishing of a 1.8-m f/1 mirror. In Barr, L. D., editor, *Advanced Technology Optical Telescopes IV*, volume 1236 of Proc. SPIE, pages 682–690.

- Matuszewski, M., Chang, D., Crabill, R. M., Martin, D. C., Moore, A. M., Morrissey, P., and Rahman, S. (2010). The Cosmic Web Imager: an integral field spectrograph for the Hale Telescope at Palomar Observatory: instrument design and first results. In *Ground-based and Airborne Instrumentation for Astronomy III*, volume 7735 of Proc. SPIE, page 77350P.
- Mazin, B. A., Meeker, S. R., Strader, M. J., Szypryt, P., Marsden, D., van Eyken, J. C., Duggan, G. E., Walter, A. B., Ulbricht, G., Johnson, M., Bumble, B., O'Brien, K., and Stoughton, C. (2013). ARCONS: A 2024 Pixel Optical through Near-IR Cryogenic Imaging Spectrophotometer. *PASP*, 125:1348–1361.
- McGregor, P. J., Hart, J., Conroy, P. G., Pfitzner, M. L., Bloxham, G. J., Jones, D. J., Downing, M. D., Dawson, M., Young, P., Jarnyk, M., and Van Harmelen, J. (2003). Gemini near-infrared integral field spectrograph (NIFS). In Iye, M. and Moorwood, A. F. M., editors, *Instrument Design and Performance for Optical/Infrared Ground-based Telescopes*, volume 4841 of Proc. SPIE, pages 1581–1591.
- Minowa, Y., Hayano, Y., Oya, S., Watanabe, M., Hattori, M., Guyon, O., Egner, S., Saito, Y., Ito, M., Takami, H., Garrel, V., Colley, S., Golota, T., and Iye, M. (2010). Performance of Subaru adaptive optics system AO188. In *Adaptive Optics Systems II*, volume 7736 of Proc. SPIE, page 77363N.
- Motohara, K., Konishi, M., Takahashi, H., Kato, N. M., Kitagawa, Y., Kobayakawa, Y., Terao, Y., Ohashi, H., Aoki, T., Doi, M., Kamizuka, T., Kohno, K., Minezaki, T., Miyata, T., Morokuma, T., Mori, K., Ohsawa, R., Okada, K., Sako, S., Soyano, T., Tamura, Y., Tanabe, T., Tanaka, M., Tarusawa, K., Uchiyama, M. S., Koshida, S., Asano, K., Tateuchi, K., Uchiyama, M., Todo, S., and Yoshii, Y. (2016). NIR camera and spectrograph SWIMS for TAO 6.5m telescope: overview and development status. In *Society of Photo-Optical Instrumentation Engineers (SPIE) Conference Series*, volume 9908 of Proc. SPIE, page 99083U.
- Motohara, K., Konishi, M., Takahashi, H., Tateuchi, K., Kitagawa, Y., Todo, S., Kato, N. M., Ohsawa, R., Aoki, T., Asano, K., Doi, M., Kamizuka, T., Kawara, K., Kohno, K., Koshida, S., Minezaki, T., Miyata, T., Morokuma, T., Okada, K., Sako, S., Soyano, T., Tamura, Y., Tanabe, T., Tanaka, M., Tarusawa, K., Uchiyama, M., and Yoshii, Y. (2014). Development of a simultaneous two-color near-infrared multi-object spectrograph SWIMS for the TAO 6.5-m telescope. In *Ground-based and Airborne Instrumentation for Astronomy V*, volume 9147 of Proc. SPIE, page 91476K.
- Müller-Sánchez, F., Prieto, M. A., Mezcuca, M., Davies, R. I., Malkan, M. A., and Elitzur, M. (2013). The Central Molecular Gas Structure in LINERs with Low-luminosity Active Galactic Nuclei: Evidence for Gradual Disappearance of the Torus. *ApJ*, 763:L1.
- Nierenberg, A. M., Treu, T., Wright, S. A., Fassnacht, C. D., and Auger, M. W. (2014). Detection of substructure with adaptive optics integral field spectroscopy of the gravitational lens B1422+231. *MNRAS*, 442:2434–2445.
- Noguchi, M. (1999). Early Evolution of Disk Galaxies: Formation of Bulges in Clumpy Young Galactic Disks. *ApJ*, 514:77–95.
- Ogilvy, J. A. (1987). Wave scattering from rough surfaces. *Reports on Progress in Physics*, 50(12):1553.

- Ozaki, S., Kitagawa, Y., Motohara, K., Konishi, M., Takahashi, H., Yoshikawa, T., Tateuchi, K., and Kato, N. (2012). Development of an integral field unit for a near-infrared multi-object imaging spectrograph SWIMS. In *Modern Technologies in Space- and Ground-based Telescopes and Instrumentation II*, volume 8450 of Proc. SPIE, page 84503Y.
- Ozaki, S., Tanaka, Y., Hattori, T., Mitsui, K., Fukushima, M., Okada, N., Obuchi, Y., Tsuzuki, T., Miyazaki, S., and Yamashita, T. (2014). Development of a slicer integral field unit for the existing optical spectrograph FOCAS: progress. In *Advances in Optical and Mechanical Technologies for Telescopes and Instrumentation*, volume 9151 of Proc. SPIE, page 915149.
- Pannella, M., Elbaz, D., Daddi, E., Dickinson, M., Hwang, H. S., Schreiber, C., Strazzullo, V., Aussel, H., Bethermin, M., Buat, V., Charmandaris, V., Cibinel, A., Juneau, S., Ivison, R. J., Le Borgne, D., Le Floch, E., Leiton, R., Lin, L., Magdis, G., Morrison, G. E., Mullaney, J., Onodera, M., Renzini, A., Salim, S., Sargent, M. T., Scott, D., Shu, X., and Wang, T. (2015). GOODS-Herschel: Star Formation, Dust Attenuation, and the FIR-radio Correlation on the Main Sequence of Star-forming Galaxies up to $z \sim 4$. *ApJ*, 807:141.
- Pecontal, E., Adam, G., Bacon, R., Courtes, G., Georgelin, Y., and Monnet, G. (1990). Observation of the central region of NGC 5728 with the integral field spectrograph TIGER. *A&A*, 232:331–336.
- Pereira-Santaella, M., Colina, L., García-Burillo, S., Planesas, P., Usero, A., Alonso-Herrero, A., Arribas, S., Cazzoli, S., Emonts, B., Piqueras López, J., and Villar-Martín, M. (2016). Sub-kpc star formation law in the local luminous infrared galaxy IC 4687 as seen by ALMA. *A&A*, 587:A44.
- Petrovsky, G. T., Tolstoy, M. N., Lubarsky, S. V., Khimitch, Y. P., and Robb, P. N. (1994). 2.7-meter-diameter silicon carbide primary mirror for the SOFIA telescope. In Stepp, L. M., editor, *Advanced Technology Optical Telescopes V*, volume 2199 of Proc. SPIE, pages 263–270.
- Pilbratt, G. L., Riedinger, J. R., Passvogel, T., Crone, G., Doyle, D., Gageur, U., Heras, A. M., Jewell, C., Metcalfe, L., Ott, S., and Schmidt, M. (2010). Herschel Space Observatory. An ESA facility for far-infrared and submillimetre astronomy. *A&A*, 518:L1.
- Piqueras López, J., Colina, L., Arribas, S., and Alonso-Herrero, A. (2013). VLT-SINFONI integral field spectroscopy of low- z luminous and ultraluminous infrared galaxies. II. 2D extinction structure and distance effects. *A&A*, 553:A85.
- Piqueras López, J., Colina, L., Arribas, S., Alonso-Herrero, A., and Bedregal, A. G. (2012). VLT-SINFONI integral field spectroscopy of low- z luminous and ultraluminous infrared galaxies. I. Atlas of the 2D gas structure. *A&A*, 546:A64.
- Piqueras López, J., Colina, L., Arribas, S., Pereira-Santaella, M., and Alonso-Herrero, A. (2016). VLT-SINFONI sub-kpc study of the star formation in local LIRGs and ULIRGs. Analysis of the global Σ_{SFR} structure and characterisation of individual star-forming clumps. *A&A*, 590:A67.

- Posselt, W., Holota, W., Kulinyak, E., Kling, G., Kutscheid, T., Le Fevre, O., Prieto, E., and Ferruit, P. (2004). NIRSpec: near-infrared spectrograph for the JWST. In Mather, J. C., editor, *Optical, Infrared, and Millimeter Space Telescopes*, volume 5487 of Proc. SPIE, pages 688–697.
- Robichaud, J. L., Wang, D., and Mastandrea, A. A. (1998). Cryogenic performance and long-term stability of metal optics and optical systems. In Fowler, A. M., editor, *Infrared Astronomical Instrumentation*, volume 3354 of Proc. SPIE, pages 178–186.
- Rolt, S. and Robertson, D. R. (2008). Diamond machining of aspherical mirrors and mirror arrays for Integral Field Units: part II. Metrology. In *Advanced Optical and Mechanical Technologies in Telescopes and Instrumentation*, volume 7018 of Proc. SPIE, page 70183S.
- Roth, M. M., Bauer, S.-M., Dionies, F., Fechner, T., Hahn, T., Kelz, A., Paschke, J., Popow, E., Schmolz, J., Wolter, D., Laux, U., and Altmann, W. (2000). PMAS design and integration. In Iye, M. and Moorwood, A. F., editors, *Optical and IR Telescope Instrumentation and Detectors*, volume 4008 of Proc. SPIE, pages 277–288.
- Rozas, M., Richer, M. G., López, J. A., Relaño, M., and Beckman, J. E. (2006). H α line profiles for a sample of supergiant HII regions. I. The main spectral component. *A&A*, 455:539–547.
- Saito, T. T. (1978). Diamond turning of optics: the past, the present, and the exciting future. *Optical Engineering*, 17(6):176570–176570.
- Sakon, I., Ikeda, Y., Nakagawa, H., Tokoro, H., Honda, M., Okamoto, Y. K., Kataza, H., Onaka, T., Chun, M. R., Richter, M. J., and Packham, C. (2016). A trial production of a large format image slicer unit for a possible future mid-infrared instrument on the TMT. In *Society of Photo-Optical Instrumentation Engineers (SPIE) Conference Series*, volume 9912 of Proc. SPIE, page 99125T.
- Sakon, I., Kataza, H., Onaka, T., Fujishiro, N., Ikeda, Y., Tokoro, H., Nakagawa, H., Kirino, O., Mitsui, K., and Okada, N. (2013). A design and trial production of the image slicer unit for the mid-infrared spectrograph. In *UV/Optical/IR Space Telescopes and Instruments: Innovative Technologies and Concepts VI*, volume 8860 of Proc. SPIE, page 88600Z.
- Salmi, F., Daddi, E., Elbaz, D., Sargent, M. T., Dickinson, M., Renzini, A., Bethermin, M., and Le Borgne, D. (2012). Dissecting the Stellar-mass-SFR Correlation in $z = 1$ Star-forming Disk Galaxies. *ApJ*, 754:L14.
- Salpeter, E. E. (1955). The Luminosity Function and Stellar Evolution. *ApJ*, 121:161.
- Sánchez-Blázquez, P., Rosales-Ortega, F. F., Méndez-Abreu, J., Pérez, I., Sánchez, S. F., Zibetti, S., Aguerri, J. A. L., Bland-Hawthorn, J., Catalán-Torrecilla, C., Cid Fernandes, R., de Amorim, A., de Lorenzo-Caceres, A., Falcón-Barroso, J., Galazzi, A., García Benito, R., Gil de Paz, A., González Delgado, R., Husemann, B., Iglesias-Páramo, J., Jungwiert, B., Marino, R. A., Márquez, I., Mast, D., Mendoza, M. A., Mollá, M., Papaderos, P., Ruiz-Lara, T., van de Ven, G., Walcher, C. J., and Wisotzki, L. (2014). Stellar population gradients in galaxy discs from the CALIFA survey. The influence of bars. *A&A*, 570:A6.
- Sanders, D. B., Mazzarella, J. M., Kim, D.-C., Surace, J. A., and Soifer, B. T. (2003). The IRAS Revised Bright Galaxy Sample. *AJ*, 126:1607–1664.

- Sanders, D. B. and Mirabel, I. F. (1996). Luminous Infrared Galaxies. *ARA&A*, 34:749.
- Schade, D., Lilly, S. J., Le Fevre, O., Hammer, F., and Crampton, D. (1996). Canada-France Redshift Survey. XI. Morphology of High-Redshift Field Galaxies from High-Resolution Ground-based Imaging. *ApJ*, 464:79.
- Scoville, N., Sheth, K., Aussel, H., Vanden Bout, P., Capak, P., Bongiorno, A., Casey, C. M., Murchikova, L., Koda, J., Álvarez-Márquez, J., Lee, N., Laigle, C., McCracken, H. J., Ilbert, O., Pope, A., Sanders, D., Chu, J., Toft, S., Ivison, R. J., and Manohar, S. (2016). ISM Masses and the Star formation Law at $Z = 1$ to 6: ALMA Observations of Dust Continuum in 145 Galaxies in the COSMOS Survey Field. *ApJ*, 820:83.
- Shapiro, K. L., Genzel, R., Förster Schreiber, N. M., Tacconi, L. J., Bouché, N., Cresci, G., Davies, R., Eisenhauer, F., Johansson, P. H., Krajnović, D., Lutz, D., Naab, T., Arimoto, N., Arribas, S., Cimatti, A., Colina, L., Daddi, E., Daigle, O., Erb, D., Hernandez, O., Kong, X., Mignoli, M., Onodera, M., Renzini, A., Shapley, A., and Steidel, C. (2008). Kinemetry of SINS High-Redshift Star-Forming Galaxies: Distinguishing Rotating Disks from Major Mergers. *ApJ*, 682:231–251.
- Sharples, R. M., Bender, R., Lehnert, M. D., Ramsay Howat, S. K., Bremer, M. N., Davies, R. L., Genzel, R., Hofmann, R., Ivison, R. J., Saglia, R., and Thatte, N. A. (2004). KMOS: an infrared multiple-object integral field spectrograph for the ESO VLT. In Moorwood, A. F. M. and Iye, M., editors, *Ground-based Instrumentation for Astronomy*, volume 5492 of Proc. SPIE, pages 1179–1186.
- Shibuya, T., Ouchi, M., Kubo, M., and Harikane, Y. (2016). Morphologies of $\sim 190,000$ Galaxies at $z = 0-10$ Revealed with HST Legacy Data. II. Evolution of Clumpy Galaxies. *ApJ*, 821:72.
- Sparre, M., Hayward, C. C., Springel, V., Vogelsberger, M., Genel, S., Torrey, P., Nelson, D., Sijacki, D., and Hernquist, L. (2015). The star formation main sequence and stellar mass assembly of galaxies in the Illustris simulation. *MNRAS*, 447:3548–3563.
- Speagle, J. S., Steinhardt, C. L., Capak, P. L., and Silverman, J. D. (2014). A Highly Consistent Framework for the Evolution of the Star-Forming "Main Sequence" from $z \sim 0-6$. *ApJS*, 214:15.
- Steidel, C. C., Shapley, A. E., Pettini, M., Adelberger, K. L., Erb, D. K., Reddy, N. A., and Hunt, M. P. (2004). A Survey of Star-forming Galaxies in the $1.4 < z < 2.5$ Redshift Desert: Overview. *ApJ*, 604:534–550.
- Stierwalt, S., Armus, L., Surace, J. A., Inami, H., Petric, A. O., Diaz-Santos, T., Haan, S., Charmandaris, V., Howell, J., Kim, D. C., Marshall, J., Mazzarella, J. M., Spoon, H. W. W., Veilleux, S., Evans, A., Sanders, D. B., Appleton, P., Bothun, G., Bridge, C. R., Chan, B., Frayer, D., Iwasawa, K., Kewley, L. J., Lord, S., Madore, B. F., Melbourne, J. E., Murphy, E. J., Rich, J. A., Schulz, B., Sturm, E., Vavilkin, T., and Xu, K. (2013). Mid-infrared Properties of Nearby Luminous Infrared Galaxies. I. Spitzer Infrared Spectrograph Spectra for the GOALS Sample. *ApJS*, 206:1.
- Storey, J. W. V. (2000). Infrared astronomy: In the heat of the night. The 1999 Ellery Lecture. *PASA*, 17:270–274.

- Sugai, H., Hattori, T., Kawai, A., Ozaki, S., Hayashi, T., Ishigaki, T., Ishii, M., Ohtani, H., Shimono, A., Okita, Y., Matsubayashi, K., Kosugi, G., Sasaki, M., and Takeyama, N. (2010). The Kyoto Tridimensional Spectrograph II on Subaru and the University of Hawaii 88 in Telescopes. *PASP*, 122:103–118.
- Sugano, T., Takeuchi, K., Goto, T., Yoshida, Y., and Ikawa, N. (1987). Diamond turning of an aluminum alloy for mirror. *CIRP Annals-Manufacturing Technology*, 36(1):17–20.
- Swinbank, A. M., Smail, I., Sobral, D., Theuns, T., Best, P. N., and Geach, J. E. (2012). The Properties of the Star-forming Interstellar Medium at $z = 0.8-2.2$ from HiZELS: Star Formation and Clump Scaling Laws in Gas-rich, Turbulent Disks. *ApJ*, 760:130.
- Tacconi, L. J., Neri, R., Genzel, R., Combes, F., Bolatto, A., Cooper, M. C., Wuyts, S., Bournaud, F., Burkert, A., Comerford, J., Cox, P., Davis, M., Förster Schreiber, N. M., García-Burillo, S., Gracia-Carpio, J., Lutz, D., Naab, T., Newman, S., Omont, A., Saintonge, A., Shapiro Griffin, K., Shapley, A., Sternberg, A., and Weiner, B. (2013). Phibss: Molecular Gas Content and Scaling Relations in $z \sim 1-3$ Massive, Main-sequence Star-forming Galaxies. *ApJ*, 768:74.
- Takahashi, H., Konishi, M., Motohara, K., Kato, N. M., Tateuchi, K., Kitagawa, Y., and Todo, S. (2014). Development of multi-object spectroscopy unit for simultaneous-color wide-field infrared multi-object spectrograph. In *Ground-based and Airborne Instrumentation for Astronomy V*, volume 9147 of Proc. SPIE, page 91476N.
- Tasca, L. A. M., Le Fèvre, O., Hathi, N. P., Schaerer, D., Ilbert, O., Zamorani, G., Lemaux, B. C., Cassata, P., Garilli, B., Le Brun, V., Maccagni, D., Pentericci, L., Thomas, R., Vanzella, E., Zucca, E., Amorin, R., Bardelli, S., Cassarà, L. P., Castellano, M., Cimatti, A., Cucciati, O., Durkalec, A., Fontana, A., Giavalisco, M., Grazian, A., Paltani, S., Ribeiro, B., Scodreggio, M., Sommariva, V., Talia, M., Tresse, L., Vergani, D., Capak, P., Charlot, S., Contini, T., de la Torre, S., Dunlop, J., Fotopoulou, S., Koekemoer, A., López-Sanjuan, C., Mellier, Y., Pforr, J., Salvato, M., Scoville, N., Taniguchi, Y., and Wang, P. W. (2015). The evolving star formation rate: M_* relation and sSFR since $z = 5$ from the VUDS spectroscopic survey. *A&A*, 581:A54.
- Taylor, J. S., Syn, C. K., Saito, T. T., and Donaldson, R. R. (1986). Surface finish measurements of diamond-turned electroless-nickel-plated mirrors. In *Society of Photo-Optical Instrumentation Engineers (SPIE) Conference Series*, volume 571 of Proc. SPIE, pages 10–21.
- Tecza, M., Thatte, N. A., Eisenhauer, F., Mengel, S., Roehrle, C., and Bickert, K. (2000). SPIFFI image slicer: revival of image slicing with plane mirrors. In Iye, M. and Moorwood, A. F., editors, *Optical and IR Telescope Instrumentation and Detectors*, volume 4008 of Proc. SPIE, pages 1344–1350.
- ter Horst, R., de Haan, M., Gubbels, G., Senden, R., van Venrooy, B., and Hoogstrate, A. (2012). Diamond turning and polishing tests on new RSP aluminum alloys. In *Modern Technologies in Space- and Ground-based Telescopes and Instrumentation II*, volume 8450 of Proc. SPIE, page 84502M.
- Terada, H., Kobayashi, N., Tokunaga, A. T., Pyo, T.-S., Nedachi, K., Weber, M., Potter, R., and Onaka, P. M. (2004). Performance update of the infrared camera and spectrograph for

- the Subaru Telescope (IRCS). In Moorwood, A. F. M. and Iye, M., editors, *Ground-based Instrumentation for Astronomy*, volume 5492 of Proc. SPIE, pages 1542–1550.
- Terlevich, R. and Melnick, J. (1981). The dynamics and chemical composition of giant extragalactic H II regions. *MNRAS*, 195:839–851.
- Toomre, A. (1964). On the gravitational stability of a disk of stars. *ApJ*, 139:1217–1238.
- Tsuno, K., Irikado, H., Oono, K., Ishida, J., Suyama, S., Itoh, Y., Ebizuka, N., Eto, H., Dai, Y., Lin, W., et al. (2005). New-technology silicon carbide (nt-sic): demonstration of new material for large lightweight optical mirror. In *Fourth International Asia-Pacific Environmental Remote Sensing Symposium 2004: Remote Sensing of the Atmosphere, Ocean, Environment, and Space*, pages 138–145. International Society for Optics and Photonics.
- Walker, H. J. (2000). A brief history of infrared astronomy. *Astronomy and Geophysics*, 41(5):10.
- Whitaker, K. E., van Dokkum, P. G., Brammer, G., and Franx, M. (2012). The Star Formation Mass Sequence Out to $z = 2.5$. *ApJ*, 754:L29.
- Wisnioski, E., Glazebrook, K., Blake, C., Poole, G. B., Green, A. W., Wyder, T., and Martin, C. (2012). Scaling relations of star-forming regions: from kpc-sized clumps to H II regions. *MNRAS*, 422:3339–3355.
- Wright, E. L. (2006). A Cosmology Calculator for the World Wide Web. *PASP*, 118:1711–1715.
- Wuyts, E., Rigby, J. R., Gladders, M. D., and Sharon, K. (2014). A Magnified View of the Kinematics and Morphology of RCSGA 032727-132609: Zooming in on a Merger at $z = 1.7$. *ApJ*, 781:61.
- Wuyts, S., Förster Schreiber, N. M., van der Wel, A., Magnelli, B., Guo, Y., Genzel, R., Lutz, D., Aussel, H., Barro, G., Berta, S., Cava, A., Graciá-Carpio, J., Hathi, N. P., Huang, K.-H., Kocevski, D. D., Koekemoer, A. M., Lee, K.-S., Le Flocc’h, E., McGrath, E. J., Nordon, R., Popesso, P., Pozzi, F., Riguccini, L., Rodighiero, G., Saintonge, A., and Tacconi, L. (2011). Galaxy Structure and Mode of Star Formation in the SFR-Mass Plane from $z \sim 2.5$ to $z \sim 0.1$. *ApJ*, 742:96.
- Yamamuro, T., Sato, S., Zenno, T., Takeyama, N., Matsuhara, H., Maeda, I., and Matsueda, Y. (2006). Measurement of refractive indices of 20 optical materials at low temperatures. *Optical Engineering*, 45(8):083401–083401.
- Yan, R., Bundy, K., Law, D. R., Bershady, M. A., Andrews, B., Cherinka, B., Diamond-Stanic, A. M., Drory, N., MacDonald, N., Sánchez-Gallego, J. R., Thomas, D., Wake, D. A., Weijmans, A.-M., Westfall, K. B., Zhang, K., Aragón-Salamanca, A., Belfiore, F., Bizyaev, D., Blanc, G. A., Blanton, M. R., Brownstein, J., Cappellari, M., D’Souza, R., Emsellem, E., Fu, H., Gaulme, P., Graham, M. T., Goddard, D., Gunn, J. E., Harding, P., Jones, A., Kinemuchi, K., Li, C., Li, H., Maiolino, R., Mao, S., Maraston, C., Masters, K., Merrifield, M. R., Oravetz, D., Pan, K., Parejko, J. K., Sanchez, S. F., Schlegel, D., Simmons, A., Thanjavur, K., Tinker, J., Tremonti, C., van den Bosch, R., and Zheng, Z.

- (2016). SDSS-IV MaNGA IFS Galaxy Survey- Survey Design, Execution, and Initial Data Quality. *AJ*, 152:197.
- Yoshii, Y., Aoki, T., Doi, M., Handa, T., Kawara, K., Kato, D., Kohno, K., Konishi, M., Koshida, S., Minezaki, T., Mitani, N., Miyata, T., Motohara, K., Sako, S., Soyano, T., Tanabe, T., Tanaka, M., Tarusawa, K., Bronfman, L., Ruiz, M. T., and Hamuy, M. (2010). The University of Tokyo Atacama Observatory 6.5m telescope project. In *Ground-based and Airborne Telescopes III*, volume 7733 of Proc. SPIE, page 773308.
- Zibetti, S., Charlot, S., and Rix, H.-W. (2009). Resolved stellar mass maps of galaxies - I. Method and implications for global mass estimates. *MNRAS*, 400:1181–1198.

Appendix A

Measurement Instruments

In an ultra-precision processing, an accuracy of a measurement instruments is an important factor determining whether or not the target surface precision has been achieved. In other words, ultra-precision processing is a system including the measurement, which is realized by highly accurate measurement on the order of (sub) nanometers. In order to perform highly accurate measurements of a diamond finished surface, it is important to satisfy the following conditions. (1) Keep the temperature of a workpiece constant. It is important to control the temperature of the measuring instrument and the workpiece so that at least the temperature fluctuation during the measurements can be ignored. (2) No force is applied to the workpiece, in other words, a non-contact measurement is desirable. (3) Use a measurement instrument with sufficient accuracy to know intrinsic machining error. In order to suppress the measurement error to $\lesssim 1\%$, measurement accuracy of $\sim 7\text{--}10$ times the tolerance to be measured is required.

We use ZYGO NewView7200 and MITAKA KOHKI PFU-3 for surface roughness and shape measurement, respectively. The appearance and specifications of both instruments are shown in Fig. A.1 and Table A.1 These instruments are installed in a thermostatic room kept at 20°C , and a workpiece is measured after that its temperature is well fitted in the ambient temperature. Also, both instruments are non-contact type using optical probes, and their measurement accuracy is optimal for our specifications.

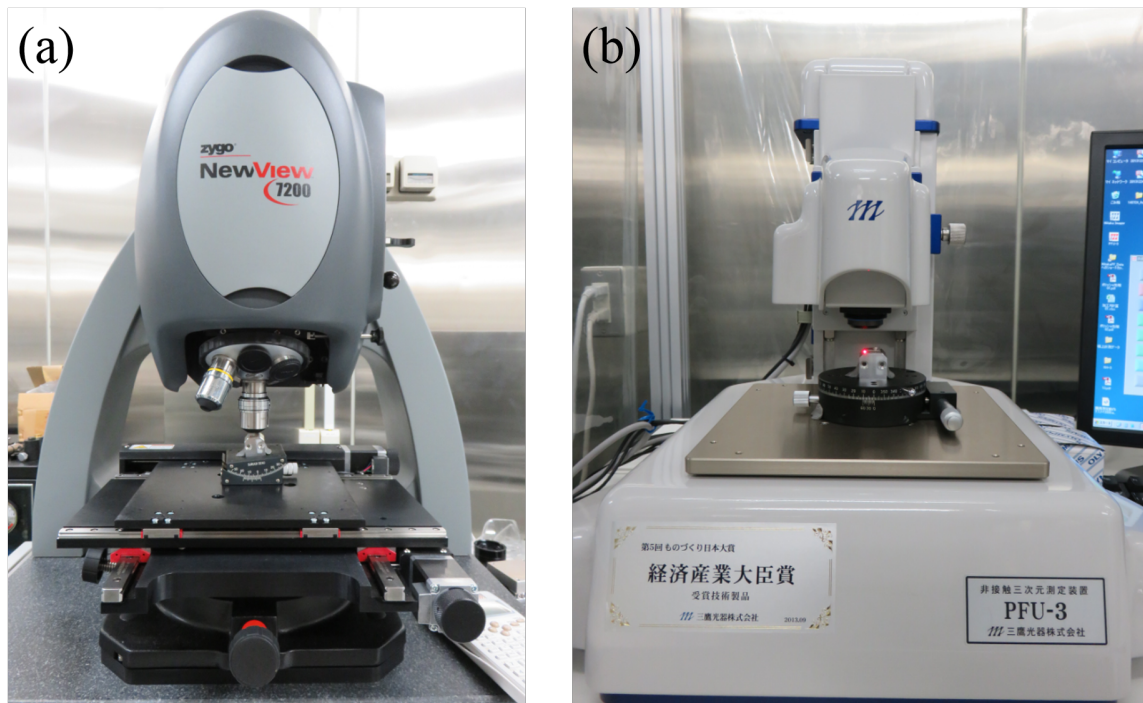


Fig. A.1 Photographs of measurement instruments. (a) ZYGO, NewView7200, which is a non-contact, scanning white light interferometry. (b) MITAKA KOHKI, PFU-3, which is a non-contact, surface texture measuring instrument with an automatic focus control system.

Table A.1 Specifications of measurement instruments

	NewView7200 (ZYGO)	PFU-3 (MITAKA KOHKI)
Method	non-contact, scanning white light interferometry	non-contact, scanning autofocus system
Resolution (X, Y)	$3.3 \mu\text{m}^{(a)}$	$0.1 \mu\text{m}$
Resolution (Z)	$< 0.1 \text{ nm}$	10 nm

^(a) Object lens magnification is 10x.

Appendix B

Elimination of cutting marks by post-process polishing

Cutting marks remaining after the cutting process will cause diffuse scatter or diffraction, which may reduce optical performance (Beaucamp et al., 2008). Therefore, we try to polish the NiP workpiece after the surface finishing and verify whether the cutting marks can be removed. Note that we are interested only in whether cutting marks can be eliminated by polishing, the workpiece used in this experiment is different from that shown in Section 5.2. The modified polishing work is done by hand with the polishing pad and the polishing liquid.

Fig. B.1 shows the change of surface profile with polishing time. The measurement is performed in the same manner as in described in Section 5.2. 5 minutes after the start of polishing, cutting marks still remain, and noticeable change can not be seen. Improvement in surface roughness is observed after 10 minutes, and the appearance of the cutting marks becomes also gentle. The cutting marks almost disappear after 40 minutes from the start of polishing. The surface roughness is improved at this point, reaching 3 nm or less.

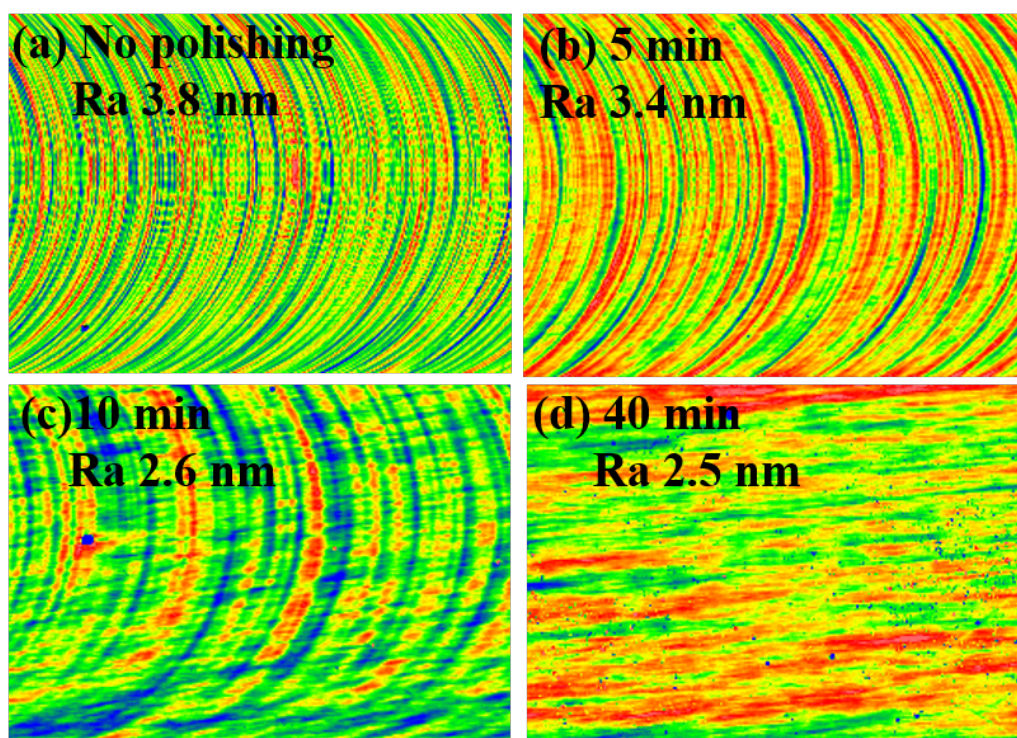


Fig. B.1 Results of post-process polishing by hand. The size of the measurement region is $702 \mu\text{m} \times 526 \mu\text{m}$. The time of the polishing changes with (a)–(d).